NUCLEAR MAGNETIC RESONANCE STUDIES TO CHARACTERIZE PHASE TRANSITIONS IN POROUS SYSTEMS

by

Linn Winsnes Thrane

A dissertation submitted in partial fulfillment
of the requirements for the degree

of

Doctor of Philosophy

in

Engineering

MONTANA STATE UNIVERSITY
Bozeman, Montana

November 2018

DEDICATION

To Mom, Dad, Martin, and bestefar

I would not be where I am today without you

ACKNOWLEDGMENTS

The work presented in this dissertation was funded in part by the National Science Foundation (NSF) under CBET grant 1335534, and the Department of Energy (DOE) under Grants No. DE-FE0024296 and DE-FE0026513. Any opinions, findings, conclusions or recommendations expressed herein are those of the authors and do not necessarily reflect the views of the DOE. The author also acknowledges Murdock Charitable Trust for equipment funding.

I would like to thank Dr. Sarah Codd and Dr. Joseph Seymour for the opportunity to work with and learn from them, and for all their guidance, advice, and support.

I would like to thank the MR lab students for great discussions and for creating such a welcoming work environment. I thank the MR Lab facility director Scott Busse for all his practical help with the MR equipment.

I would like to thank my wonderful friends Mike and Jordan for their unfaltering support and encouragement, and Madison for great scientific discussions and countless laughs.

I am grateful to my family for their patience, understanding, and all their love and support in the past 7 years. I know it has not always been easy to be so far apart, and I cannot wait to be closer to home again.

TABLE OF CONTENTS

TABLE OF CONTENTS – CONTINUED

TABLE OF CONTENTS – CONTINUED

LIST OF TABLES

LIST OF FIGURES

LIST OF FIGURES – CONTINUED

LIST OF FIGURES – CONTINUED

Figure Page

ABSTRACT

Nuclear magnetic resonance (NMR) allows for *in-situ* non-invasive studies of a wide range of systems at microscopic time and length scales. NMR relaxometry and diffusometry techniques along with magnetic resonance imaging (MRI) are applied to explore and characterize various phase transitions in complex systems. NMR techniques are highly sensitive to the thermodynamic phase of the system as well as restrictions on molecular motion, and the ability to detect and monitor phase transitions non-invasively is of great interest for various industrial applications

NMR frequency spectra and 1D T_2 relaxation measurements are used to characterize the presence of an amorphous drug and its liquid-solid phase transition. T_1-T_2 magnetic relaxation correlation experiments monitor the impact of long-time storage at high relative humidity on the drug in a porous silica tablet. The results indicate the ability of non-solid-state NMR to characterize crystalline and amorphous solid structural phases, and the potential for drug quality control by NMR methods.

High resolution MRI along with T_1-T_2 magnetic relaxation correlation experiments and pulsed gradient stimulated echo (PGStE) NMR methods are demonstrated to characterize hydrate formation. MRI monitors the spatial heterogeneity of the system as well as local hydrate growth rates. Using T_1-T_2 correlation NMR and spectrally resolved diffusometry, the transition from mobile to restricted dynamics is observed simultaneously for both water and cyclopentane throughout the hydrate formation process. The combination of these MR techniques allows for exploration of the complex molecular dynamics involved in hydrate formation processes.

Using a low-field NMR system, microbially induced calcite precipitation (MICP) processes in granular media are explored by means of 1D T_2 relaxation measurements. The 1D T_2 distributions allowed for in-situ monitoring of the mineral precipitation progress and indicates decrease in total pore volume and a significant change in the surface mineralogy of the granular media. The results confirm the potential for detailed characterization of MICP progression in engineering applications.

Ultimately, NMR is demonstrated as an effective method for detecting, characterizing, and monitoring several distinct phase transitions at various time- and length-scales.

INTRODUCTION

The research presented in this dissertation employed nuclear magnetic resonance (NMR) and magnetic resonance imaging (MRI) to explore and characterize liquid-solid phase transitions in several complex systems. NMR techniques are sensitive to the thermodynamic phase of the system (solid-liquid-gas) as well as restrictions on molecular motion, thus NMR relaxometry and diffusometry was used to explore the complex molecular dynamics taking place during phase transitions at microscopic time and length scales. MRI measurements were used to characterize the spatial heterogeneity of the phase transitions occurring within the system. NMR is a non-invasive, non-destructive measuring technique well-suited for heterogeneous and opaque systems and is therefore a particularly useful method for monitoring phase transitions as they occur in real time over an extensive range of length scales.

The work described here focuses on phase transitions in three distinct systems: 1) drug crystallization in bulk and in a porous construct, 2) cyclopentane-water hydrate formation, and 3) biomineralization in granular media. In all the above systems, only the liquid phase can be detected with NMR with the exception of a highly amorphous crystalline structure of the drug solidifying within the porous construct. The hydrate crystals, the mineral precipitate, and the highly ordered bulk crystalline drug all exhibit NMR signals too short to detect with the NMR systems used for this research due to hardware limitations.

High-field NMR was used to characterize drug crystallization and hydrate formation due to the high signal-to-noise ratio (SNR) attainable at high fields, which is

essential in studies of systems with limited signal, and its ability to explore the fundamental process of phase transitions and mass transport at the micro-scale.

Natural sediments, like the quartz sand used in the biomineralization study, is not well suited for characterization by high-field NMR due to the abundance of minerals with a wide range of magnetic susceptibility present in these samples. In the presence of an applied magnetic field, the magnetic susceptibilities interact with the applied field, generating internal field gradients, which will result in a broadening of the spectral peaks and more rapid signal decay. The effect of magnetic susceptibilities can be reduced by decreasing the applied magnetic field strength, thus a low-field NMR system was used to characterize bio mineralization processes in granular media.

Outline

An introduction to the basics of NMR is given in chapter 2 where topics such as spin angular momentum, the evolution of the magnetization, signal inversion by Fourier transform, spin relaxation mechanisms, magnetic field gradients, and imaging are described in detail. Additionally, an introduction to various basic pulse sequences can be found in chapter 2. Chapter 3 covers more advanced NMR topics with considerable focus on the theory behind diffusion measurements, but also topics such as spin relaxation in heterogeneous porous media, signal inversion by Laplace transformations, and relaxation correlation measurements.

The characterization of the crystallization of the drug fenofibrate in bulk and in a porous construct is presented in chapter 4. In addition, the impact of long-term storage on

the drug at high relative humidity is described. The results indicate that the drug takes on an amorphous structure when solidifying in the confined environment of the porous construct, and a highly ordered crystalline structure when solidifying in bulk. Water was observed occupying progressively more of the pore space of the porous construct at high relative humidity, decreasing the detected drug signal with time. The manuscript presenting this work was published in *Molecular Pharmaceutics* [1].

Chapter 5 discusses the results of monitoring hydrate formation by means of NMR. The onset, growth, and completion of hydrate growth was successfully detected using NMR frequency spectra. Spectrally resolved diffusion measurements demonstrated two distinct diffusion coefficients for water, of which the slower is representative of water trapped in the porous hydrate shell. The slow diffusion coefficient decreased in correlation with the progression of hydrate growth indicating a reduction in pore space of the hydrate shell as it fills in and increases in thickness. MRI measurements revealed heterogeneous hydrate growth and spatially dependent hydrate formation rates, while relaxation correlation measurements indicated complex diffusion dynamics during hydrate growth. This work has been submitted to *Journal of Magnetic Resonance* for publication.

The results of the low-field NMR measurements used to explore bio mineralization processes in granular media is presented in chapter 6. 1D MRI measurements revealed highly homogeneous calcite precipitation throughout the system. Relaxation measurements were used to investigate changes in pore size and surface mineralogy due to mineral precipitation on the surface of the granular media. The results

indicate that changes observed in the NMR relaxation data are predominantly a consequence of the formation of a gas interface between the bulk liquid and pore walls, reducing the impact of surface relaxation mechanisms. Scanning electron microscope (SEM) images collected during the experiment demonstrate a strong correlation also between changes in the relaxation data and mineral precipitate surface coverage. This work has been submitted to *Environmental Science and Technology* for publication.

References

1. Thrane, L.W., et al., *NMR Relaxometry to Characterize the Drug Structural Phase in a Porous Construct.* Molecular Pharmaceutics, 2018. **15**(7): p. 2614-2620. DOI: 10.1021/acs.molpharmaceut.8b00144

INTRODUCTION TO NUCLEAR MAGNETIC RESONANCE

Spin Angular Momentum

Nuclear magnetic resonance (NMR) utilizes the intrinsic quantum mechanical property possessed by all nuclei called spin angular momentum. The spin state of nuclei is described by the angular momentum quantum number *I*, which is a fixed integer or half-integer, and characterizes nuclei in their stable ground state. The spin state *I* is the product of a basis set of discrete values of angular momentum, *m*, which is measured along the z-axis and may take on integer or half-integer values in the range *–I*, *-I+1*, …, *I-1*, *I*. For example, a proton with $I=½$ can have two discrete energy projections labeled $m=½$ and $m=-½$, also referred to as "spin up" and "spin down," respectively. The component of *I* along the z-axis for a single nucleus in a basis state can be described by the eigenvalue equation [1],

$$I_z|m\rangle = m|m\rangle \qquad (2.1)$$

where the angular momentum I_z is the observable of interest, the eigenvector $|m\rangle$ is the basis state of I_z, and *m* is the eigenvalue, the observed value of I_z.

In the case of the quantum system existing in a definite state of I_z, a measurement of I_z would yield a definite result of either a "spin up" or a "spin down" state. However, if the quantum system is in some general superposition state $|\Psi\rangle$, the results of the measurement is given by the expectation value, $\langle\Psi|I_z|\Psi\rangle$ of I_z, defined as

$$\langle\Psi|I_z|\Psi\rangle = \sum_m |a_m|^2\, m \qquad (2.2)$$

A measurement will force the superposition state into a single eigenstate $|m\rangle$ defined by the normalized probability $|a_m|^2$. Until the measurement is performed, the quantum system will exist in a superposition state of multiple eigenstates.

The time evolution of a quantum system is described by the Schrödinger equation

$$i\hbar\frac{\partial}{\partial t}|\Psi(t)\rangle = H|\Psi(t)\rangle \qquad (2.3)$$

where *H* is the Hamiltonian operator and corresponds to the total energy of the quantum system. In the case of a time independent *H*, the Schrödinger equation reduces to

$$|\Psi(t)\rangle = \exp(-iHt)|\Psi(0)\rangle \qquad (2.4)$$

here the exponential is known as the evolution operator *U(t)*. In the presence of a static magnetic field $\boldsymbol{B_0}$, the Hamiltonian is written as $-\boldsymbol{\mu}\cdot\boldsymbol{B_0}$ and describes the interaction between spin nuclei and said magnetic field, known as the Zeeman interaction. Nuclei have a magnetic dipole moment, $\boldsymbol{\mu}$, which will align either parallel or anti-parallel with the $\boldsymbol{B_0}$ field with a slight preference for parallel alignment. The summation of magnetic moments results in a net bulk magnetization, $\boldsymbol{M}$, in the direction of the $\boldsymbol{B_0}$ field due to the preference for parallel alignment. Parallel alignment is the lower energy "spin up" state, while anti-parallel alignment is the higher energy "spin down" state. The energy difference between the two spin states is equal to $\Delta E = \gamma\hbar B_0$, as indicated in Figure 2.1.

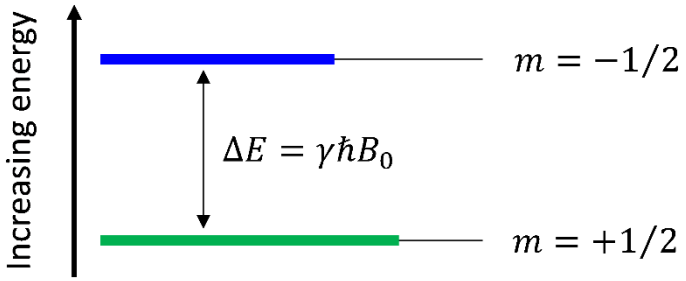

Figure 2.1. The energy difference between the higher and lower energy spin states is equal to $\gamma\hbar B_0$. There is a slight preference for the lower energy state, thus the total sum of the magnetic moments in the system will result in a net magnetization, ***M***, in the direction of $\boldsymbol{B_0}$.

The Hamiltonian operator in the case of $\boldsymbol{B_0}$ oriented along the z-axis, is referred to as the Zeeman Hamiltonian

$$H = -\gamma B_0 I_z \qquad (2.5)$$

where γ is known as the gyromagnetic ratio with a value specific to a particular nucleus. Hydrogen, ^{1}H, has one of the largest gyromagnetic ratios of all nuclei with $\gamma = 2.675 \times 10^8\ rad/(T \cdot s)$ and is also naturally abundant, making it the most common nuclei used in NMR experimental work.

In the presence of a magnetic field the angular momentum of a nucleus causes it to precess around the z-axis at a precession frequency called the Larmor frequency which is proportional to the strength of the magnetic field and the gyromagnetic ratio.

$$\omega_0 = \gamma B_0 \qquad (2.6)$$

The Larmor frequency is also the frequency at which spins transition between the two spin states. It is this transitioning that creates the signal detected in NMR as the signal results from the energy difference between the energy absorbed or emitted during the

transition from the lower to higher or higher to lower energy state respectively. Thus, the signal is proportional to the ratio of the populations in the two energy levels as described by the Boltzmann distribution

$$\frac{N^+}{N^-} = \exp\left(\frac{\gamma B_0 \hbar}{kT}\right) \qquad (2.7)$$

where *T* is the absolute temperature of the system, *k* is the Boltzmann constant, and $\frac{N^+}{N^-}$ is the ratio of the two energy states as well as the observed net magnetization in NMR.

Excitation and Signal Detection

The microscopic quantum description of a single nucleus is not advantageous in NMR where the signal is generated from an abundance of nuclei. Instead, a semi-classical macroscopic description of the system can be used to describe the average and detectable behavior of the spins. In this macroscopic description the angular momentum vector simplifies to $\boldsymbol{M}/\gamma$ where γ is the gyromagnetic ratio and $\boldsymbol{M}$ is the net magnetization vector which will precess around the z-axis at the Larmor frequency, $\omega_0 = \gamma B_0$, for a single nucleus. The magnitude of $\boldsymbol{M}$ is inherently much smaller than $\boldsymbol{B_0}$, so in order to detect the signal generated by $\boldsymbol{M}$ it has to be moved away from thermal equilibrium in the z-direction of the $\boldsymbol{B_0}$-field and into the transverse x-y plane. By applying a radiofrequency (rf) pulse at the Larmor frequency, ω_0, a secondary oscillating magnetic field $\boldsymbol{B_1}$ forms in the transverse plane. $\boldsymbol{B_1}$ exerts a torque on $\boldsymbol{M}$, tipping it into the transverse plane. The time evolution of $\boldsymbol{M}$ in the presence of a magnetic field is given by

$$\frac{d\boldsymbol{M}}{dt} = \gamma \boldsymbol{M} \times \boldsymbol{B} \qquad (2.8)$$

The oscillation of the $\boldsymbol{B_1}$-field will also occur at the Larmor frequency, given the system is on resonance, and is defined as

$$\boldsymbol{B_1} = B_1 \cos \omega_0 t\, \mathbf{i} + B_1 \sin \omega_0 t\, \mathbf{j} \qquad (2.9)$$

If the cross product in Equation (2.8) is performed with $\boldsymbol{B_1}$ as the magnetic field, the result yields three equations describing the evolution of $\boldsymbol{M}$ in each coordinate direction

$$\frac{d\boldsymbol{M_x}}{dt} = \gamma\left[M_y B_0 + M_z B_1 \sin \omega_0 t\right]$$

$$\frac{d\boldsymbol{M_y}}{dt} = \gamma[M_z B_1 \cos \omega_0 t - M_x B_0] \qquad (2.10)$$

$$\frac{d\boldsymbol{M_z}}{dt} = \gamma\left[-M_x B_1 \sin \omega_0 t - M_y B_1 \cos \omega_0 t\right]$$

Under the initial condition $\boldsymbol{M}(t) = M_0\mathbf{k}$, the above equations simplify to

$$M_x = M_0 \sin \omega_1 t \sin \omega_0 t$$

$$M_y = M_0 \sin \omega_1 t \cos \omega_0 t \qquad (2.11)$$

$$M_z = M_0 \cos \omega_1 t$$

where $\omega_1 = \gamma B_1$. The above equations describe the behavior of the magnetization vector in the laboratory frame, where $\boldsymbol{M}$ precesses around the z-axis at ω_0 due to the angular momentum of nuclei in the presence of a magnetic field and around the $\boldsymbol{B_1}$-field at ω_1 during the duration of the rf pulse. The motion of $\boldsymbol{M}$ in the laboratory frame is shown in Figure 2.2.

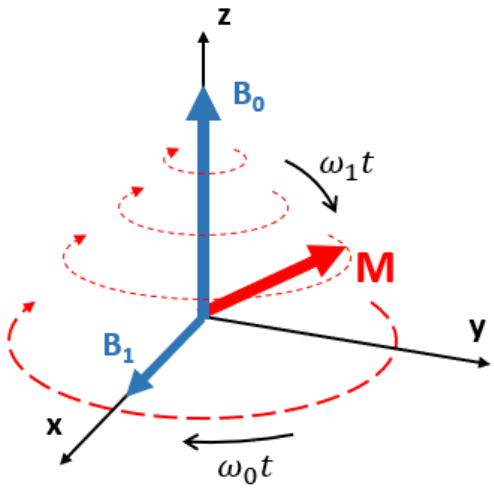

Figure 2.2. During a 90° rf pulse, the net magnetization vector, ***M***, as viewed from the laboratory frame of reference, will precess around the $\boldsymbol{B_0}$-field at the Larmor frequency, ω_0 and around the $\boldsymbol{B_1}$-field at ω_1.

To further simplify the description of ***M*** it is common to introduce a rotating frame of reference that rotates around the $\boldsymbol{B_0}$-field at a frequency ω. Recall that the Hamiltonian due to the static magnetic field in the z-direction, $\boldsymbol{B_0}$, is $H = -\gamma B_0 I_z$. In the rotating frame, an additional frequency term needs to be added to the Hamiltonian to account for the rotation of the reference frame itself.

$$H_{rot} = -\gamma \left(B_0 + \frac{\omega}{\gamma} \right) I_z \qquad (2.12)$$

When an oscillating $\boldsymbol{B_1}$ field is applied to tip the magnetization vector into the transverse plane, the Hamiltonian becomes

$$H_{rot} = -\gamma \left(B_0 + \frac{\omega}{\gamma} \right) I_z - \gamma B_1 I_x \qquad (2.13)$$

When the system is at resonance and the reference frame frequency $\omega = \omega_0$, H_{rot} reduces to $-\gamma B_1 I_x$, and the $\boldsymbol{B_1}$-field appears stationary in the transverse plane as shown in Figure 2.3. The equations describing the evolution of $\boldsymbol{M}$ in each coordinate direction then reduces to

$$M_x = 0$$

$$M_y = M_0 \sin \omega_1 t \quad (2.14)$$

$$M_z = M_0 \cos \omega_1 t$$

Assuming the $\boldsymbol{B_1}$-field is applied in the x-direction as in Figure 2.3.

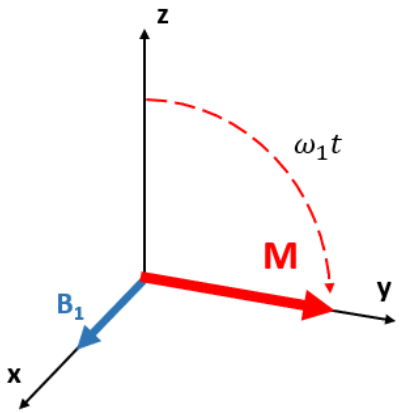

Figure 2.3. Because the rotating frame of reference rotates at the Larmor frequency, ω_0, $\boldsymbol{B_1}$ appears to be stationary in the transverse plane, and the only rotation that occurs is that of $\boldsymbol{M}$ around $\boldsymbol{B_1}$.

The magnetization vector's, $\boldsymbol{M}$, angle of rotation around $\boldsymbol{B_1}$ is equal to $\omega_1 t$. It is then easy to see that by controlling the duration of the rf pulse and the amplitude of $\boldsymbol{B_1}$, $\boldsymbol{M}$ can be reoriented to the transverse plane. A reorientation to the transverse plane is referred to as a 90° or $\frac{\pi}{2}$ pulse. By doubling the duration of the rf pulse or increasing the amplitude of $\boldsymbol{B_1}$, the magnetization vector will align with the negative z-direction,

referred to as a 180° or π pulse. This disturbance from equilibrium is referred to as the NMR phenomenon.

The precession of ***M*** in the transverse plane induces an oscillating current in a rf receiver coil at the Larmor frequency. The coil measures the magnitude and phase of the magnetization, resulting in a complex (real and imaginary) signal oscillating in quadrature. The most basic NMR measurement consists of a single 90° rf pulse immediately followed by signal acquisition shown in Figure 2.4. The NMR signal takes the form of a sinusoidal exponential decay that oscillates at an offset frequency, $\Delta\omega$, and is called a "Free Induction Decay (FID)." The FID signal decays at a rate of $1/T_2^*$ and is given by

$$S(t) = S_0 \exp(i\varphi) \exp(i\Delta\omega t) \exp\left(\frac{-t}{T_2^*}\right) \qquad (2.15)$$

where S_0 is the signal immediately following excitation and T_2^* is the spin-spin relaxation in presence of inhomogeneities in $\boldsymbol{B_0}$. The decay of the NMR signal is due to two relaxation mechanisms, spin-spin T_2 and spin-lattice T_1 relaxation, which will be discussed in a later section.

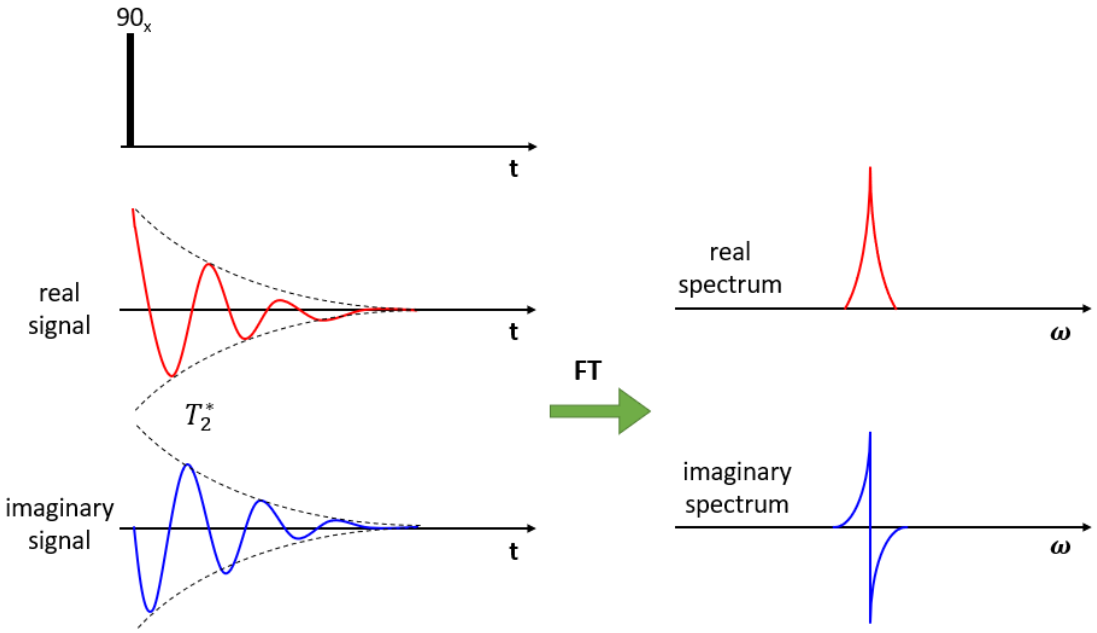

Figure 2.4. The real and imaginary oscillating decaying signal obtained through a Free Induction Decay (FID) measurement can be Fourier transformed from time domain to produce a real and imaginary spectrum in frequency domain.

The NMR signal is recorded as a decaying signal in time domain and may consist of multiple individual frequencies. t and ω are conjugate variables and the complex signal is therefore well-suited for analysis by Fourier transformation which converts the time domain signal to frequency domain and vice versa. The Fourier transform of the time domain data to the frequency domain produces a frequency spectrum and is expressed as

$$F\{S(t)\} = s(\omega) = \int_{-\infty}^{\infty} S(t) \exp(i\omega t) dt \qquad (2.16)$$

For a liquid, the Fourier transform of the real component of the FID results in a Lorentzian line shape in the frequency domain, known as the absorption spectrum, with a Full-Width-Half-Maximum of $1/\pi T_2^*$ (Figure 2.4, top). The line shape of the imaginary

component of the FID in the frequency domain has a slightly greater width and is known as the dispersion spectrum (Figure 2.4, bottom). In solids, the correlation time of the dipolar coupling is much longer resulting in a rapidly decaying (~1-100 μs) Gaussian FID, which generates a broad Gaussian line shape in the frequency domain.

Relaxation

Following an rf pulse, the spin system will gradually return to its thermal equilibrium state along the z-axis due to a process known as spin-lattice relaxation, or T_1 relaxation. The system is at thermal equilibrium when the net magnetization $\boldsymbol{M}$ is fully aligned with the $\boldsymbol{B_0}$ field. T_1 relaxation occurs due to an exchange of energy between the spins and their surrounding environment, or lattice, and is typically at the order of 0.1-10 seconds for liquids at room temperature. The mathematical description of the T_1 relaxation mechanism is

$$\frac{dM_z}{dt} = -\frac{M_z - M_0}{T_1} \qquad (2.17)$$

with solution

$$M_z(t) = M_z(0) + M_0\left(1 - exp\left(\frac{-t}{T_1}\right)\right) \qquad (2.18)$$

The lifetime of the transverse magnetization following an rf pulse is governed by spin-spin relaxation. Spin-spin relaxation, also termed T_2 relaxation, is the process in which the spins come to thermal equilibrium among themselves. In other words, the decay of the transverse magnetization, and therefore the induced signal is caused by a loss of spin coherence due to molecular interactions. The timescale for T_2 relaxation ranges from

microseconds in highly ordered crystalline structures to seconds for liquids at room temperature. The T_2 relaxation mechanism is described by

$$\frac{dM_{x,y}}{dt} = -\frac{M_{x,y}}{T_2} \qquad (2.19)$$

with solution

$$M_{x,y}(t) = M_{x,y}(0)exp\left(\frac{-t}{T_2}\right) \qquad (2.20)$$

By combining Equation (2.8), (2.18), and (2.20), a set of equations describing the time evolution of $\boldsymbol{M}$ in the rotating frame due to both excitation and relaxation is obtained.

$$\frac{dM_x}{dt} = \gamma M_y(B_0 - \omega/\gamma) - \frac{M_x}{T_2}$$

$$\frac{dM_y}{dt} = \gamma M_z B_1 - \gamma M_x(B_0 - \omega/\gamma) - \frac{M_y}{T_2} \qquad (2.21)$$

$$\frac{dM_z}{dt} = -\gamma M_y B_1 - \frac{(M_z - M_0)}{T_1}$$

These equations are known as the Bloch equations and were first formulated by Felix Bloch in 1946 [2].

T_1 and T_2 relaxation are caused by spin interactions that lead to stochastic fluctuations of the dipolar Hamiltonian, H_D. The rate of relaxation is sensitive to both the magnitude and the rate of these fluctuations which have the potential to induce transitions between spin states resulting in T_1 relaxation, and to generate a loss of phase coherence resulting in T_2 relaxation. T_1 relaxation is best described in the laboratory frame and lends itself well to the use of time-dependent perturbation theory when describing the transition rate between energy states mathematically. T_2 relaxation is most naturally described in the rotating frame where the transverse magnetization is stationary, and the approach of

time-dependent perturbation theory is therefore not appropriate. Instead, density operator formalism is used to describe the behavior of the magnetization due to spin-spin relaxation. Both methods result in an expression that includes the auto-correlation function, $G^q(\tau)$, where the Fourier transform produces the spectral density function, $J(\omega)$. In a static magnetic field, $\boldsymbol{B_0}$, there are three possible quantum transitions that may occur and cause relaxation through dipolar coupling for spin-½ nuclei; a zero-quantum transition, a single-quantum transition, and a double quantum transition. The probability of the coupled spins remaining in their original energy state is called the zero-quantum transition probability and is given by

$$W_0 = \frac{1}{10} b^2 J^0(\omega) \quad (2.22)$$

where $b = -\frac{\mu_0}{4\pi}\frac{\hbar\gamma^2}{r_{ij}^3}$, and r_{ij} is the radial distance between the spins. The probability of one of the two spins transitioning to a new energy state, the single-quantum transition probability, is given by

$$W_0 = \frac{3}{20} b^2 J^1(\omega) \quad (2.23)$$

and the probability of both spins transitioning to a new energy state, the double-quantum transition probability, is given by

$$W_0 = \frac{3}{5} b^2 J^2(\omega) \quad (2.24)$$

The spectral density functions for the zero, single, and double quantum transition are given by the following equations, respectively

$$J^{(0)}(\omega) = \frac{24}{15r_{ij}^6}\frac{\tau_c}{1+\omega^2\tau_c^2}$$

$$J^{(1)}(\omega) = \frac{4}{15r_{ij}^6}\frac{\tau_c}{1+\omega^2\tau_c^2} \quad (2.25)$$

$$J^{(2)}(\omega) = \frac{16}{15r_{ij}^6}\frac{\tau_c}{1+\omega^2\tau_c^2}$$

where τ_c is the rotational correlation time of the molecules, the time it takes the molecule to rotate by 1 rad. Typically, small molecules or non-viscous fluids have short correlation times and double-quantum transitions are the most probable transitions, while large molecules, or viscous fluid have long correlation times and zero-quantum transitions are most probable.

The spectral density functions can be used to generate equations that provide a solution for the relaxation rates. The T_1 relaxation rate in terms of the Larmor frequency, ω_0, is given by

$$\frac{1}{T_1} = (\frac{\mu_0}{4\pi})^2\,\gamma^4\hbar^2\frac{3}{2}I(I+1)\left[J^{(1)}(\omega_0) + J^{(2)}(2\omega_0)\right] \quad (2.26)$$

The T_1 relaxation rate is governed by single- and double-quantum transitions, with no contribution from spins that remain in their original energy state. It is therefore apparent that T_1 relaxation is caused by an energy exchange between the spins and the local environment.

The T_2 relaxation rate at the Larmor frequency is given by

$$\frac{1}{T_2} = (\frac{\mu_0}{4\pi})^2\,\gamma^4\hbar^2\frac{3}{2}I(I+1)\left[\frac{1}{4}J^{(0)}(0) + \frac{5}{2}J^{(1)}(\omega_0) + \frac{1}{4}J^{(2)}(2\omega_0)\right] \quad (2.27)$$

In addition to the single and double-quantum transitions, the T_2 relaxation rate also depends on the zero-quantum transition. The additional term infers that T_2 relaxation will always occur at a rate equal to or faster than T_1 relaxation. At short correlation times, the T_1 and T_2 relaxation rates are equal. As the correlation time increases so does the contribution of the zero-quantum transition term, causing the T_2 relaxation rate to increase further while the T_1 relaxation rate decreases as demonstrated in Figure 2.5.

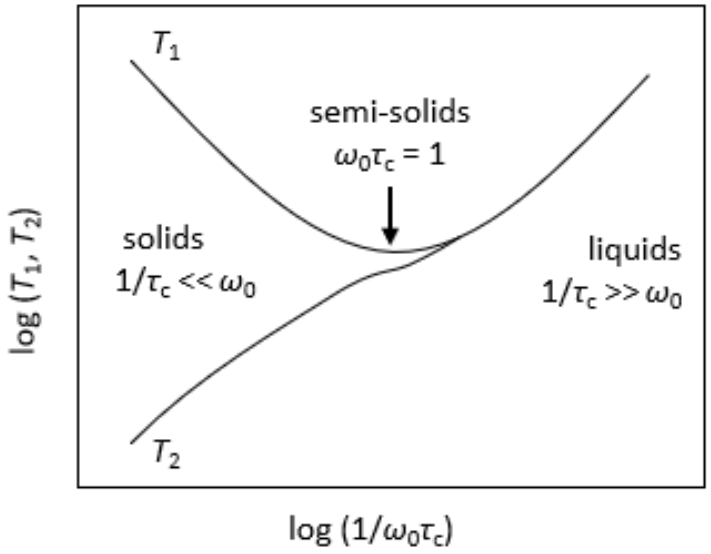

Figure 2.5. T_1 and T_2 relaxation times as a function of the correlation time, τ_c. For long τ_c in liquids, T_1 and T_2 are approximately equal, while for shorter τ_c in solids, T_2 is much shorter than T_1.

Basic Pulse Sequences

NMR measurements rely on manipulation of the spin system through a sequence of radio frequency pulses and magnetic field gradients under the influence of the Zeeman Hamiltonian and relaxation processes. The combination, as well as the timing of the rf pulses, gradients, and the signal detection determines the observable encoded for. In this

section, four basic NMR pulse sequences originating from the early beginnings of this field of research will be described. These pulse sequences are still frequently used today and include the inversion recovery sequence, the Hahn echo [3], the Carr-Purcell-Meiboom-Gill (CPMG) sequence [4, 5], and the stimulated spin-echo [6]. A pulse sequence diagram with increasing time from left to right is typically used to show the order and the timing of the rf pulses and the gradients in these NMR sequences.

Each sequence is typically repeated *N* number of times during an NMR measurement. Repeating the sequence several times averages out random noise resulting in increased signal-to-noise ratio (SNR) and is necessary for phase cycling. By varying the relative phases of the pulses for each repetition, phase cycling sequences enable cancellation of coherent noise, correction for phase and amplitude anomalies, transverse magnetization interference, and echo artifacts. Consequently, phase cycling is essential in most NMR measurements, and the most commonly incorporated phase cycling sequence is the 4-pulse CYCLOPS sequence of Hoult and Richards [7].

Inversion Recovery

The inversion recovery sequence, shown in Figure 2.6, is used to measure T_1 relaxation times. The first 180° rf pulse inverts $\boldsymbol{M}$ onto the -z-axis, the most severe disturbance of the spin system from thermal equilibrium. Due to spin-lattice relaxation, $\boldsymbol{M}$ decreases in magnitude in the -z-direction as the system begins to return to thermal equilibrium. After some time, τ, a 90° rf pulse brings the remaining $\boldsymbol{M}$ into the transverse plane where the induced signal is recorded. The evolution of the signal amplitude along the z-axis can be seen in Figure 2.7 and is described by the equation

$$M_z(t) = M_0\left(1 - 2exp\left(-\frac{t}{T_1}\right)\right) \qquad (2.28)$$

The crossover from **-*M*** to **+*M*** observed in Figure 2.7 occurs at $t = 0.6931T_1$ and can therefore be used to extract the T_1 time from the measurement.

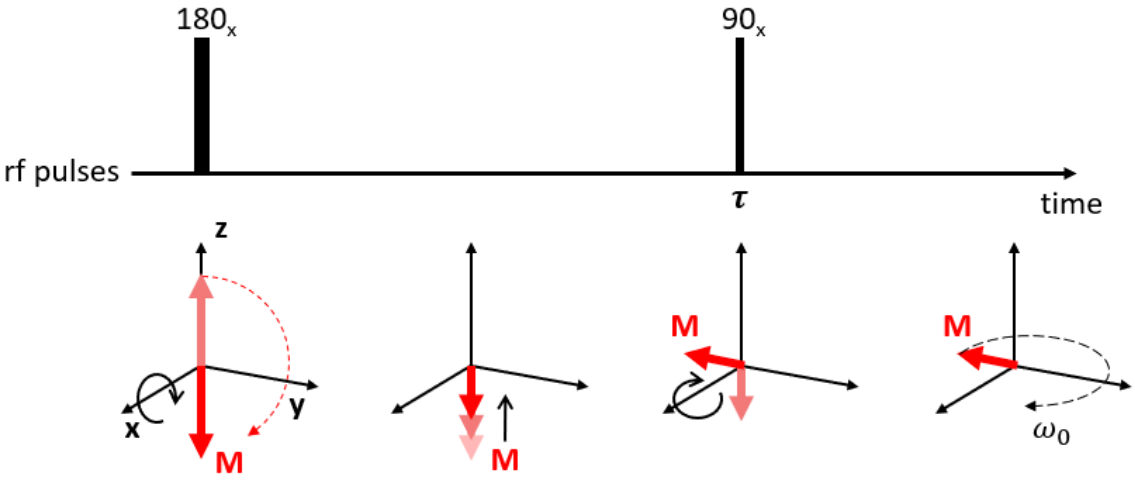

Figure 2.6. The inversion recovery (IR) pulse sequence the magnetization vector is first inverted by a 180° rf pulse. ***M*** will then gradually return to thermal equilibrium due T_1 relaxation effects. T_1 relaxation is measured by bringing ***M*** back to the transverse plane where the reduction of the magnitude of ***M*** is detected. The evolution of ***M*** is depicted bellow the IR sequence.

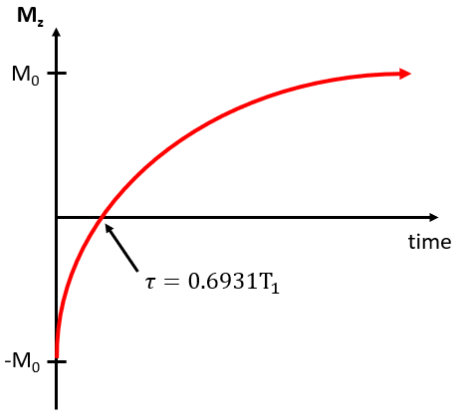

Figure 2.7. The amplitude of $\boldsymbol{M}$ as a function of time following the 180° rf pulse. The crossover from negative to positive amplitude occurs at $\tau = 0.6931T_1$.

Hahn Echo

Magnetic field inhomogeneities across a sample is inevitable in all NMR experiments and will cause spins to precess at different Larmor frequencies depending on their location. This effect results in a dephasing of the transverse magnetization vector following a 90° rf pulse as shown in Figure 2.8 as some spins will precess at a faster rate than others. Accordingly, phase coherence is time limited. In 1950, Erwin Hahn discovered that this loss of phase coherence is reversible, establishing the basis of today's T_2 measurements. By applying a 180° rf pulse at some time τ after the 90° rf pulse, the dephasing is reversed and causes refocusing of the transverse magnetization. Following the 180° pulse, the spins will re-phase at the same rate they were dephasing and arrive simultaneously in phase again to produce an echo signal at 2τ. The spins are subject to T_2

relaxation during the 2τ period, consequently the signal amplitude at the echo center will be less than the initial signal amplitude at $t = 0$.

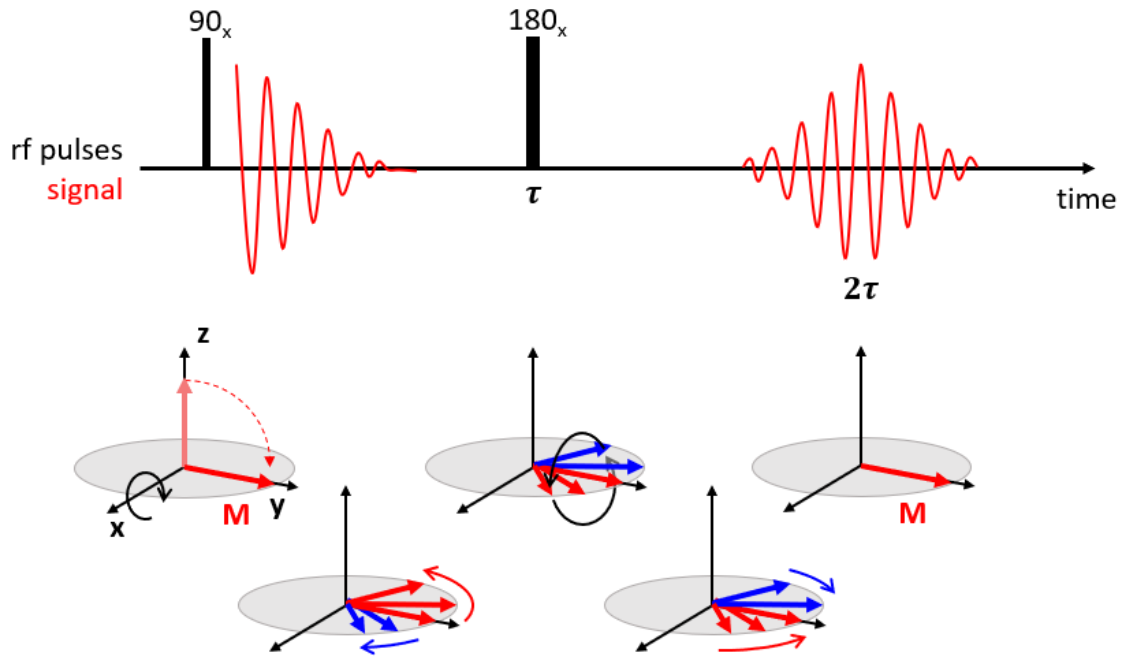

Figure 2.8. The Hahn echo, or spin-echo, pulse sequence allows for dephasing of the spins in the transverse plane for a period τ before a 180° rf pulse reverses the dephasing. An echo is produced at 2τ once the spins are perfectly in phase again. The dephasing and refocusing of the spins is demonstrated in terms of $\boldsymbol{M}$ below the pulse sequence.

CPMG Echo Train

In 1954, Carr and Purcell suggested that successive phase coherence recoveries are possible by performing consecutive 180° rf pulses at a rate of $1/2\tau$ as shown in Figure 2.9. This generates a train of echoes with a maximum echo amplitude that decays exponentially at a rate of $1/T_2$. The signal decay in the transverse plane is described by the equation

$$M_{x,y}(t) = M_0 \exp\left(-\frac{t}{T_2}\right) \quad (2.29)$$

In 1958, Meiboom and Gill modified the Carr-Purcell train with the use of quadrature 180_y rf pulses which compensates for the cumulative effect of small tip-angle errors. The CPMG sequence can then be used to determine the T_2 relaxation time in a single experiment.

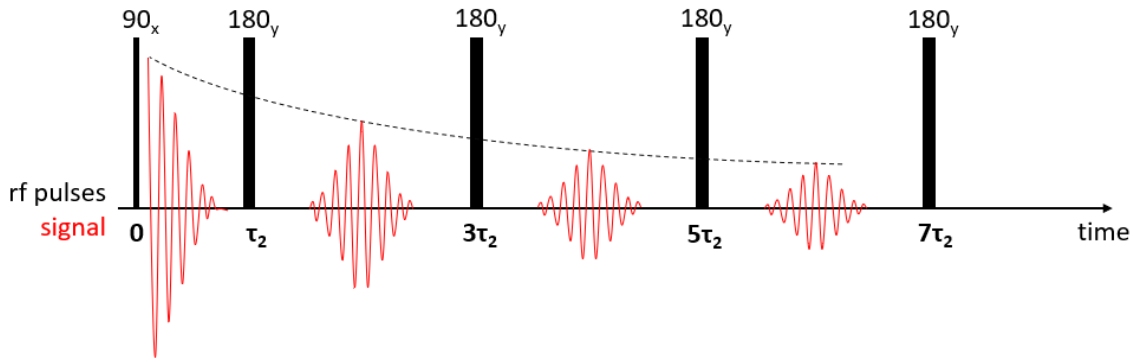

Figure 2.9. The Carr-Purcell-Meiboom-Gill sequence consist of a series of 180° rf pulses that refocuses the spins over and over producing a train of spin-echoes with decreasing maximum amplitude.

Stimulated Echo

The stimulated echo is particularly useful when measuring the translational motion of molecules in materials where the transverse relaxation time is considerably shorter than the longitudinal relaxation time. By applying a second 90_x rf pulse at some time τ after the first 90_x rf pulse (Figure 2.10), the phase coherence can be stored along the -z-axis for a longer period. While stored along the z-axis, only longitudinal relaxation will occur. The transverse magnetization can then be recalled at some later time with a third 90_x rf pulse to examine how the molecules have changed during storage. When the magnetization is recalled into the transverse plane, phase coherence is recovered, just like in the Hahn Echo sequence, producing the stimulated echo that can be recorded. The

stimulated echo is particularly important in the pulsed field gradient stimulated echo sequence (PGStE), which is used to measure the diffusion of molecules in materials with fast T_2 relaxation rate. The PGStE sequence will be discussed in more detail in a later section.

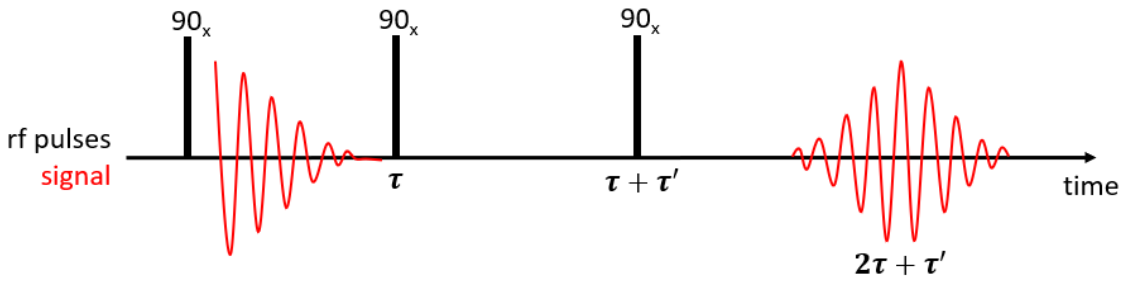

Figure 2.10. The stimulated echo sequence stores the phase coherence along the -z-axis for a period τ', allowing for longitudinal relaxation only while translational motion occurs. The magnetization is then brought back up to the transverse plane where an echo is produced and acquired at $t = 2\tau + \tau'$.

Magnetic Field Gradients

The importance of a highly homogeneous $\boldsymbol{B_0}$ field during some NMR measurements has been discussed in pervious sections. For other NMR experiments, a linearly varying magnetic field called a magnetic field gradient, $\boldsymbol{G}$, is deliberately applied generating a spatially varying magnetic field. Consequently, the Larmor frequency at which the spins precess will have a linearly spatial dependence. This technique is the basis for magnetic resonance imaging (MRI) and NMR measurements of translational motion. For now, the discussion will focus on the use of gradients for MRI. When a magnetic field gradient is applied, the spatially dependent magnetic field is expressed as

$$B(\boldsymbol{r}) = B_0 + \boldsymbol{G} \cdot \boldsymbol{r} \quad (2.30)$$

Where $\boldsymbol{r}$ is the position and $\boldsymbol{G}$ represent the amplitude and direction of the applied magnetic gradient. The effect of an applied magnetic field gradient on the magnetic field strength is demonstrated in Figure 2.11.

Recalling that $\omega_0 = \gamma B_0$, the spatially dependent frequency becomes

$$\omega(\boldsymbol{r}) = \gamma B_0 + \gamma \boldsymbol{G} \cdot \boldsymbol{r} \qquad (2.31)$$

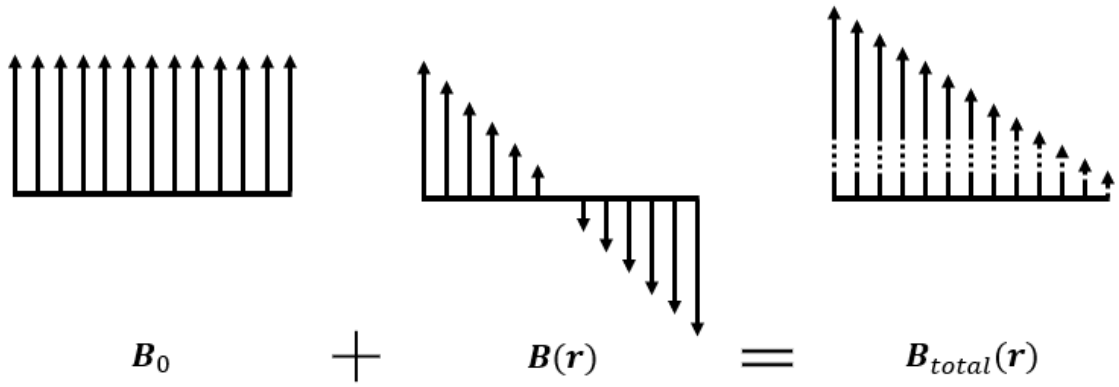

Figure 2.11. By applying a magnetic field gradient, a linearly varying magnetic field, $\boldsymbol{B(r)}$, is added to $\boldsymbol{B_0}$, resulting in a spatially varying total magnetic field, $\boldsymbol{B_{total}(r)}$. Note that $\boldsymbol{B_0}$ is in reality orders of magnitude larger than $\boldsymbol{B(r)}$.

$\boldsymbol{k}$-space and Magnetic Resonance Imaging

In the presence of a magnetic field gradient, the evolution of the signal amplitude resulting from a spin ensemble following a rf pulse is described by

$$S(t) = \iiint \rho(\boldsymbol{r}) \exp(i\gamma \boldsymbol{G} \cdot \boldsymbol{r} t)\, d\boldsymbol{r} \qquad (2.32)$$

where $\rho(\boldsymbol{r})$ is the spin density function, and t is the gradient pulse duration. The above equation can be simplified by introducing a reciprocal space vector, $\boldsymbol{k}$, which is proportional to the area under the applied gradient [8]

$$\boldsymbol{k} = \frac{\gamma t \boldsymbol{G}}{2\pi} \quad (2.33)$$

From Equation (2.34) it is apparent that this new reciprocal space, called *k*-space, can be traversed by varying either the duration, *t*, or the amplitude of $\boldsymbol{G}$. Substituting Equation (2.34) into Equation (2.33) yields the following Fourier relationship

$$S_N(\boldsymbol{k}) = \int \rho(\boldsymbol{r}) \exp(-i\boldsymbol{k} \cdot \boldsymbol{r})\, d\boldsymbol{r} \quad (2.34)$$

$$\rho(\boldsymbol{r}) = \frac{1}{2\pi} \int S_N(\boldsymbol{k}) \exp(i\boldsymbol{k} \cdot \boldsymbol{r})\, d\boldsymbol{k} \quad (2.35)$$

The spin density function, $\rho(\boldsymbol{r})$, produced by the above Fourier relationship represents the spatial signal amplitude distribution of a sample. Thus, an MR image is the reconstruction of the spin density distribution.

Alternatively, the NMR signal can be expressed in terms of the maximum signal before the gradient is applied, and a phase factor

$$S = S_0 \exp(i\varphi) \quad (2.36)$$

where φ is the accumulated phase shift of the spins at position $\boldsymbol{r}$ after the gradient duration t.

$$\varphi(\boldsymbol{r}) = \gamma \boldsymbol{G} \cdot \boldsymbol{r} t \quad (2.37)$$

During the application of a magnetic field gradient, the spin phases are allowed to evolve, winding up a ‘helix of phase’ as a function of the position as depicted in Figure 2.12. Following a 90° rf pulse, all spins at different positions along the gradient axis are perfectly in phase. Once the gradient is turned on, each spin will experience a different phase shift depending on its position forming a helix with wavelength $\lambda = \frac{2\pi}{\gamma G t}$ which

decreases with a stronger gradient or a longer duration. ***k*** is the inversely proportional to λ, so as λ gets shorter, more of *k*-space is traversed.

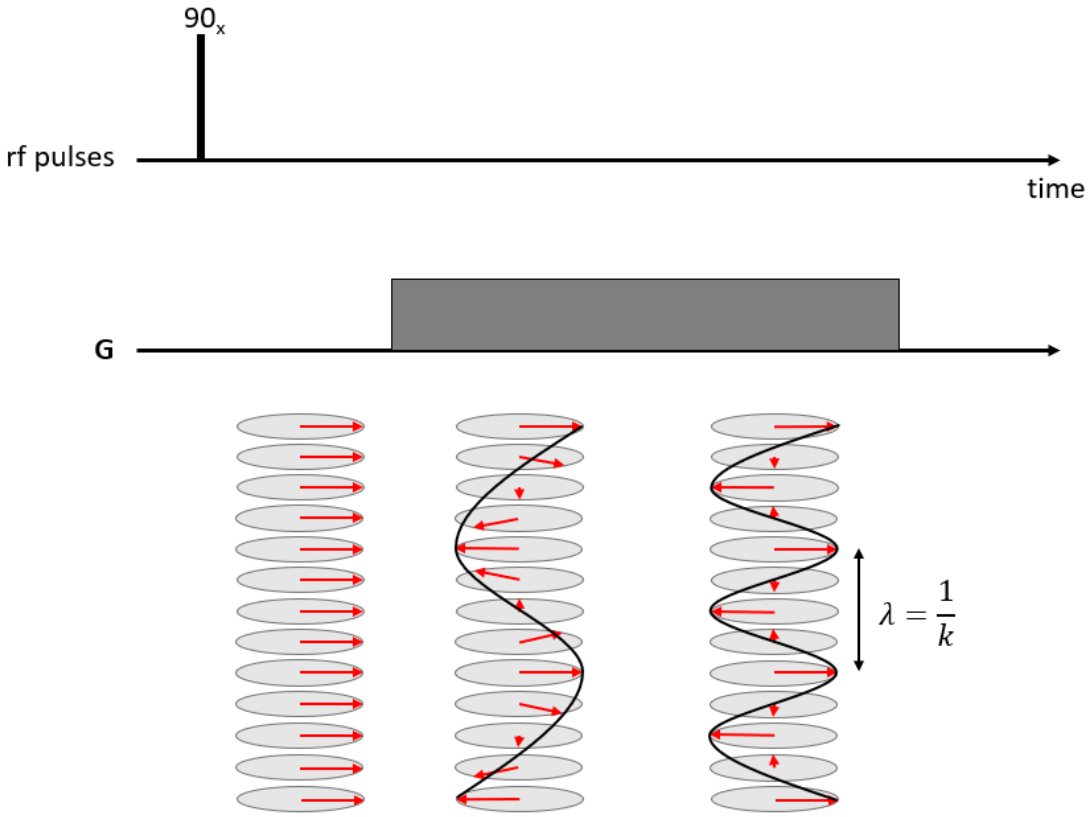

Figure 2.12. A 90° rf pulse followed by a steady gradient that winds up a helix of phase as portrayed bellow the pulse sequence. The longer the gradient is on, the more tightly wound the phase helix will be, resulting in a shorter and shorter wavelength, λ.

The winding of the phase helix can be reversed by applying a gradient of equal amplitude and length, but opposite sign, called a gradient echo (Figure 2.13), or by applying a 180° rf pulse followed by a gradient of equal amplitude, length, and sign called a spin echo (Figure 2.14). The spins will rephase resulting in an echo which is essential for data acquisition. A perfect echo is only possible if the spins remain fixed in their original position, something that is not realistic during the application of longer time

varying gradients. However, any translational motion of the spins during the phase evolution becomes embedded in the final phase distribution, so this type of gradient sequences is typically used to encode for displacement. Displacement encoding will be discussed in a later section.

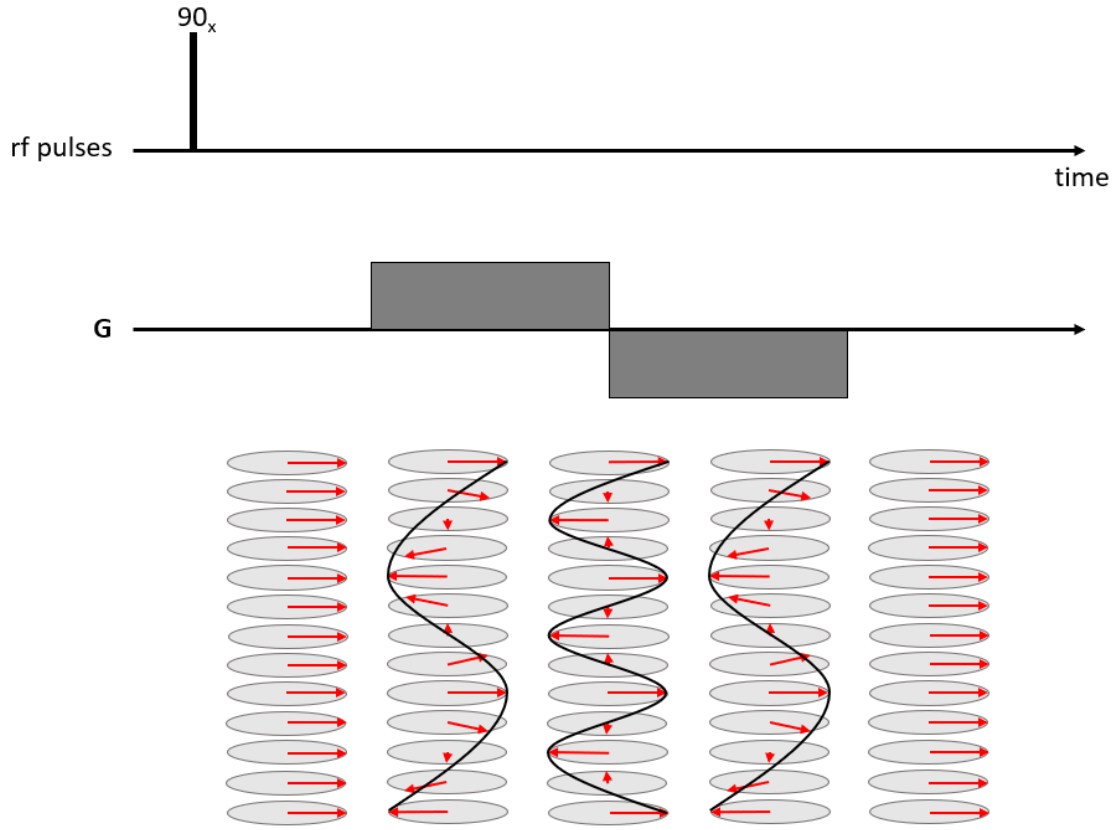

Figure 2.13. The gradient echo reverts the winding of the phase helix by applying a gradient of equal amplitude and duration, but opposite sign. As the name of the sequence implies, and echo is formed once complete phase coherence is attained.

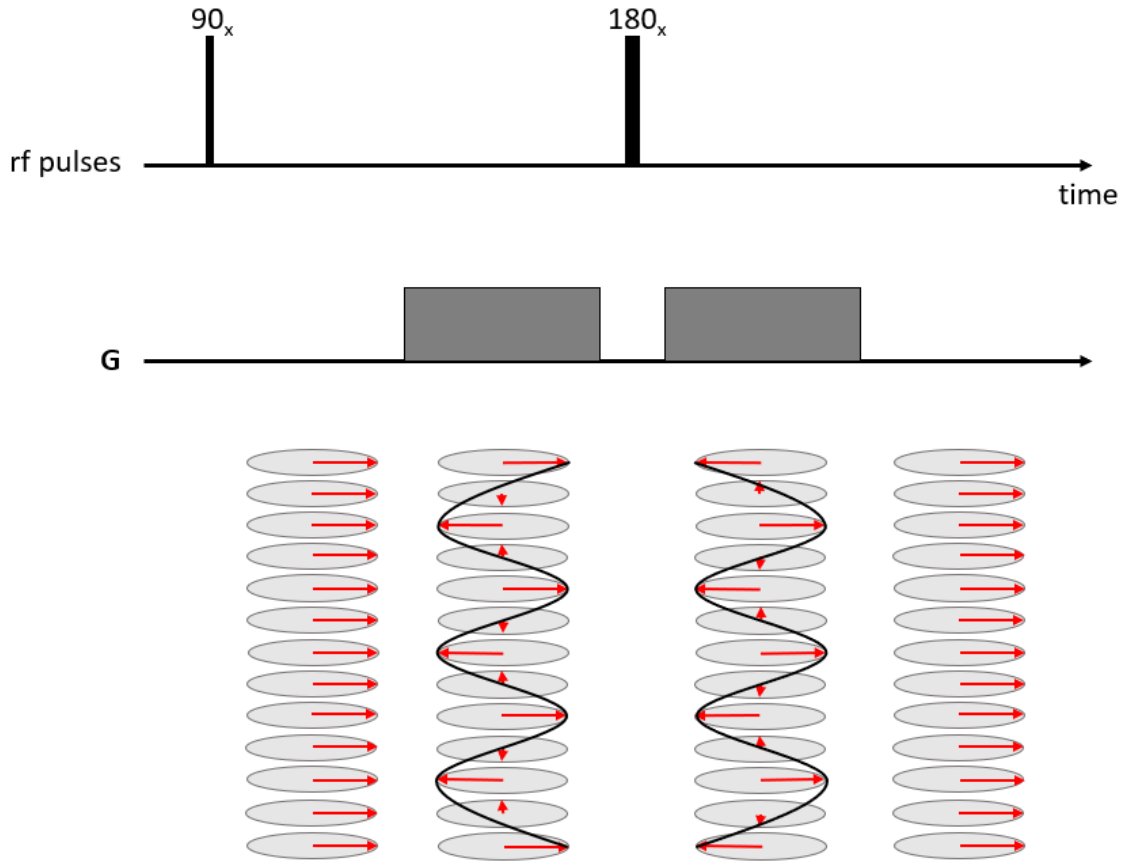

Figure 2.14. The spin echo sequence reverts the winding of the phase helix by applying a 180° rf pulse followed by a gradient of equal amplitude, duration, and sign. In this case, it is the 180° rf pulse that changes the direction of the phase evolution of the spins. Again, an echo is produced once phase coherence is attained.

***k*-space Encoding**

To produce a well resolved MR image with good contrast, a larger portion of *k*-space must be sampled. Two methods of traversing and sampling *k*-space are used in imaging sequences. The first method, known as phase-encoding, is executed by stepping through various gradient amplitudes in a systematic order. These gradients are called phase-gradients and are denoted G_{phase}. Phase-gradients will wind up the phase helix until a specific point in *k*-space is reached, and signal will then be acquired for that one

point. The second method is known as frequency encoding and is executed by acquiring the signal over a time *t* at constant gradient amplitude. These gradients are called read-gradients and are denoted G_{read}. By acquiring the signal during a constant gradient, an entire line of k-space is sampled rather than a single point, making this method much more time efficient. However, because the signal is collected during the applied gradient, imaging artifacts are more likely when frequency encoding is used. Figure 2.15 and 2.16 illustrate imaging sequences using phase encoding and frequency encoding, respectively, along with their subsequent *k*-space trajectories.

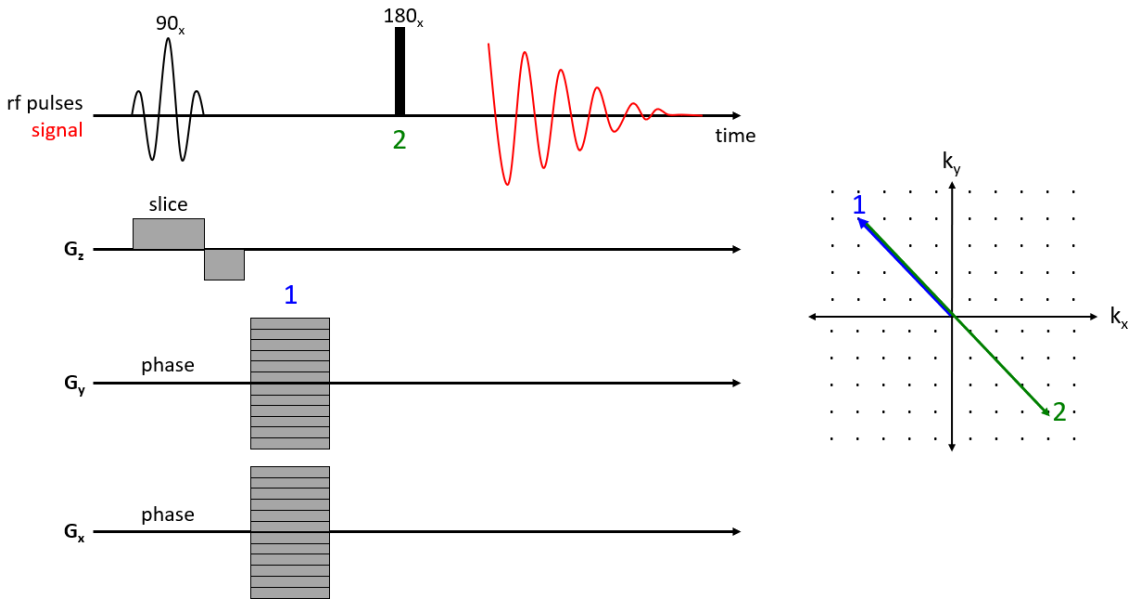

Figure 2.15. This pulse sequence is a 2D-imaging pulse sequences using pure phase encoding and the associated *k*-space trajectory. The 90° pulse and the slice gradients excite spins in a plane normal to the z-axis, the x and y phase gradients cause a traverse to a specific point in *k*-space by winding up the phase helix (1), and the 180° rf pulse inverts the spin phases (2), allowing an echo to be formed. The echo signal is then acquired. This process must be repeated N^2 times until signal is acquired from enough points to produce an image.

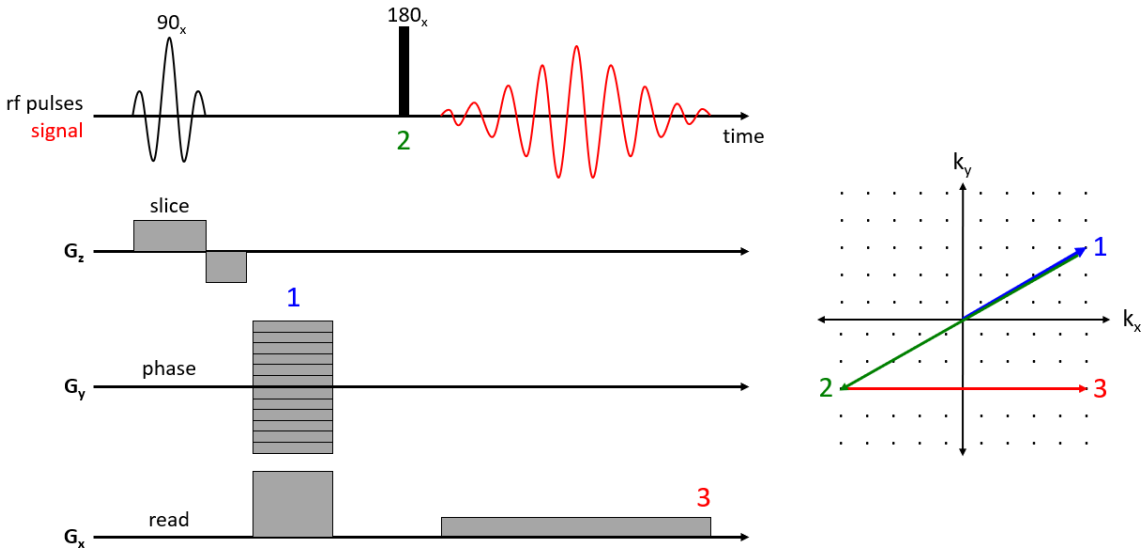

Figure 2.16. The above pulse sequence and the associated *k*-space trajectory is a different 2D-imaging sequence using both phase and read encoding. Again, a plane normal to the z-axis is selected, and the first set of gradients cause a traverse to a point at the edge of *k*-space (1). The 180° rf pulse inverts the spin phases (2), allowing an echo to be formed. The echo signal is acquired during an applied read gradient (3) so that an entire line of k-space is sampled rather than a single point. Hence, the above sequence needs to be repeated only *N* times to obtain an image.

Every point in *k*-space contains information about the entire final image. The center of *k*-space contains information about the general contrast of the image, while the outer regions provide the finer details such as borders and contours. Thus, the further out *k*-space is sampled, the better is the resolution of the final MR image.

References

1. Callaghan, P.T., *Translational Dynamics & Magnetic Resonance: Principles of Pulsed Gradient Spin Echo NMR*. 2011, New York: Oxford University Press.

2. Bloch, F., *Nuclear Induction.* Physical Review, 1946. **70**(7-8): p. 460-474.

3. Hahn, E.L., *Spin Echoes.* Physical Review, 1950. **77**(5): p. 746-746.

4. Carr, H.Y. and E.M. Purcell, *Effects of Diffusion on Free Precession in Nuclear Magnetic Resonance Experiments.* Physical Review, 1954. **94**(3): p. 630-638.

5. Meiboom, S. and D. Gill, *Modified Spin-Echo Method for Measuring Nuclear Relaxation Times.* Review of Scientific Instruments, 1958. **29**(8): p. 688-691.

6. Wanlass, L.K. and J. Wakabayashi, *Stimulated Spin-Echo Measurement of Cross-Relaxation in Neutron-Irradiated Calcite.* Physical Review Letters, 1961. **6**(6): p. 271-+.

7. Hoult, D.I. and R.E. Richards, *Critical Factors in Design of Sensitive High-Resolution Nuclear Magnetic-Resonance Spectrometers.* Proceedings of the Royal Society of London Series a-Mathematical Physical and Engineering Sciences, 1975. **344**(1638): p. 311-340.

8. Mansfield, P. and P.K. Grannell, *NMR Diffraction in Solids.* Journal of Physics C-Solid State Physics, 1973. **6**(22): p. L422-L426.

ADVANCED NMR TOPICS

Molecular Self-Diffusion and Propagators

Molecular self-diffusion was first described by Albert Einstein as the random motion of molecules driven by thermal energy. Based on this idea, an equation for self-diffusion known as the Sutherland-Einstein relation was formulated

$$D = \frac{k_B T}{6\pi\eta R} \quad (3.1)$$

where k_B is the Boltzmann constant, T is the temperature, η is the viscosity, and R is the effective particle size. Equation (3.1) allowed for the interpretation of Fick's law for diffusion in terms of probability densities. Thus, the Brownian motion of molecules as well as self-diffusion processes can be described by propagators which specify the probability that a molecule has travelled a certain distance in a given amount of time. Because NMR deals with spin ensembles, it is useful to introduce an average propagator to describe the probability of displacement:

$$\bar{P}(\boldsymbol{R}, t) = \int \rho(\boldsymbol{r}) P(\boldsymbol{r}|\boldsymbol{r} + \boldsymbol{R}, t)\, d\boldsymbol{r} \quad (3.2)$$

$\bar{P}(\boldsymbol{R}, t)$ represents the probability that spins with an original spin density $\rho(\boldsymbol{r})$ have travelled a distance $\boldsymbol{R}$ over a time t where $\boldsymbol{R} = \boldsymbol{r}' - \boldsymbol{r}$, where $\boldsymbol{r}$ is any starting position and $\boldsymbol{r}'$ is any final position. For self-diffusion and Brownian motion, the average propagator results in a normalized Gaussian probability distribution which evolves with time. The successive evolution of the Gaussian distributions in time is shown in Figure 3.1.

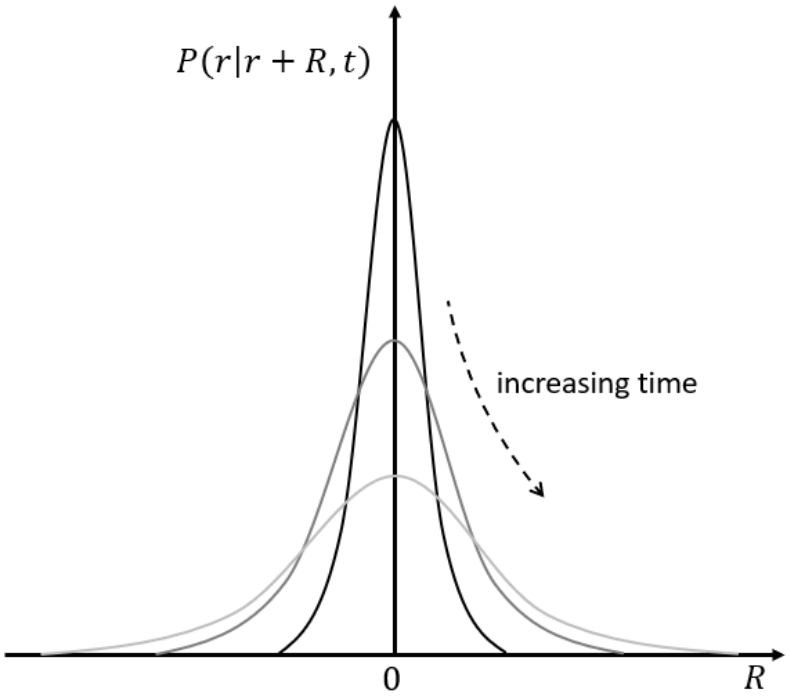

Figure 3.1. Displacement probability distribution for an ensemble of particles undergoing Brownian motion. The broadening of the Gaussian with increasing time indicates a decreased probability of finding a particle at the starting position, x_0.

Finally, the relationship between molecular displacement and self-diffusion, known as the Einstein definition, is given in Equation (3.3) and (3.4), respectively.

$$\langle (x' - x)^2 \rangle = 2Dt \quad (3.3)$$

$$\langle (\boldsymbol{r}' - \boldsymbol{r})^2 \rangle = 6Dt \quad (3.4)$$

Where $\langle (x' - x)^2 \rangle$ is the mean squared displacement in one dimension, and $\langle (\boldsymbol{r}' - \boldsymbol{r})^2 \rangle$ is the mean squared displacement in three dimensions.

Normalized Echo Signal

NMR measurements can be used to detect molecular motion by comparing the initial position of a spin to its position at a later time. Following an initial phase encoding gradient pulse, spins migrating during the measurement will accumulate a phase shift. At a later time, a second gradient pulse is applied, and if the over-all displacement is non-zero, a residual phase shift caused by translational motion is detected in the acquired echo signal. In NMR experiments that encode for motion, time varying gradients, $\boldsymbol{g}(t)$, are normally used to produce an echo. A requirement for the construction of an echo is $\int_0^t \boldsymbol{g}(t')dt' = 0$ as this is a necessary condition for rephasing of the phase helix. Any translational motion occurring during a measurement will cause attenuation of the echo amplitude, so it is convenient to introduce the concept of a normalized echo amplitude, where the magnetization influenced by residual phase shifts is compared to the magnetization before any gradients are applied. The normalized echo amplitude can be expressed as

$$E(t) = \frac{M_+(t)_{\boldsymbol{g}^*(t')\neq 0}}{M_+(t)_{\boldsymbol{g}^*(t')=0}} \quad (3.5)$$

where $\boldsymbol{g}^*(\boldsymbol{t})$ is the effective gradient carrying the actual sign at time *t*. Normalizing the echo amplitude according to Equation (3.5) eliminates relaxation effects, leaving only the effect of the gradient. As a side note, lower case $\boldsymbol{g}(t)$ will be used in the discussion for motion measurements to distinguish the gradients from those used for imaging.

Moments of the Gradient

In systems where the spins are experiencing coherent motion, the residual phase shift accumulated for a spin *j* at time *t* during a measurement using effective gradients is given by

$$\varphi_j(t) = \gamma \int_0^t \boldsymbol{g}^*(t') \cdot \boldsymbol{r}_j(t') dt' \quad (3.6)$$

where $\boldsymbol{r}_j(t')$ is the path of the spin. The accumulated phase shift can be analyzed considering the moments of the gradient waveform. This is done by first expanding the spin position in a Taylor series expansion

$$\boldsymbol{r}(t) = \boldsymbol{r}_0 + \boldsymbol{v}_0 t + \frac{1}{2}\boldsymbol{a}_0 t^2 + \cdots \quad (3.7)$$

where $\boldsymbol{r}(0)$ is the initial spin position, $\boldsymbol{v}(t)$ is the velocity, and $\boldsymbol{a}(t)$ is the acceleration. Using the Taylor expansion of the spin position, the phase shift can be written

$$\varphi_j(t) = \gamma \left[\boldsymbol{r}_0 \int_0^t \boldsymbol{g}^*(t') dt' + \boldsymbol{v}_0 \int_0^t \boldsymbol{g}^*(t') t' dt' + \boldsymbol{a}_0 \int_0^t \boldsymbol{g}^*(t') t'^2 dt' + \cdots \right] \quad (3.8)$$

The integrals in Equation (3.8) represent the zeroth, first, and second moment of the gradient waveform. To ensure the echo condition, the zeroth moment must equal zero, and therefore does not contribute to the phase shift nor the accumulated echo amplitude

$$m_0 = \int_0^t \boldsymbol{g}^*(t') dt' = 0 \quad (3.9)$$

The first moment, the second integral of Equation (3.8), is the velocity contribution to the normalized echo amplitude, and the second moment, the third integral of Equation (3.8),

is the acceleration contribution to the normalized echo amplitude. The first and second moment are given by

$$m_1 = \int_0^t \boldsymbol{g}^*(t')t'dt' = g\delta\Delta \quad (3.10)$$

$$m_2 = \int_0^t \boldsymbol{g}^*(t')t'^2dt' = g\delta^2\Delta \quad (3.11)$$

where δ is the gradient pulse duration and Δ is the time between two gradient pulses. The normalized echo amplitude can then be expressed in terms of the gradient moments

$$E(t) = exp\left(i\gamma\boldsymbol{v}\cdot\int_0^t t'\boldsymbol{g}^*(t')dt' + i\gamma\boldsymbol{a}\cdot\int_0^t t'^2\boldsymbol{g}^*(t')dt' + \cdots\right) \quad (3.12)$$

With knowledge of the various gradient moments, pulse sequences can be designed to encode for either velocity, acceleration, or higher order moments excluded from the above equations by zeroing other moments. This is done by choosing a specific time dependence for $\boldsymbol{g}^*(t)$.

Stejskal-Tanner Experiment and *q*-space

In 1965, Stejskal and Tanner demonstrated that self-diffusion can be measured using a NMR pulse sequence known as the pulsed gradient spin-echo sequence (PGSE) [1]. The two most common pulse sequences used for diffusion encoding are the pulsed gradient spin echo (referred to as PGSE), and the pulsed gradient stimulated echo (referred to as PGStE from here on). The PGSE and PGStE pulse sequences are shown in Figure 3.2. Both pulse sequences consist of a combination of rf pulses, rectangular gradient pulses of duration δ, and an observation time, Δ, which is the time separating the

start of the gradient pulses and the time over which diffusion occurs. The use propagator formalism to describe molecular translational motion, the narrow gradient pulse condition must be met, meaning that the gradient pulses must be sufficiently short that any molecular motion occurring over δ can be neglected. Thus, the narrow gradient pulse condition is often expressed as $\delta \ll \Delta$.

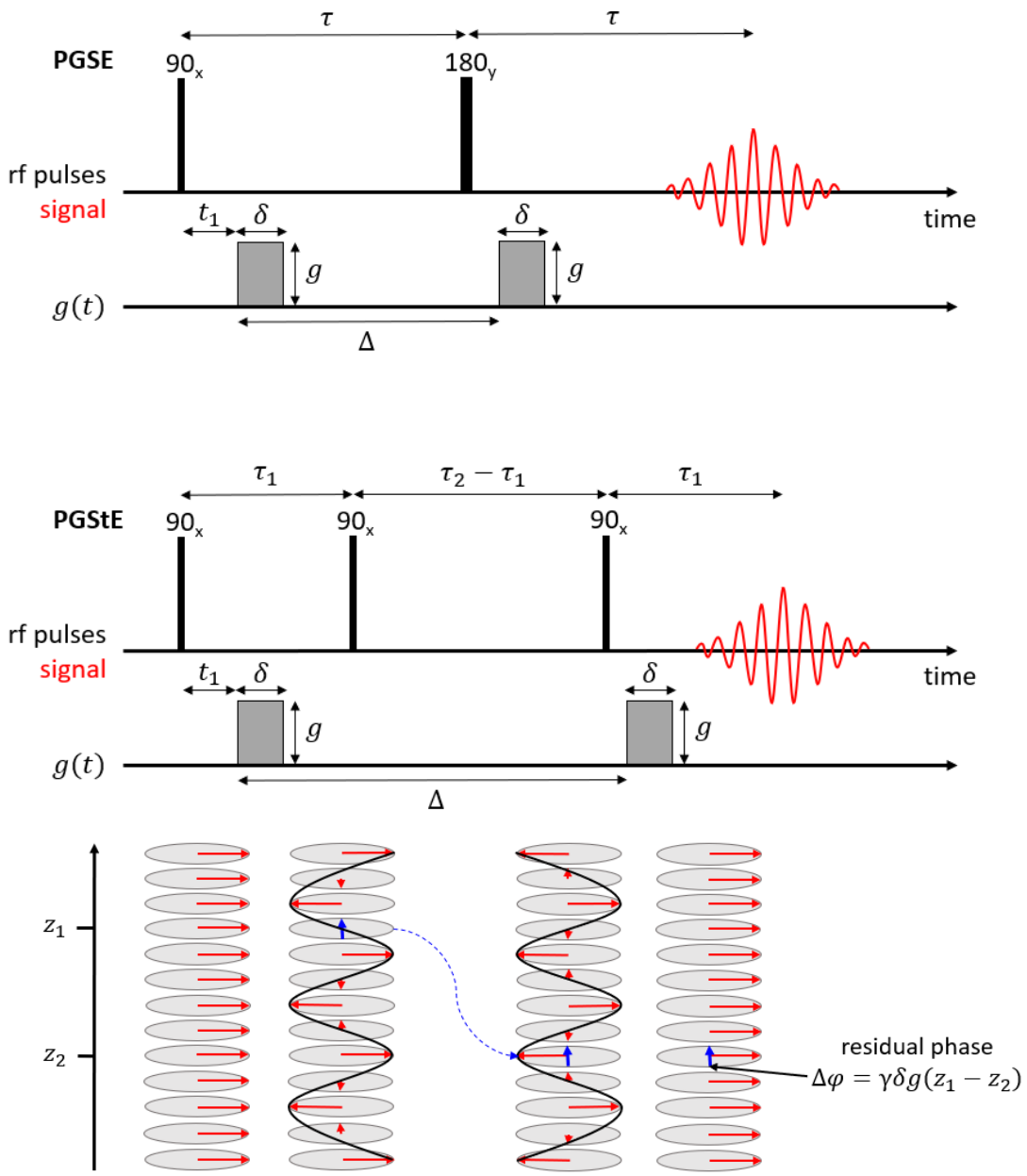

Figure 3.2. The PGSE sequence (top) and the PGStE sequence (bottom) can be used to encode for self-diffusion. The first gradient winds up a helix of phase followed by an observation time, Δ. During the observation time, the spins experiencing Brownian motion will travel to a new position while carrying their phase with them (shown in blue in the above phase helix evolution). The second gradient unwinds the phase helix, and the spins that relocated during the period Δ will retain a residual phase shift, $\Delta\varphi$, which can be obtained from the acquired echo signal and used to characterize the self-diffuison of a spin ensemble.

The first gradient imparts a phase shift $\gamma\delta\boldsymbol{g}\cdot\boldsymbol{r}$ on a spin at location $\boldsymbol{r}$. Following the final gradient, the residual net phase of a spin is $\Delta\varphi = \gamma\delta\boldsymbol{g}(\boldsymbol{r}' - \boldsymbol{r})$. If the spin does not move during the period Δ, the residual phase shift is zero and no echo attenuation is observed. It should be noted that the two pulse sequences in Figure 3.2 are equivalent in terms of motion-induced phase shifts. However, in the PGStE sequence, the magnetization vector is stored along the -z-axis in-between gradient pulses, eliminating magnetization decay due to spin-spin relaxation. Consequently, the PGStE sequence is particularly well suited for systems where $T_2 < T_1$. The normalized echo attenuation due to the phase shifts across the spin ensemble is known as the Stejskal-Tanner relation and is given by the following equation

$$E(g) = \exp\left(-\gamma^2 g^2 \delta^2 D(\Delta - \delta/3)\right) \quad (3.13)$$

where D is the diffusion coefficient, and the exponent is proportional to the mean-squared molecular displacement over the period $\Delta - \delta/3$. Equation (3.13) assumes only Brownian motion in the system and is often simplified by introducing a new variable $b = \gamma^2 g^2 \delta^2(\Delta - \delta/3)$. By plotting the natural log of the echo amplitude, $\ln(E(g))$, vs b, the slope of the plot equals $-D$, and the apparent diffusion coefficient, D_{app}, can be extracted. Thus, D_{app} is the value of the diffusion coefficient obtained by a PGSE experiment and is identical to the self-diffusion, D_0, in an unrestricted environment. However, in an environment restricted by surfaces and boundaries, such as porous media, its value may be influenced by the observation time Δ used in that specific measurement. In this case, D_{app} is often referred to as the effective diffusion coefficient, D_{eff}, which depends on the time dependence of the mean-squared displacement, resulting in

$D_{eff} < D_0$ for long Δ-times. D_{eff} will be described in more detail in a later section.

In the case of an additional coherent motion, Equation (3.13) can be expanded to include the first term of Equation (3.12) resulting in an expression that accounts for both the attenuation due to diffusion and a phase shift due to flow

$$E(\boldsymbol{g}) = \exp\left(i\gamma\delta\boldsymbol{g}\cdot\boldsymbol{v}\Delta - \gamma^2 g^2\delta^2 D(\Delta - \delta/3)\right) \quad (3.14)$$

where $\boldsymbol{v}$ is the coherent flow velocity.

Stejskal also suggested the use of propagators to describe the probability of generalized motion [2]. The normalized echo amplitude as a function of the gradient strength, $\boldsymbol{g}$, and the observation time, Δ, is given by

$$E(\boldsymbol{g},\Delta) = \int \rho(\boldsymbol{r}) \int P(\boldsymbol{r}|\boldsymbol{r}',\Delta)\exp(i\gamma\delta\boldsymbol{g}\cdot[\boldsymbol{r}-\boldsymbol{r}'])\,d\boldsymbol{r}'d\boldsymbol{r} \quad (3.15)$$

Equation (3.15) closely resembles Equation (2.35) in the Fourier relationship used for *k*-space analysis, and consequently lends itself well to a new reciprocal space analogy. While $\boldsymbol{k}$ describes the static displacement, $\boldsymbol{r}$, of spins, the new reciprocal space vector, denoted $\boldsymbol{q}$, describes the dynamic displacement $\boldsymbol{R}$ of spins in terms of spin phase behavior.

$$\boldsymbol{q} = \frac{\gamma\delta\boldsymbol{g}}{2\pi} \quad (3.16)$$

Equation (3.15) can now be rewritten in terms of $\boldsymbol{q}$

$$E(\boldsymbol{q},\Delta) = \int \rho(\boldsymbol{r}) \int P(\boldsymbol{r}|\boldsymbol{r}',\Delta)\exp(i2\pi\boldsymbol{q}\cdot[\boldsymbol{r}-\boldsymbol{r}'])\,d\boldsymbol{r}'d\boldsymbol{r} \quad (3.17)$$

Using the definition of the average propagator given in Equation (3.2), a Fourier relationship between the normalized echo signal and the average displacement probability density is obtained

$$\bar{P}(\boldsymbol{R}, t) = \int \rho(\boldsymbol{r}) P(\boldsymbol{r}|\boldsymbol{r} + \boldsymbol{R}, \Delta) d\boldsymbol{r} \quad (3.18)$$

$$E(\boldsymbol{q}, \Delta) = \int \bar{P}(\boldsymbol{R}, \Delta) \exp(i2\pi \boldsymbol{q} \cdot \boldsymbol{R})\, d\boldsymbol{R} \quad (3.19)$$

From this Fourier relationship, it is clear that by measuring the echo signal in *q*-space, an image of the displacement probability can be produced. During *k*-space imaging, a distribution of spin density is obtained, while during *q*-space imaging, a distribution of spin displacement is obtained.

At this point, it is convenient to introduce a simplified version of the echo attenuation equation valid in the low *q*-limit. If the molecular displacement taking place is due to Brownian motion only, i.e. there is no coherent flow in the system, the echo attenuation can be expressed by the following equation

$$E(\boldsymbol{q}, \Delta) \approx 1 - \frac{1}{2} q^2 \langle Z^2(\Delta) \rangle \quad (3.20)$$

which allows for measuring the mean squared displacement directly. The simplified expression in Equation (3.20) becomes particularly useful in the case of restricted diffusion where it can be used to obtain information about length scales in porous systems.

The Bloch-Torrey Equation for Diffusion and Flow

A method for describing the spin phase evolution taking the effects of position, advection, and spin-spin relaxation into account was developed by Torrey in 1956 [3]. His approach is based on the Bloch equations and effectively treats the magnetization as a

fluid. The equation describing the 'transport of the magnetization' is known as the Bloch-Torrey equation

$$\frac{\partial M_+}{\partial t} = -i\gamma \boldsymbol{r} \cdot \boldsymbol{g}^*(t) M_+ - \frac{M_+}{T_2} + D\nabla^2 M_+ - (\boldsymbol{v} \cdot \nabla) M_+ \qquad (3.21)$$

The above version of the Bloch-Torrey equation assumes a scalar diffusion coefficient and is the time evolution of the transverse magnetization vector, $M_+ = M_x + iM_y$, in the rotating reference frame. The solution to Equation (3.21) is

$$M_+(\boldsymbol{r}, t) = A(t) exp\left(-i\gamma \boldsymbol{r} \cdot \int_0^t \boldsymbol{g}^*(t')dt'\right) \exp(-t/T_2) \qquad (3.22)$$

where $A(t)$ is a modulation factor determined by the spreading motion of the spin bearing molecules through diffusion and flow, the first exponential is a helical phase distribution that equals 1 at the echo center, and the second exponential describes the spin-spin relaxation. If the echo condition, $\int_0^t \boldsymbol{g}^*(t')dt' = 0$, is met, $A(t)$ becomes the normalized echo amplitude

$$E(t) = exp\left[-D\gamma^2 \int_0^t \left(\int_0^{t'} \boldsymbol{g}^*(t'')dt''\right)^2 dt'\right] exp\left[i\gamma \boldsymbol{v} \cdot \int_0^t \int_0^{t'} \boldsymbol{g}^*(t'')dt''dt'\right] \qquad (3.23)$$

The above expression of the Bloch-Torrey equation is accurate only if the signal is evaluated at the echo center. If this condition is met, and isotropic diffusion is assumed, Equation (3.23) can be used to evaluate the spin phase distribution for the PGSE sequence. By evaluating the Bloch-Torrey integrals in Equation (3.23) using the time intervals in a PGSE sequence, the zeroth and first moment are obtained from the first two integrals, while the last integral produces an expression that represent the diffusion induced echo attenuation in Equation (3.13)

$$\int_0^{2\tau} \boldsymbol{g}^*(t')dt' = 0 \quad (3.24)$$

$$\int_0^t \int_0^{t'} \boldsymbol{g}^*(t'')dt''dt' = -\boldsymbol{g}\delta\Delta \quad (3.25)$$

$$\int_0^t \left(\int_0^{t'} \boldsymbol{g}^*(t'')dt'' \right)^2 dt' = g^2\delta^2(\Delta - \delta/3) \quad (3.26)$$

Equation (3.24) is simply the echo condition, Equation (3.25) is the first moment representing the coherent flow contribution to the echo amplitude, and Equation (3.26) represents the diffusion contribution to the echo amplitude.

Restricted Diffusion

The ability to measure restricted diffusion by means of NMR has become a topic of great interest in a variety of fields due to the correlation between the diffusion coefficient and the microstructure of a porous structure. Diffusion measurements are essential to understanding the transport processes in complex porous structures, both for stationary fluids and flow through the porous media. The PGSE experiment lies at the heart of these measurements due to its ability to non-invasively probe the molecular displacement which is proportional to the diffusion coefficient value. In a stationary bulk fluid, the PGSE experiment will return a diffusion coefficient equivalent to the self-diffusion coefficient, D_0, of that particular fluid. In a confining geometry, the measured diffusion coefficient is referred to as the effective diffusion coefficient, D_{eff}, and is a function of the diffusion time, or the observation time, Δ, when it is measured using the PGSE sequence. Using the Einstein definition from Equation (3.4), D_{eff} is given by

$$D_{eff} = \frac{\langle (\boldsymbol{r}(t) - \boldsymbol{r}(0))^2 \rangle}{6t} \quad (3.27)$$

Figure 3.3 depicts two different porous system, one consisting of isolated pores (*left*) with pore diameter *d*, and one consisting of an interconnected porous network (*right*) where *d* represents the diameter of the pores. At short diffusion times, most molecules have yet to experience wall collisions, and the measured diffusion coefficient is approximately equal to the self-diffusion. As $t \to \infty$, the molecules sample more of the pore space, experiencing several wall collisions, and the measured diffusion coefficient is reduced. In a porous structure with isolated pores, $D(t) \to 0$ because the mean squared displacement averages to zero after numerous wall collisions. In an interconnected porous network, the molecules also experience numerous wall collisions, but will also travel between different pores, and $D(t) \to D_{eff}(\infty)$.

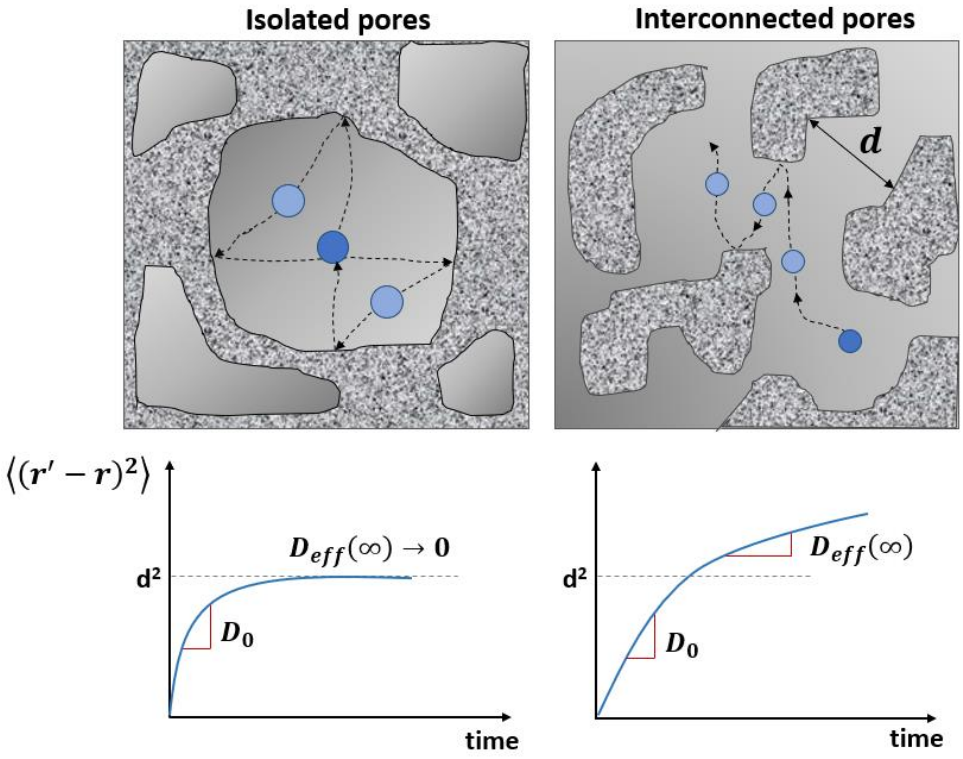

Figure 3.3. The measured diffusion coefficient as a function of the observation time in a PGSE experiment for isolated pores (left) and an interconnected porous structure (right). Redrawn from [4]. In isolated pores, the motion of the particles will average out and $D_{eff} \rightarrow 0$ at long observation times. In an interconnected porous structure, a decreased diffusion coefficient, $D_{eff} < D_0$, is observed at long times.

$D_{eff}(\infty)$ can be used to obtain the tortuosity, α, of a porous medium. The tortuosity is used to characterize the connectivity of an interconnected porous matrix and is therefore highly correlated to the permeability of a porous medium. The relationship between D_{eff} and α is given by

$$\lim_{t\to\infty} \frac{D_{eff}(t)}{D_0} = \frac{D_{eff}(\infty)}{D_0} = \frac{1}{\alpha} \qquad (3.28)$$

The larger the ratio of D_{eff} and D_0 is the higher the tortuosity. Thus, a higher tortuosity corresponds to lower connectivity, and therefore also a lower permeability.

Spin Relaxation in Inhomogeneous Porous Media

In PGSE experiments where longer values of the diffusion observation time, Δ, are needed, spin relaxation effects cannot be avoided. The structure and geometry of porous media affects the spin relaxation rate, thus knowledge about how spin relaxation is affected by a restrictive environment is essential in interpreting the echo attenuation signal. This section will discuss two different methods in which the interplay between diffusion and relaxation in porous media may be described.

The first method will be referred to as the exchange model for multi-site relaxation, where molecules exchange between domains with different relaxation times. Different relaxation rates are assigned to different physical regions of the sample, and diffusion causes molecules to migrate or exchange between these regions. The relaxation time for region *i* is denoted $T^{(i)}$, and can represent either T_1 or T_2 relaxation. The spin occupancy of the region is given by P_i, and of course $\sum_i P_i = 1$. The rate of exchange between different regions is given by the exchange time, τ_E, and can be defined as either slow exchange, where the condition $T^{(i)} \ll \tau_E$ must be met, intermediate exchange, or fast exchange, where $T^{(i)} \gg \tau_E$ is required. In the case of slow exchange, the total magnetization decay due to relaxation is multi-exponential and is given by

$$\frac{M(t)}{M_0} = \sum_i P_i \exp\left(-\frac{t}{T^{(i)}}\right) \quad (3.29)$$

In the case of fast exchange, a common relaxation rate, given by Equation (3.30) for the whole spin system is observed, and thus the magnetization decay due to relaxation is single-exponential and is given by Equation (3.31)

$$\frac{1}{T} = \sum_i P_i \frac{1}{T^{(i)}} \quad (3.30)$$

$$\frac{M(t)}{M_0} = exp\left(-\frac{t}{T}\right) \quad (3.31)$$

Intermediate exchange rates result in non-exponential decays and cannot be explained using the above methods.

Brownstein-Tarr Theory

In a porous media where molecules experience restricted diffusion, the spin relaxation is highly influenced by the geometry of the pore structure. Thus, the second method describing the interplay between diffusion and relaxation in an inhomogeneous media uses a geometric description of spin relaxation in which the relaxation in the bulk fluid, T_B, is distinguished from the relaxation that occurs at the surface of the solid matrix, T_S. The relaxation that occurs when molecules collide with the surface of the solid matrix is of particular importance due to the strong relaxation "sinks" that exist there, and the strength of the effect of this surface relaxation on the measured relaxation rate is therefore highly dependent on both pore sizes and diffusion rates. The relaxation effects deriving from surface collisions have been described in detail by Brownstein and Tarr [5] using the classical magnetization diffusion approach developed by Bloch and Torrey. By assigning a magnetization density that obeys Fick's law [6], $M(\boldsymbol{r}, t)$ describes

the probability of finding the spin at position $\boldsymbol{r}$ at time *t* given it has not relaxed due to surface interactions. The differential equation becomes

$$D\nabla^2 M(\boldsymbol{r},t) = \frac{\partial M(\boldsymbol{r},t)}{\partial t} \quad (3.32)$$

where $M(\boldsymbol{r},t)$ can refer to either spin-lattice or spin-spin relaxation. The normal mode solution to the differential equation as written by Brownstein and Tarr is

$$M(t) = M_0 \sum_{n=0}^{\infty} I_n \, exp\left(-\frac{t}{T_n}\right) \quad (3.33)$$

where I_n is the relative contribution of a normal mode, and $I_n = a_n \int_V d\boldsymbol{r}\, u_n$. The sum of I_n equals unity. u_n and T_n are the eigenfunctions and eigenvalues of the Helmholtz equation

$$\frac{u_n}{T_n} + D\nabla^2 u_n = 0 \quad (3.34)$$

The geometric aspect of the Brownstein-Tarr description is found in the variables I_n and T_n which depend on the self-diffusion coefficient, D, the pore shape and size, a, and the average surface relaxation sink strength, $\bar{\rho}$, which is also known as the surface relaxivity. Specific solutions to I_n and T_n have been derived for planar pore geometry, cylindrical pore geometry, and spherical pore geometry, but will not be included in this thesis. However, it should be noted that for all geometries, I_n and T_n vary as a function of $\bar{\rho}a/D$.

Again, there are two limiting cases to consider; the fast-exchange limit and the slow-exchange limit. The fast-exchange limit is defined as $\bar{\rho}a/D \ll 1$, which means that the rate of diffusion of magnetization delivered to the surface of the solid matrix is much

larger than the surface relaxivity, ρ. This limiting case is therefore also referred to as the "fast-diffusion" limit. In the case of the fast-diffusion limit, the relaxation is a single mode featuring single-exponential decay and is dominated by the slowest relaxation mode $T_0^{-1} \sim a/\bar{\rho}$. In the case of slow exchange, $\bar{\rho}a/D \gg 1$, the surface relaxation rate, ρ, is much larger than the rate at which diffusion can deliver magnetization to the surface. Thus, the slow-exchange limit is often referred to as "diffusion-limited" exchange. The diffusion limited regime depends on higher order relaxation modes as well as the slowest mode and features multi-exponential relaxation. The slowest relaxation mode is given by $T_0^{-1} \sim a^2/D$. The higher order relaxation modes, T_n^{-1}, can only be observed in the diffusion limited regime, are virtually independent of ρ, and are of order $a^2/n^2\pi^2 D$. This relationship provides the means to estimate the range of pore sizes in the inhomogeneous media. Reliable estimates of ρ are difficult to obtain, however, in combination with q-space imaging, the Brownstein-Tarr model can be used to characterize pore structure and geometry.

In the case of an inhomogeneous porous media with pore sizes at the order of 10 microns or smaller, the fast diffusion limit applies, and the relaxation rates are directly related to the surface to volume ratio of the pores. For larger pores, the relaxation rate of the bulk fluid will contribute. The overall T_1 and T_2 relaxation rate of the fluid in a porous media is given by the following equations

$$\frac{1}{T_1} = \frac{1}{T_{1B}} + \frac{1}{T_{1S}} \quad (3.35)$$

$$\frac{1}{T_2} = \frac{1}{T_{2B}} + \frac{1}{T_{2S}} + \frac{1}{T_{2D}} \quad (3.36)$$

where T_B is the contribution of the bulk relaxation, T_S is the surface relaxation contribution and $\frac{1}{T_{1,2S}} = \rho_{1,2}\frac{S}{V}$, where $\rho_{1,2}$ are the surface relaxivities for T_1 or T_2 relaxation. T_D is a diffusion term that allows for echo attenuation due to local inhomogeneous magnetic fields which can be ignored if the CPMG sequence is executed with sufficiently short echo times, τ_E. For small pores, when the fast-diffusion limit applies, the bulk relaxation term can also be ignored, and the relaxation rate simplifies to

$$\frac{1}{T_{1,2}} = \rho_{1,2}\frac{S}{V} \quad (3.37)$$

A distribution of pore sizes will result in a multiexponential signal decay, and by using an inverse Laplace transformation technique, a relaxation rate distribution can be obtained.

Inverse Laplace Transformations

In an inhomogeneous media where a distribution of pore sizes results in a multiexponential signal decay, an inverse Laplace transformation of the signal decay returns a distribution of the various relaxation rates.

$$f(R) = \mathcal{L}^{-1}\{S(t)\} \quad (3.38)$$

$$S(t) = \mathcal{L}\{f(R)\} = \int_0^\infty f(R)\exp(-Rt)\,dR \quad (3.39)$$

Here, Equation (3.39) represents the multiexponential decay where $f(R)$ is the probability of obtaining a decay rate, R. $S(t)$ is the time domain signal such as acquired in an NMR relaxation experiment. The relaxation rate distribution is imbedded in $f(R)$, so an inverse Laplace transformation (ILT) is needed to extract the relaxation rate

distribution. The ILT is asymmetric, ill-defined, and difficult to implement, but an analytical expression does exist

$$f(R) = \mathcal{L}^{-1}\{S(t)\} = \frac{1}{2\pi i}\int_{\gamma-i\infty}^{\gamma+i\infty} S(t)\exp(Rt)\,dt \quad (3.40)$$

The integral in Equation (3.40) is a contour integral where γ is a vertical contour positioned to the right of any singularities, thus, the introduction of gamma prevents the integration of a singularity. However, the above expression is unstable due to the increasing exponential term which may lead to exponential divergence due to the presence of noise in $S(t)$, something that is unavoidable in NMR experiments. Instead, a regularized non-negative least squared method of the ILT that accounts for noise was suggested by Provencher in 1982 [7]

$$S(t_i) = \sum_{j=1}^{M} \exp\left(-t_i R_j\right) f\left(R_j\right) + \epsilon_i \quad (3.41)$$

where $i = 1 \ldots N$ representing discrete sampling time intervals, and $j = 1 \ldots M$ representing the numerous relaxation rate domains for which the solution $f(R)$ is being discretized. ϵ_i is the error due to noise in the measurement, so the results of a measurement can be optimized by minimizing ϵ_i. This method requires that the spectral amplitudes of $f(R_j)$ are all positive, and that the simplest solution, which contains the least amount of detail and information is being used. To ensure that the simplest solution is being used, Provencher implemented a method known as the Tikhonov regularization method in which the goal is to determine the minimum value of the solution, $V(\alpha)$, given by

$$V(\alpha) = \left\| \underline{\underline{K}} f - \underline{S} \right\|^2 + \alpha^2 \left\| \underline{\underline{\Gamma}} f \right\|^2 = minimum \quad (3.42)$$

where K is the kernel, α is the regularization parameter, Γ is an operator that promotes smoothness, S is the measured signal, and f is the least-squares solution and the distribution of relaxation rates. The last term in Equation (3.42) can be expressed as

$$\left\| \underline{\underline{\Gamma}} f \right\|^2 = \int_{R_{min}}^{R_{max}} [f''(R)]^2 dR \quad (3.43)$$

where R_{min} and R_{max} are the bounds of the solution variable R. The solution, $V(\alpha)$, can be discretized so that the solution vector, f, takes on values corresponding to each R_j, obtaining the expression

$$V(\alpha) = \sum_i^N \sum_j^M (S_i - \exp(-t_i R_j) f_j)^2 + \alpha^2 \sum_j^M (2f_j - f_{j+1} - f_{j-1})^2 = minimum \quad (3.44)$$

The last summation in Equation (3.44) is the residual denoted χ^2, and is calculated for each value of α^2. To obtain the minimum value of the solution, $V(\alpha)$, a value of α^2 that minimizes χ^2 is chosen. However, if the chosen value for α^2 is too high a phenomenon known as “pearling” will result, where the final relaxation rate distribution display more fine detail than actually exists in the data. Thus, α^2 is chosen with the aim to minimize χ^2, but only just.

The T_1-T_2 Correlation Pulse Sequence

The T_1-T_2 correlation experiment has the ability to probe both spin-lattice and spin-spin relaxation in just one NMR experiment by performing an inversion recovery in quick succession with a CPMG train. In the T_1-T_2 pulse sequence shown in Figure 3.4, τ_1 is the inversion, or evolution, time in the inversion recovery, and τ_2 is the time for any echo maxima in the CPMG sequence and is given by $\tau_2 = n\tau_E$, where τ_E is the echo time as usual. The sequence is executed by first performing the inversion recovery and CPMG train in succession before looping back to the beginning of the sequence again. The loop is performed *N* times for *N* different inversion times.

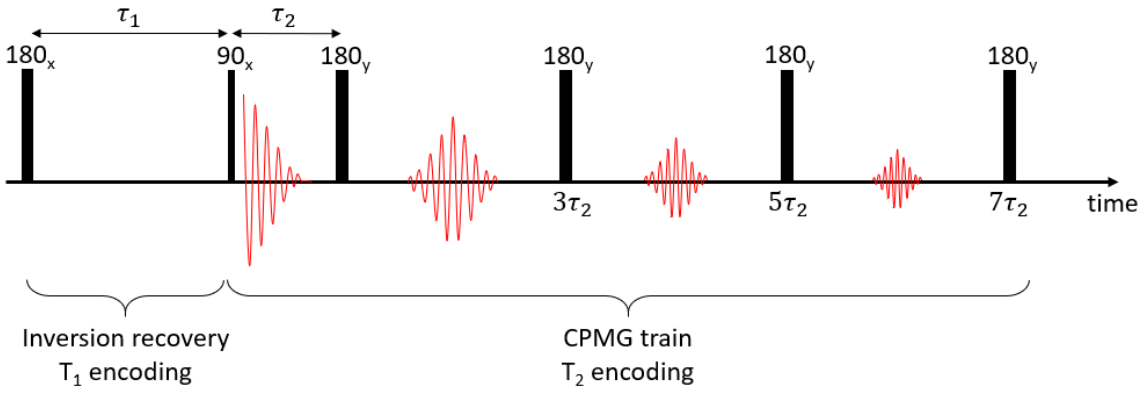

Figure 3.4. The T_1-T_2 pulse sequence consist of an inversion recovery which encodes for T_1 relaxation followed by a CPMG train which encodes for T_2 relaxation. The combination of the two pulse sequences allows for investigation of the correlation between T_1 and T_2 relaxation in a sample.

The normalized signal is given by

$$S(\tau_1, \tau_2) = \int\int (1 - 2\exp(-R_1\tau_1))\exp(-R_2\tau_2)\, f(R_1, R_2) dR_1 dR_2 \qquad (3.45)$$

where $f(R_1, R_2)$ is the relaxation spectrum density, and R_1 and R_2 are the T_1 and T_2 relaxation rates, respectively. To analyze the data using the ILT, the discrete form of the normalized signal is necessary. Using explicit discretization of two independent encoding times τ_1 and τ_2,

$$S(\tau_{1i}, \tau_{2j}) = \sum_{k=1}^{M_1} \sum_{l=1}^{M_2} (1 - 2\exp(-R_{1k}\tau_{1i}))\exp(-R_{2l}\tau_{2j})\, f(R_{1k}, R_{2l}) + \epsilon_{i,j} \quad (3.46)$$

The relaxation rate distribution imbedded in $f(R_{1k}, R_{2l})$ can then be obtained, and an example of such a distribution, known as a relaxation correlation map, is given in Figure. 3.5.

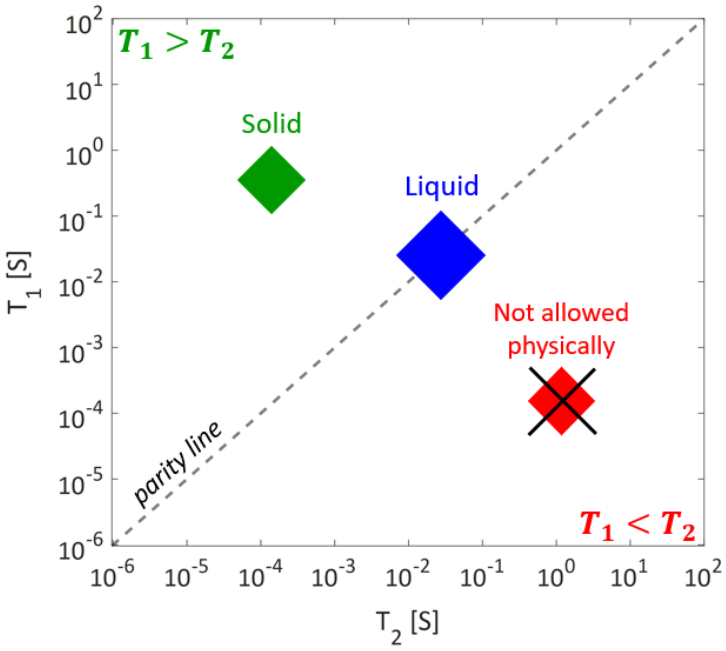

Figure 3.5. A hypothetical representation of a T_1-T_2 relaxation correlation map. Populations representing bulk liquids (blue) will appear on the parity line where $T_1 = T_2$. Populations representing highly viscous liquids or solids (green) will appear to the left of parity line, $T_1 > T_2$. No populations should appear to the right of the parity line because, in theory, T_1 should never be less than T_2.

The dashed line in the above plot, often referred to as the 'parity line', represent $T_1 = T_2$. Any relaxation population that appears on the parity line is characterized as a non-viscous bulk fluid. Populations that appear to the left of the parity line are defined as highly viscous fluids or solids for which $T_1 > T_2$. No populations should appear to the right of the parity line as this would indicate $T_1 < T_2$, which is known to be non-physical. However, relaxation populations will occasionally appear in this 'forbidden' region and are referred to as negative amplitude peaks because they are a result of negative amplitude relaxation eigenmodes. These populations are not a true representation of actual relaxation rates, but rather an artifact as a consequence of unnatural non-

exponential decaying behavior of the acquired signal, which can be observed in the raw time domain data.

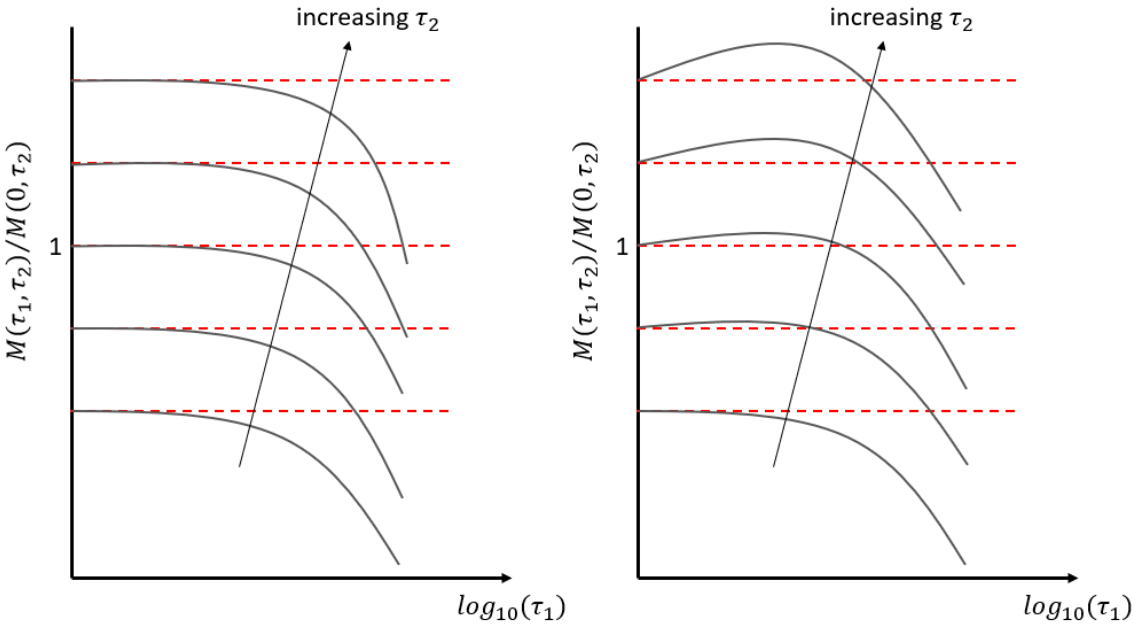

Figure 3.6. Two hypothetical cases of magnetization decay as a function of τ_1 at five different τ_2-times. Each data set is normalized by the initial magnetization amplitude, $M(0,\tau_2)$, and shifted away from unity for better visualization. The left plot demonstrates a typical exponential signal decay from a *T₁*-*T₂* correlation experiment. The initial rise in signal in the right plot is abnormal, but still occasionally observed, and is associated with complex diffusion dynamics.

The plots in Figure 3.6 show the normalized magnetization decay for a *T₁*-*T₂* experiment as a function of the inversion time, τ_1, at a specific τ_2 time. Normally, the magnetization will decay away exponentially due to relaxation effects as depicted in the left plot, but under certain conditions, an initial increase in the signal is observed for short τ_1-times. The increase becomes more predominant at longer τ_2-times and is caused by complex diffusion dynamics in which the relaxation modes in an interconnected

geometric structure are coupled through a specific combination of fast and slow molecular exchange. Because the ILT requires the spectral amplitudes of $f(R_{1k}, R_{2l})$ to be all positive, the presence of negative amplitude relaxation modes may distort the relaxation distribution spectrum, resulting in unreliable relaxation correlation maps.

References

1. Stejskal, E.O. and J.E. Tanner, *Spin Diffusion Measurements: Spin Echoes in the Presence of a Time-Dependent Field Gradient.* Journal of Chemical Physics, 1965. **42**(1): p. 288-+.

2. Stejskal, E.O., *Use of Spin Echoes in a Pulsed Magnetic-Field Gradient to Study Anisotropic Restricted Diffusion and Flow*. Journal of Chemical Physics, 1965. **43**(10P1): p. 3597-+.

3. Torrey, H.C., *Bloch Equations with Diffusion Terms.* Physical Review, 1956. **104**(3): p. 563-565.

4. Callaghan, P.T., *Translational Dynamics & Magnetic Resonance: Principles of Pulsed Gradient Spin Echo NMR*. 2011, New York: Oxford University Press.

5. Brownstein, K.R. and C.E. Tarr, *Importance of Classical Diffusion in NMR-Studies of Water in Biological Cells.* Physical Review A, 1979. **19**(6): p. 2446-2453.

6. Fick, A., *Uber Diffusion*. 1855, Phil. Mag.

7. Provencher, S.W., *A Constrained Regularization Method for Inverting Data Represented by Linear Algebraic or Integral-Equations.* Computer Physics Communications, 1982. **27**(3): p. 213-227.

NMR RELAXOMETRY TO CHARACTERIZE DRUG STRUCTURAL PHASE IN A POROUS CONSTRUCT

Contribution of Authors and Co-Authors

Manuscript in Chapter 4

Author: Linn W. Thrane

Contributions: Assisted in design and implementation of NMR experiments. Collected and analyzed all NMR data. Wrote manuscript.

Co-Author: Emily A. Berglund

Contributions: Assisted in design and implementation of study. Prepared samples for NMR experiments. Provided feedback and comments on manuscript.

Co-Author: James N. Wilking

Contributions: Assisted in design and implementation of study. Helped with data interpretation. Provided x-ray diffraction spectra. Provided feedback and comments on manuscript.

Co-Author: David Vodak

Contributions: Helped with data interpretation. Provided feedback and comments on manuscript.

Co-Author: Joseph D. Seymour

Contributions: Assisted in design and implementation of NMR experiments. Helped with data interpretation. Assisted in writing of manuscript. Provided feedback and comments on manuscript.

Manuscript Information Page

Linn W. Thrane, Emily A. Berglund, James N. Wilking, David Vodak, Joseph D. Seymour

Molecular Pharmaceutics

Status of Manuscript:
____ Prepared for submission to a peer-reviewed journal
____ Officially submitted to a peer-review journal
____ Accepted by a peer-reviewed journal
_X___ Published in a peer-reviewed journal

American Chemical Society
Vol. 15, No. 7, Pages 2614-2620, June 2018

NMR RELAXOMETRY TO CHARACTERIZE DRUG STRUCTURAL PHASE IN A POROUS CONSTRUCT

Abstract

Nuclear magnetic resonance (NMR) frequency spectra and T_2 relaxation time measurements, using a high-power radio frequency probe, are shown to characterize the presence of amorphous drug in a porous silica construct. The results indicate the ability of non-solid-state NMR methods to characterize crystalline and amorphous solid structural phases in drugs. 2D T_1-T_2 magnetic relaxation time correlation experiments are shown to monitor the impact of relative humidity (RH) on the drug in a porous silica tablet.

Introduction

Drug solubility depends on whether the drug is in the crystalline or amorphous solid state [1]. Methods such as spray drying [2] and pore entrapment [3-6] are well established approaches to impact molecular dynamics during solidification and control the drug structural phase. Nuclear magnetic resonance (NMR) methods have been applied to characterize the amorphous and crystal structures of pharmaceuticals using solid state (ssNMR) methods [7-10]. These ssNMR methods require sample spinning and typically grinding of the sample into a powder, and the incompatibility of the methods with the liquid state preclude observing transitions from the liquid melt to the solid-state during solidification. Liquid state NMR relaxometry is well established to characterize pore size

distributions in porous media [11, 12]. NMR relaxation times are sensitive to phase transitions from liquid to solid state [13, 14]. Somewhat analogous to the solidification processes studied here are NMR cryoporometry in porous media which relies on the Gibbs-Thomson effect and the presence of nanoscale unfrozen water layers at the boundary of the solid porous matrix and the ice crystals in the bulk pores to characterize porous systems [15, 16].

In this paper we describe the use of a purpose-built high-power radio frequency (rf) pulse probe to measure the solidification of the drug fenofibrate in bulk and within a porous matrix. The probe allows high power short duration rf pulses capable of acquiring signal from the solid-state drug without sample spinning. NMR spectra indicate amorphous domains after solidification in the porous matrix that are not present in the bulk solidification, assisting in verification and interpretation of the novel relaxation data presented. The impact of relative humidity on the structure of the solid-state drug in the porous matrix is shown to correlate with NMR relaxation behavior. The results quantify the impact of porous matrix restriction on the drug solidification and indicate the potential for quality control and process monitoring by NMR.

Theory

NMR frequency spectra and magnetic relaxation times are sensitive to the liquid or solid phase of the sample and the solid-state structural crystal or amorphous phase. Frequency spectra of liquids are Lorentzian due to the exponential form of the time dependent free induction decay (FID) voltage signal, while those of solids are Gaussian

[17, 18]. This is due to motional averaging of the dipolar coupling of the ^{1}H protons in liquids by rotational diffusion [17]. In solids the correlation time of the dipolar coupling is much longer and results in a Gaussian FID that decays away rapidly in time (~1-100 μs) generating a broad Gaussian linewidth in the frequency domain [18]. The spin-spin T_2 relaxation time depends on the proton dipolar coupling and is short (< 1 ms) for solids and longer (>100 ms) for liquids and determines the line shape and linewidth. The solid phase ordering in crystalline phases increases the dipolar coupling with corresponding fast in time Gaussian FID decays with shorter T_2 than in amorphous solids where disorder and slightly increased mobility generates longer T_2 and potentially short time Gaussian and longer time exponential FIDs [12, 19]. Spin-lattice T_1 relaxation in liquids is at the order of seconds and $T_1 \sim T_2$, while in solids T_1 is much longer than T_2 [12]. The solid phase T_1 is longer in more ordered crystalline states than in amorphous states.

Methods

The porous matrix used in these experiments is a porous tablet made from colloidal silica. Silica with a stable ordered mesoporous structure has been shown to be a promising controlled drug delivery system [3]. Charge-stabilized, amorphous colloidal silica (Nissan Chemical, MP-1040-H) suspended in water with an average particle diameter of d = 100 nm and low size polydispersity (<5%) was used for all experiments. The surface of the colloidal silica is negatively charged with a surface charge density between 8 nm^{-1} and 10 nm^{-1}, and free of residual organics as stated by the manufacturer. 300 μL colloidal silica is added to cylindrical molds and left to solidify for 24 hours. The

tablet dimensions are set by the dimensions of the mold used during the slipcasting process. Tablets are cylindrical in shape, with a diameter and height on the order of 0.5-1 cm. Silica particles are packed into a random structure, as revealed by small angle neutron scattering experiments. The characteristic pore size can be estimated by calculating the void created by three kissing spheres: $D = 0.15d$; with d estimated as $d \approx$ 15 nm. After 24 hours, the fenofibrate is heated to 10°C above its melting point of 81.1°C and the drug is loaded into the tablet by imbibing the drug in liquid form. The fenofibrate is absorbed into the tablet by capillary action. Once the imbibition process is complete, the mass fraction of the drug in the composite is 0.18 ± 0.01, as measured using thermogravimetric analysis. This corresponds to the silica colloid volume fraction of $\varphi =$ 0.71, based on the density of amorphous silica $\rho_{\text{silica}} = 2.196$ g/cm^3 and the density of fenofibrate, $\rho_{\text{fenofibrate}} = 1.18$ g/cm^3. Measurements indicate that the void space is filled completely by the drug during imbibition. Finally, the tablet is wiped down to remove any excess drug on the surface before it is placed in a 5mm NMR tube. The bulk drug sample is prepared by adding the powdered drug to a 5mm NMR tube and melting the drug in the tube. The sample is quickly placed in a Bruker 250 MHz superconducting magnet integrated to an Avance III spectrometer where frequency spectra and T_2 measurements are performed using a high power radio frequency (rf) probe with a 5 mm rf coil custom built by Bruker. Temperature is controlled at 20°C using the Bruker BTU system with N_2 gas flow. The T_2 measurements are executed using the standard Carr-Purcell-Meiboom-Gill (CPMG) pulse sequence with echo time τ_E =12 μs, 500-4000 echoes depending on the sample, acquisition sampling dwell time of 1 μs, and 7.5 μs rf

pulses at 100 W power. The signal was acquired using 4 averages of a 16 phase cycle acquisition. The rapid data acquisition in the short $2 \cdot \tau_E$ period preludes full acquisition of the echo, so the data is not encoded for spectral frequency shift. Experiments with τ_E varying from 12-400 μs indicate no T_2 dispersion effect due to potential spin locking of longer T_2 components with rotating frame spin-lattice relaxation times $T_{1\rho}$ of similar magnitude [10, 20]. The T_2 relaxation data is converted by inverse Laplace transformation to a distribution of relaxation populations [11, 19, 21].

To explore the impact of relative humidity on the solidified drug with time, tablets are stored in an environment with controlled relative humidity at T = 20°C. The 0% RH conditions are set by sealing the tablet in a container with an excess of dry desiccant (Drierite). 100% RH conditions are set by sealing the composites in a container with excess liquid water. Liquid water is not allowed to be in contact with the tablet, but creates a saturated vapor pressure at equilibrium in an enclosed environment. Measurements of a tablet kept in a 0% RH environment are compared to measurements of a tablet kept in a 100% RH environment for two weeks. T_1 and T_2 relaxation data are acquired by performing 1D T_2 experiments and 2D T_1-T_2 correlation experiments. The T_1-T_2 measurements are performed using an inversion recovery combined with a CPMG pulse sequence [11]. The same parameters used in the T_2 measurements are used for the CPMG portion of the T_1-T_2 measurement except that 2 averages of the 16 phase cycle acquisition are used. Inversion recovery is performed with inversion times logarithmically spaced from 1 ms to 50 s. Inverse Laplace transforms of the relaxation data are performed in 1D for T_2 and 2D for T_1-T_2 experiments to provide distributions of

relaxation times. Data was collected on day 1, 3, 7, and 14 of the storage in 100% RH. To avoid exposing the sample to lower relative humidity during measurements, four samples were prepared so that none of the tablets were removed from the high relative humidity environment until the measurement was performed.

Results and Discussion

Drug Solidification

Once the tablet or the bulk drug is placed in the magnet, frequency spectra and T_2 measurements are interleaved and performed continuously until the drug is fully solidified and no further changes are observed. The fenofibrate is originally in powder form of ground crystal but takes on a more ordered crystalline structure when it solidifies after being melted [22]. This is indicated by the T_2 measurements of the drug in powder form and after the melted drug has solidified.

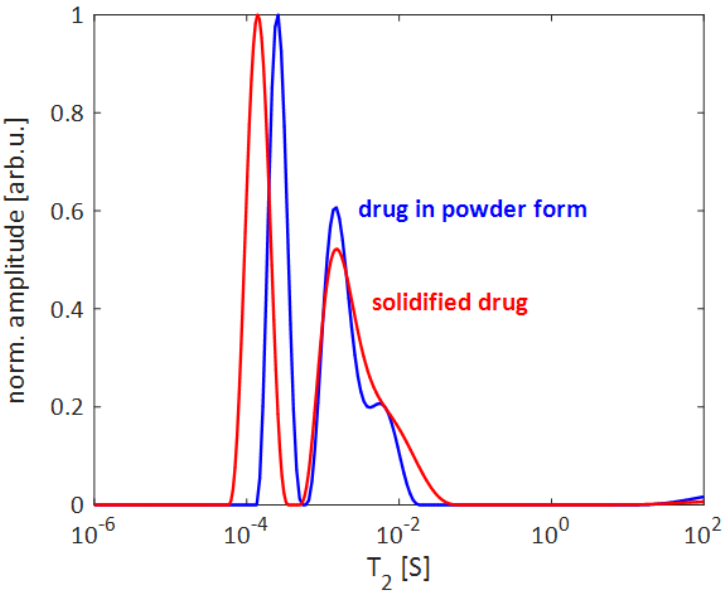

Figure 4.1. T_2 distributions of the drug in powder form (blue/black), and the solidified drug after being melted and recrystallized (red/grey). Two populations are observed in both samples, and the signal intensity ratio between the two populations remain approximately the same before and after melting. The population with shortest T_2 time experiences a shift towards shorter relaxation times when solidifying after being melted

The T_2 distributions in Figure 4.1 show that the drug has two T_2 populations before and after being melted, and the signal amplitude distribution between the two peaks remain approximately the same. A shift towards shorter T_2 relaxation times is observed in the melted and solidified drug. Additionally, the total signal amplitude of the solidified drug is two orders of magnitude lower than that of the powdered drug, however, this cannot be seen in Figure 4.1 due to both of the T_2 distributions being normalized by the population amplitude maximum for visualization of the shift in T_2 relaxation time. The decrease in total measured signal amplitude in the recrystallized system is due to the T_2 relaxation times of the drug becoming too short, *i.e.* less than τ_E of 12 μs, for the NMR pulse sequence to detect, indicating a more ordered crystalline

structure than the powder form. The two populations thus represent the most rotationally mobile protons in the system with T_2 > ~50 µs. The populations cannot be assigned to specific moieties on the molecule. However, from spectroscopic experiments and quantum mechanical simulations, the crystal structure indicates stacking of benzene rings [22]. The population at $T_2 \sim 10^{-4}$ s shifts to lower T_2 values in the melted solidified sample relative to the powdered form. It is expected the melt process will allow reorientation of molecules for a smaller molecular spacing in the crystal and protons in this population indicate that effect. The more rotationally mobile protons at $T_2 \sim 1\times10^{-3}$ are associated with the methyl groups furthest from the stacked benzene rings and the broad distribution of T_2's indicate they experience varying rotational mobility depending on the exact location on the molecule consistent with the model of Heinz et. al [22].

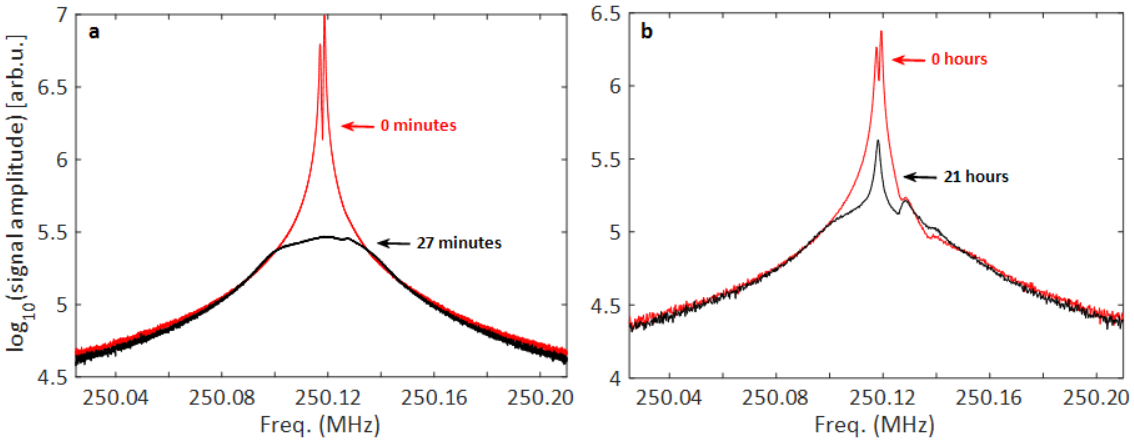

Figure 4.2. Frequency spectra of drug solidifying in (a) bulk and (b) tablet. In both samples, the drug starts out (red/grey) as highly amorphous indicated by the Lorentzian shape of the frequency spectra. Once the solidification process is complete, the pure drug has solidified (black) to a highly ordered crystalline structure, resulting in a broad Gaussian frequency peak. The final frequency spectrum for drug in the tablet is a combination of a broad Gaussian distribution and a Lorentzian, indicating that the drug solidifying in the restricted environment of the porous matrix is more amorphous than the bulk sample.

The bulk drug took approximately 30 minutes to fully solidify after melting, while it was 3-4 hours for the drug in the porous tablet to solidify. To ensure no further changes occurred in the tablet past the first 4 hours, the sample was stored and additional measurements were performed after 21 hours. Figure 4.2(a) shows frequency spectra of the drug in bulk in liquid melt state at 0 and in solid state at 27 minutes. The melt state signal is a convolution of a Gaussian and Lorentzian decay. This indicates the high degree of molecular order, likely due to pi stacking of the Benzene rings in the molten state. The Lorentzian portion of the frequency spectrum at 0 minutes is liquid like where the molecular mobility, *i.e.* the random modulation of the dipolar coupling, is fast. In bulk, the drug solidifies with unrestricted molecular mobility and the final result is a highly ordered crystalline structure. The slow random modulation of the dipolar coupling produces a pure Gaussian line shape in the frequency spectrum as can be seen in Figure 4.2(a) at 27 minutes [18].

A similar Lorentzian distribution is observed in the frequency spectra for the drug in a porous tablet in the liquid melt state at 0 minutes, Figure 4.2(b). However, in addition to the broad Gaussian distribution seen in the pure drug, a remaining Lorentzian distribution can be seen at 21 hours for this sample. The combination of Gaussian and Lorentzian line shapes in the frequency spectrum suggest that when restricted in a porous media, some of the drug will not reach the highly ordered crystalline structure of the pure drug. The Gaussian line shape confirms that the drug has solidified, but the remaining Lorentzian line shape indicates the presence of a highly amorphous state of solidified drug or supercooled liquid [23, 24].

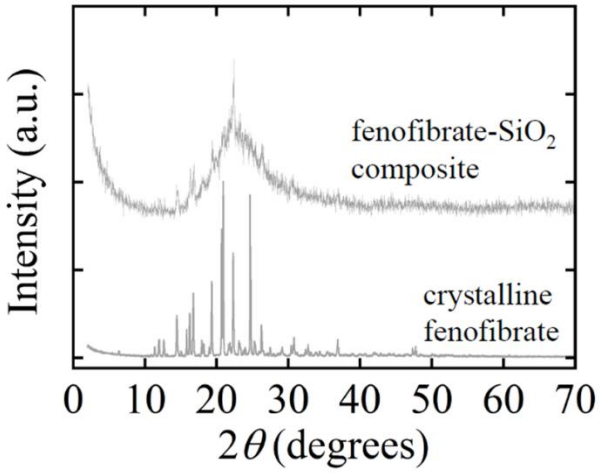

Figure 4.3. Wide angle x-ray diffraction (WAXS) spectra for the fenofibrate-SiO_2 composite with unprocessed crystalline fenofibrate powder direct from the manufacturer. The primary Bragg peaks in the composite scattering do not match up with those in the crystalline active, indicating they do not have the same crystal structure. A broad amorphous SiO_2 peak dominates the composite sample signal.

When the bulk drug solidifies, a highly ordered bulk crystal structure forms. In a confined environment of 15 nm pores, as used here, fenofibrate has been shown to produce nanocrystals by ^{13}C MAS ssNMR and XRPD [25]. In that study ssNMR data showed line broadening with pre size decreasing from 300 nm to 20 nm that was attributed to surface disorder as nanocrystals became small, thus differentiating surface drug versus nanocrystalline core drug [25]. At 12 nm pore size the ssNMR still indicated crystalline drug, but the ^{13}C spectra broadening and XRPD data indicated loss of long-range order. Wide angle x-ray diffraction on the bulk fenofibrate and fenofibrate in the porous construct for our samples how similar behavior to the XPRD data of reference [25] with crystalline behavior in bulk and a large background silica signal in the small pore tablet (Figure 4.3). The linewidth of the Gaussian portion of the spectra for the bulk and tablet solidified samples (Figure 4.2) have similar linewidth, indicating the presence

of nanocrystals of drug in the pore. The Lorentzian component indicates an amorphous component due to the impact of the silica fenofibrate surface interactions. This could be due to supercooled liquid or amorphous surface solid. Given the rapid crystallization behavior of supercooled fenofibrate, which occurs on the timescale of minutes in the presence of a nucleation site [23, 24], we believe it is surface impacted solid [25].

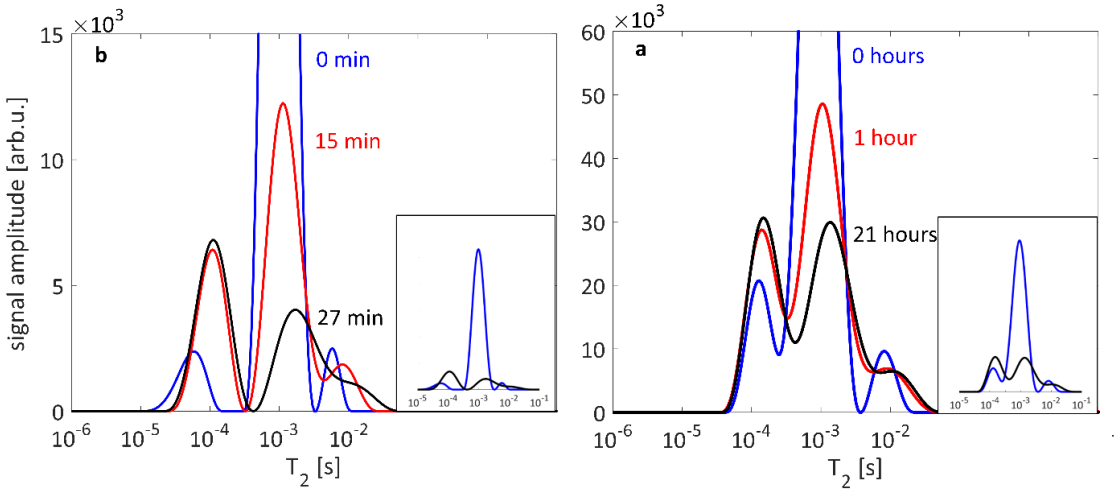

Figure 4.4. T_2 distributions of drug solidifying in (a) bulk and (b) tablet. The full signal amplitude is shown in the right corner of the plots. There is a large signal loss in both samples due to the solidification of the drug. Once solidification is complete in the bulk sample, most of the signal from the longer T_2 population, ~10^{-3} s, is lost and most of the signal results from the shorter T_2 population, ~10^{-4} s. In the tablet sample, there is an equal signal distribution between the ~10^{-3} s and the ~10^{-4} s T_2 populations when the solidification is complete, confirming the results seen in the frequency spectra suggesting that the drug in the tablet is in a more amorphous mobile state than the highly ordered bulk sample.

The T_2 data collected during the solidification process, Figure 4.4, indicate that a majority of the signal originates from the population with T_2 relaxation times of ~10^{-3} s, 9.9×10^{-4} seconds in the bulk fenofibrate and 9.3×10^{-4} s in the tablet, when the drug is in liquid form. Note that the most rotationally mobile protons in the melt at T_2 ~10^{-2} s are no

longer fully resolved in the solidifying sample. These most mobile protons associated with the methyl protons become a shoulder on the T_2 ~10^{-3} s population as the crystal forms. In both systems, the signal amplitude of the ~10^{-3} s T_2 time population decreases significantly and the signal amplitude of the shorter T_2 time population, ~10^{-4} s, increases during the drug solidification. These results indicate that the relaxation time of a portion of the fenofibrate shifts from the decreasing long T_2 population to the short T_2 population, and the remaining drug exhibits T_2 times too short to detect with the 12 μs τ_E. In the bulk fenofibrate (Figure 4.4(a)), the signal amplitude of the ~10^{-3} s T_2 population keeps decreasing until a greater portion of the remaining signal originates from the ~10^{-4} s T_2 population. For the fenofibrate in the tablet (Figure 4.4(b)), the signal amplitude of the ~10^{-3} s T_2 population stops decreasing when the remaining signal is evenly distributed between the two populations. The even distribution of signal amplitude in the final state of fenofibrate in the porous medium compared to that of the bulk fenofibrate confirms the results from the frequency spectra that the drug takes on a more amorphous structure when solidifying within a restricted environment [25].

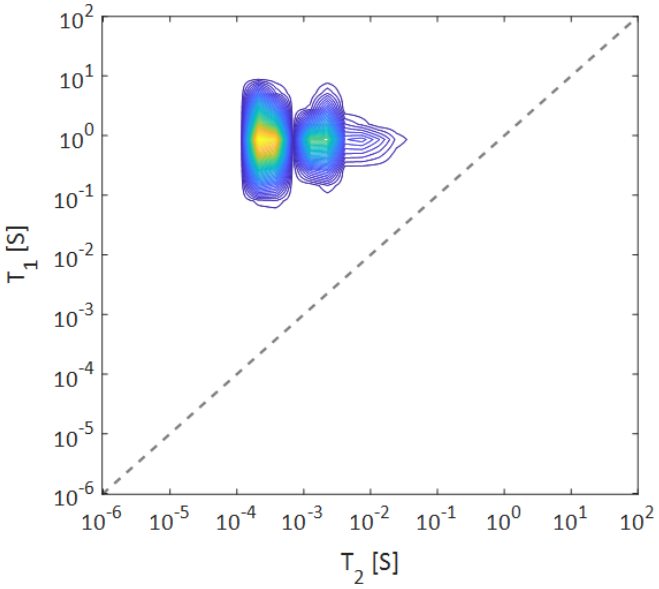

Figure 4.5. T_1-T_2 correlation data from the model drug in a tablet kept at 0% RH. The T_1-T_2 data indicate that there are two populations with different T_2 relaxation times present in the tablet at 0% RH. The two populations have identical T_1 relaxation times and T_2 times on the order of 10^{-4} s and 10^{-3} s.

Impact of Relative Humidity

The impact of relative humidity on the structure of a solid-state drug is of relevance to long time storage of the drug. If stored in a high relative humidity environment over time, water will begin to inhabit the pore space of the tablet due to capillary condensation. T_1-T_2 correlation measurements are used to quantify the effect of 100% relative humidity on fenofibrate confined in a porous matrix over a 2 week period. For comparison, T_1-T_2 data was collected from fenofibrate in a tablet stored at 0% relative humidity. At 0% relative humidity, the T_1-T_2 correlation data, Figure 4.5, reveals two main populations with identical T_1 relaxation times and T_2 times at the order of 10^{-4} and 10^{-3} s, and the broad shoulder out to 10^{-2} s on the 10^{-3} s population. These are similar

T_2 times to those observed in the T_2 distributions in Figure 4.1 and 4.4. The tablet stored at 0% RH showed no significant changes over time.

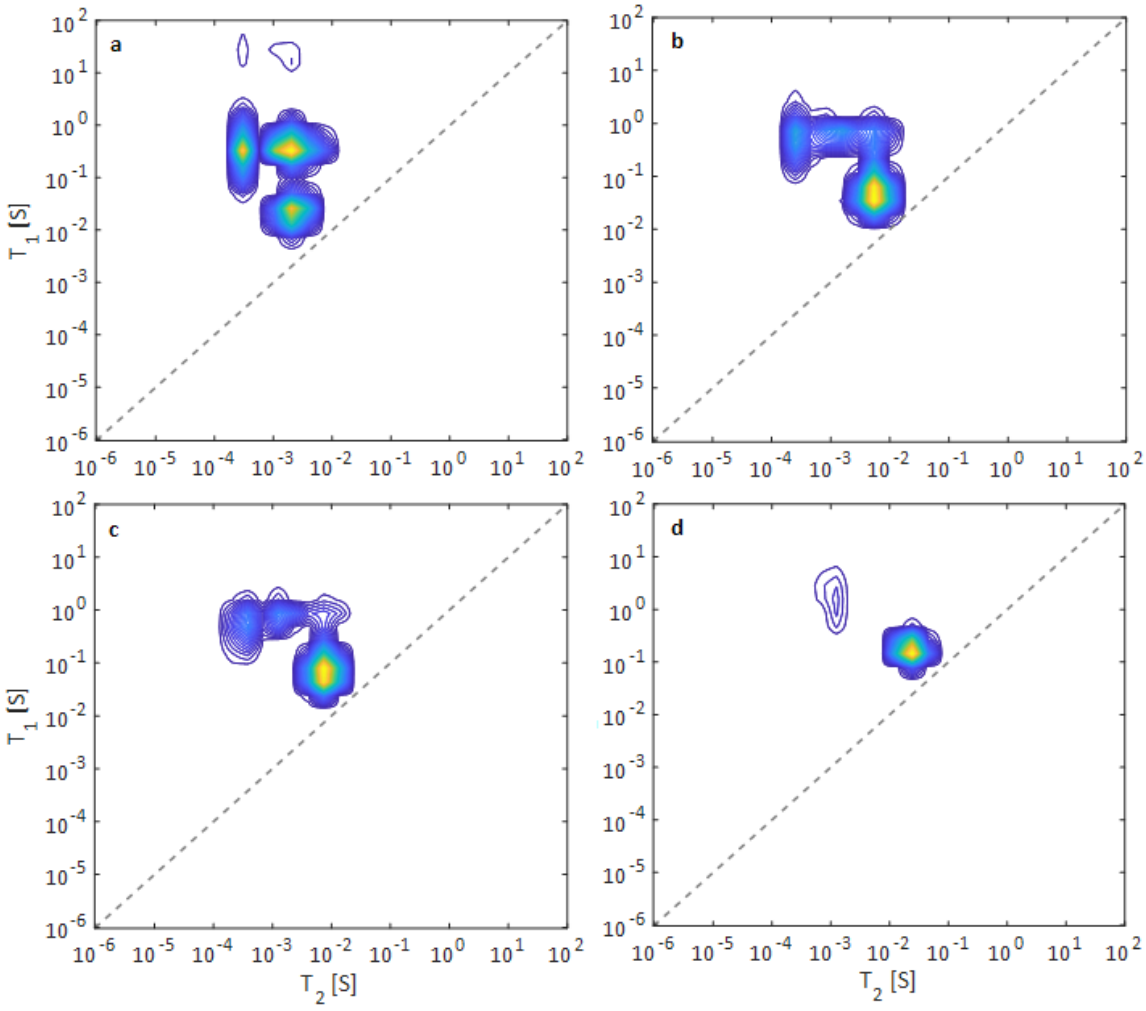

Figure 4.6. T_1-T_2 correlation data of drug in tablet stored at 100% RH for (a) 1 day, (b) 3 days, (c) 7 days, and (d) 14 days. It can be seen already on day 1 that a third population has appeared closer to the T_1=T_2 parity line (grey dashed line) when comparing to the T_1-T_2 data at 0% RH. This population is in liquid form and is attributed to water building up in the porous matrix of the tablet. The peak representing water is increasing in amplitude with time and is approximately one order of magnitude greater by day 14. The two populations representing the drug trapped within the pore space of the tablet is decreasing in amplitude with time.

T_1-T_2 measurements from day one of a tablet stored at 100% relative humidity reveal a third population in the T_1-T_2 correlation map closer to the parity line (grey dashed line), Figure 4.6(a), representing T_1 equal to T_2. Populations located on or close to the parity line are representative of a liquid phase, and it can therefore be assumed that this third population is water that has entered the porous matrix of the tablet as a result of its high relative humidity environment. The signal amplitude of the population representing water increases with time and is approximately one order of magnitude greater by day 14. The water population is also shifting towards longer T_1 and T_2 relaxation times, with T_1 increasing from 10^{-2} s on day 1 to 10^{-1} s by day 14, and T_2 increasing from 10^{-3} s to 10^{-2} s by day 14. The increase in relaxation time along with the increase in signal amplitude of the water population indicate that the water is progressively occupying more of the pore space as well as larger pores in the porous matrix over the 14-day period. The two populations representing the drug in the tablet decrease in amplitude over the 14-day period, but do not experience a significant shift in T_1 or T_2 relaxation time.

This is more readily observed in Figure 4.7 where the 1D T_2 distributions from day 1, 3, 7, and 14 are presented. The T_2 distributions are normalized to the maximum population amplitude recorded on day 14 so that the growth of the water peak can be visualized. The population with highest signal amplitude in the T_2 distribution for day 1, Figure 4.7(a), represent signal originating from both the highly restricted mobility water population and the drug population with 10^{-3} s T_2 from Figure 4.6(a). On day 1, these two populations exhibit similar T_2 times and can therefore not be distinguished in the T_2

distribution. On day 3, the water population has experienced a large enough increase in T_2 times to appear as a third peak with T_2 of 5.6×10^{-3} s in Figure 4.7(b). This very short T_2 time indicates water in highly restricted thin films. The water peak keeps increasing in signal amplitude and shifting towards longer T_2 times until a T_2 of 2.3×10^{-2} s is reached on day 14 (Figure 4.7(d)). This T_2 time indicates highly restricted water relative to bulk, but the near order of magnitude increase from day 3 suggests significant changes in restriction length scale. The two populations representing the drug have experienced a slight decrease in signal amplitude by day 14, but no significant shift in T_2 times, indicating drug insolubility. Since the drug appears insoluble and the water occupies larger length scale environments, the pore structure must be altered by the water through tablet volume expansion or breakup. This effect is also observed visually.

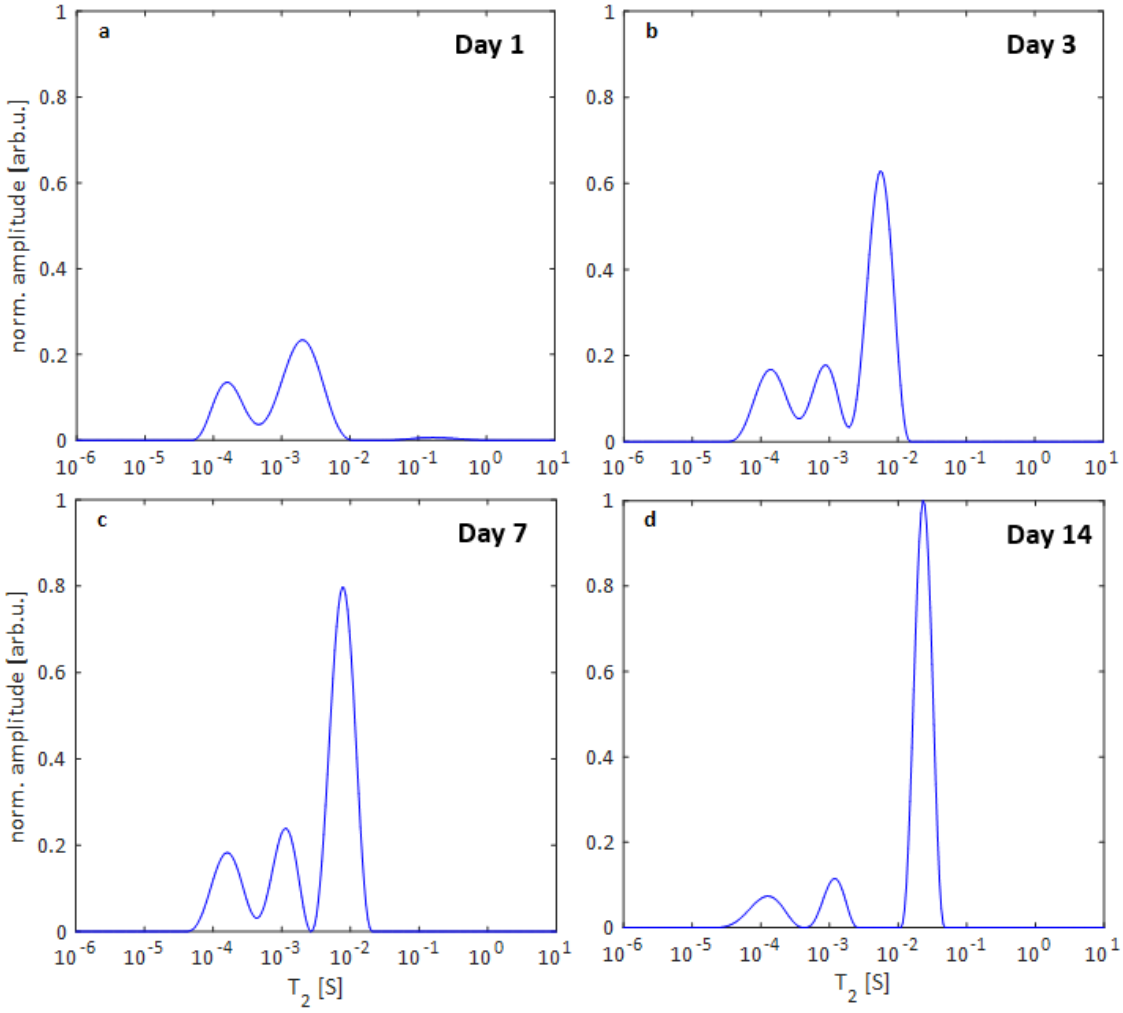

Figure 4.7. T_2 distributions of the drug in tablet stored at 100% RH for (a) 1 day, (b) 3 days, (c) 7 days, and (d) 14 days. On day 1 (a), the water population and the drug population with longest T_2 time, ~10^{-3} s, overlap and appear as just one population. By day 3 (b), the relaxation time of the water population has increased, and the water population appears as the third peak with the longest T_2 time at 5.6×10^{-3} s in the T_2 distribution. The water peak continues to shift towards longer relaxation times, 7.7×10^{-3} s on day 7 and 2.3×10^{-2} s on day 14, as well as increasing in signal amplitude.

Conclusion

NMR frequency spectra and 1D T_2 measurements were used to characterize the solidification of fenofibrate in bulk and in a porous matrix. The results indicate that fenofibrate takes on an amorphous structure in a confined environment of ~15 nm compared to the highly ordered crystal structure formed by the bulk drug and confirms the application of nonsolid-state NMR to distinguish and characterize crystalline- and amorphous solid structural phases in drugs. 1D T_2 and 2D T_1-T_2 relaxation correlation experiments were used to investigate the impact of relative humidity on fenofibrate in a porous silica tablet. Over a 14-day period, water was observed occupying progressively more of the porous silica matrix, decreasing the total drug signal detected and occupying an increasing size pore space. The results indicate the potential for drug quality control by NMR relaxometry. The further development of low field NMR systems opens the way towards online observation during storage as well as during dissolution studies under varying conditions.

Acknowledgements

JDS acknowledges Bend, Lonza, for research funding, U.S. NSF MRI program and Murdock Charitable Trust for equipment funding, and Dieter Gross at Bruker BioSpin for construction of the high power probe. JNW acknowledges the NSF (DMR-1455247) for research funding. The authors thank S.L. Codd for assistance.

References

1. Murdande, S.B., et al., *Solubility Advantage of Amorphous Pharmaceuticals: I. A Thermodynamic Analysis.* Journal of Pharmaceutical Sciences, 2010. **99**(3): p. 1254-1264.

2. Friesen, D.T., et al., *Hydroxypropyl Methylcellulose Acetate Succinate-Based Spray-Dried Dispersions: An Overview.* Molecular Pharmaceutics, 2008. **5**(6): p. 1003-1019.

3. Wang, S.B., *Ordered mesoporous materials for drug delivery.* Microporous and Mesoporous Materials, 2009. **117**(1-2): p. 1-9.

4. Vallet-Regi, M., et al., *A new property of MCM-41: Drug delivery system.* Chemistry of Materials, 2001. **13**(2): p. 308-311.

5. Xu, Z.P., et al., *Inorganic nanoparticles as carriers for efficient cellular delivery.* Chemical Engineering Science, 2006. **61**(3): p. 1027-1040.

6. Vallet-Regi, M., *Ordered mesoporous materials in the context of drug delivery systems and bone tissue engineering.* Chemistry-a European Journal, 2006. **12**(23): p. 5934-5943.

7. Skotnicki, M., et al., *Characterization of Two Distinct Amorphous Forms of Valsartan by Solid-State NMR.* Molecular Pharmaceutics, 2016. **13**(1): p. 211-222.

8. Pham, T.N., et al., *Analysis of Amorphous Solid Dispersions Using 2D Solid-State NMR and H-1 T-1 Relaxation Measurements.* Molecular Pharmaceutics, 2010. **7**(5): p. 1667-1691.

9. Dempah, K.E., J.W. Lubach, and E.J. Munson, *Characterization of the Particle Size and Polydispersity of Dicumarol Using Solid-State NMR Spectroscopy.* Molecular Pharmaceutics, 2017. **14**(3): p. 856-865.

10. Yuan, X.D., D. Sperger, and E.J. Munson, *Investigating Miscibility and Molecular Mobility of Nifedipine-PVP Amorphous Solid Dispersions Using Solid-State NMR Spectroscopy.* Molecular Pharmaceutics, 2014. **11**(1): p. 329-337.

11. Callaghan, P.T., *Translational Dynamics & Magnetic Resonance: Principles of Pulsed Gradient Spin Echo NMR*. 2011, New York: Oxford University Press.

12. Blümich, B., *NMR Imaging of Materials*. 2000, Oxford: Clarendon Press.

13. Buda, A., et al., *Molecular dynamic heterogeneity of confined lipid films by H-1 magnetization-exchange nuclear magnetic resonance.* Journal of Chemical Physics, 2005. **122**(3): p. 8.

14. Fujara, F., et al., *Translational and Rotational Diffusion in Supercooled Orthoterphenyl Close to the Glass-Transition.* Zeitschrift Fur Physik B-Condensed Matter, 1992. **88**(2): p. 195-204.

15. Mitchell, J., J.B.W. Webber, and J.H. Strange, *Nuclear magnetic resonance cryoporometry.* Physics Reports-Review Section of Physics Letters, 2008. **461**(1): p. 1-36.

16. Petrov, O.V. and I. Furo, *NMR cryoporometry: Principles, applications and potential.* Progress in Nuclear Magnetic Resonance Spectroscopy, 2009. **54**(2): p. 97-122.

17. Abragam, A., *Principles of Nuclear Magnetism* 1983: Oxford University Press, USA.

18. Kubo, R., *A Stochastic Theory of Line Shape and Relaxation* in *Fluctuation, Relaxation, and Resonance in Magnetic Systems* D. Ter Haar, Editor. 1962, Oliver and Boyd Ltd: Edinburgh. p. 23-68.

19. Washburn, K.E., et al., *Simultaneous Gaussian and exponential inversion for improved analysis of shales by NMR relaxometry.* Journal of Magnetic Resonance, 2015. **250**: p. 7-16.

20. Santyr, G.E., R.M. Henkelman, and M.J. Bronskill, *Variation in Measured Transverse Relaxation in Tissue Resulting from Spin Locking with the CPMG Sequence.* Journal of Magnetic Resonance, 1988. **79**(1): p. 28-44.

21. Song, Y.Q., et al., *T-1-T-2 correlation spectra obtained using a fast two-dimensional Laplace inversion.* Journal of Magnetic Resonance, 2002. **154**(2): p. 261-268.

22. Heinz, A., et al., *Understanding the solid-state forms of fenofibrate - A spectroscopic and computational study.* European Journal of Pharmaceutics and Biopharmaceutics, 2009. **71**(1): p. 100-108.

23. Amstad, E., F. Spaepen, and D.A. Weitz, *Crystallization of undercooled liquid fenofibrate.* Physical Chemistry Chemical Physics, 2015. **17**(44): p. 30158-30161.

24. Szklarz, G., et al., *Crystallization of supercooled fenofibrate studied at ambient and elevated pressures.* Physical Chemistry Chemical Physics, 2017. **19**(15): p. 9879-9888.

25. Dwyer, L.M., et al., *Confined crystallization of fenofibrate in nanoporous silica.* Crystengcomm, 2015. **17**(41): p. 7922-7929.

PROBING MOLECULAR DYNAMICS DURING HYDRATE FORMATION BY HIGH FIELD NMR RELAXOMETRY AND DIFFUSOMETRY

Contribution of Authors and Co-Authors

Manuscript in Chapter 5

Author: Linn W. Thrane

Contributions: Assisted in design of experimental configuration. Prepared samples for NMR experiments. Collected and analyzed NMR data. Wrote manuscript.

Co-Author: Sarah L. Codd

Contributions: Assisted in design of experimental configuration. Helped with data interpretation. Provided feedback and comments on manuscript.

Co-Author: Joseph D. Seymour

Contributions: Assisted in design of experimental configuration. Helped with data interpretation. Provided feedback and comments on manuscript.

Manuscript Information Page

Linn W. Thrane, Sarah L. Codd, Joseph D. Seymour

Journal of Magnetic Resonance

Status of Manuscript:
_X_ Prepared for submission to a peer-reviewed journal
____ Officially submitted to a peer-review journal
____ Accepted by a peer-reviewed journal
____ Published in a peer-reviewed journal

Elsevier, Inc.

PROBING MOLECULAR DYNAMICS DURING HYDRATE FORMATION BY HIGH FIELD NMR RELAXOMETRY AND DIFFUSOMETRY

Abstract

High-field nuclear magnetic resonance (NMR) relaxometry and diffusometry along with magnetic resonance imaging were used to monitor phase transition molecular dynamics during hydrate formation occurring in water droplets dispersed in liquid cyclopentane. 1D T_2 relaxation measurements indicate the extent of hydrate formation as well as a reduction in water droplet size with progression of hydrate growth. MRI intensity and T_2 relaxation maps indicate spatially dependent hydrate formation rates due to the heterogeneity of the system. Spectrally resolved diffusion measurements indicate a reduction in the porosity of the hydrate agglomerate as the hydrate shell increases in thickness. A novel signal rise observed in two dimensional T_1-T_2 relaxation correlation experiments indicates complex diffusion dynamics due to coupling between regions with varying relaxation and diffusion. These results indicate the ability to monitor hydrate growth and phase transition molecular dynamics due to evolution of the porous hydrate agglomerate by means of high-field NMR.

Introduction

Clathrate hydrates are ice-like crystalline compounds in which hydrocarbon is contained within a cage of hydrogen bonded water molecules [1]. Hydrates typically form at low temperatures and high pressures, and are of particular interest to the oil- and

gas industry due to their potential as a natural gas storage, transportation, and recovery source, and their applications in CO_2 sequestration and separation [2]. However, they are also of major concern to the industry as hydrates tend to agglomerate in oil and natural gas pipelines and have the potential to clog pipelines causing damage [1, 3, 4]. Hydrates nucleate and grow at the interface of water droplets dispersed in the organic phase where hydrogen bonded water cages combine into larger structures. The two hydrate structures most commonly found are the cubic structure I and II [1]. Structure I hydrates host smaller guest molecules such as methane and carbon dioxide and are most commonly found in natural environments, while structure II hydrates have the capacity to host larger guest molecules and occur mostly in artificial environments such as gas pipelines [5]. In addition, a third, structure H hydrates have been identified [6]. A more detailed understanding of the kinetics of the phase transition involved in the nucleation, growth and decomposition process of hydrates is needed to further develop and improve technologies required to exploit the potential of natural gas hydrates [7, 8], and to reduce the risk of hydrate blockage in pipelines. One of the main obstacles of investigating the phase transitions involved in hydrate formation is the short time and length scales at which the transitions occur and the opaque nature of the material. Nuclear magnetic resonance (NMR) allows for non-invasive studies of complex opaque structures at microscopic length and timescales and has been used extensively in research on hydrates [6, 9-12]. High field studies have focused on spectroscopy [13-15] using ^{13}C, ^{2}H, ^{129}Xe, and solid-state NMR methods [16]. Other high field applications have used magnetic resonance imaging (MRI) to monitor water-methane hydrate formation rates in porous

systems [17, 18] and for individual water droplets[19]. NMR relaxation is highly sensitive to the thermodynamic phase of the system (liquid-solid-gas) as well as restrictions in motion that occur in porous systems and is therefore an ideal tool for investigating hydrate formation processes.

MRI has been used to monitor the formation of hydrates as the phase transition from liquid water dispersed in the organic phase to crystalline hydrate clusters that occur in bulk or in porous systems generates signal loss [10, 17-23]. Haber et al. [11] used low-field NMR relaxometry to measure water consumption and pulsed field gradient (PFG) NMR techniques to monitor the diameter of the water core within a hydrate shell during model cyclopentane hydrate formation. Kleinberg et al. [12] measured T_2 relaxation distributions using a 2.2 MHz logging tool on the sea floor and Gao et al. [24] obtained ^{2}H relaxation distributions in the lab at 2 MHz. However, to our knowledge, no high-field NMR studies of ^{1}H relaxation and diffusion have been reported.

Model cyclopentane hydrates were used in this work to explore the use of high-field NMR relaxometry and diffusometry to characterize molecular dynamics and aggregation structure evolution during the hydrate phase transition. T_2 relaxation MRI was used to provide information on spatial heterogeneity. One dimensional relaxation experiments along with two dimensional T_1-T_2 relaxation correlation experiments and spectrally resloved diffusion measurements were used to observe and characterize the transition from mobile to restricted dynamics simultaneously for both water and cyclopentane throughout the formation process.

Background

In order to clearly to demonstrate the ability of the NMR measurements to characterize the phase transition dynamics, a model of hydrate formation is considered. In this work, cyclopentane is the organic phase. Cyclopentane hydrates form structure II cages at atmospheric pressure and have a hydrate-forming equilibrium temperature of 7.7 °C [25]. This means hydrates will form at any temperature above the melting temperature of the ice and 7.7 °C, at which point the hydrates will dissociate. Structure II hydrates consist of 16 small 5^{12} cages with the shape of a pentagonal dodecahedron, and 8 hexakaidecahedral shaped larger $5^{12}6^4$ cages [5].

When the hydrate formation temperature is reached, initial hydrate nucleation occurs at the water-cyclopentane interface. Initial hydrate nucleation is a stochastic process often followed by an induction time, which is the time between hydrate nucleation and when the system reaches temperature and pressure conditions that support stable hydrates [26-28]. At this point, the growth of hydrate clusters begins [8]. Early hydrate growth is a rapid process that results in a thin hydrate shell with a highly dendritic structure encapsulating the water droplets and creating a barrier between the water and the organic phase [11, 29, 30]. Haber at al. observed an increase in hydrate shell thickness and, and decrease in water core diameter as the hydrate growth progressed [11]. Rao et al. [29] observed a highly porous shell early on in the hydrate growth phase with a porosity of $\varphi \sim 95\%$, consequently the thin hydrate shell does not pose a significant barrier to mass transport [31, 32]. In the first 25 h after the onset of hydrate growth, the porosity of the hydrate shell gradually decreases to below 50% and remains

almost constant for a period of time [29]. Towards the end of the hydrate growth (the last ~20 h) the shell gets thicker and becomes less porous as the dendritic structure fills in [11] with a final porosity of $\varphi \sim 5\%$ [29]. A model of the progression of the hydrate shell growth is shown in Figure 5.1. The NMR data is shown to measure dynamics consistent with such a model.

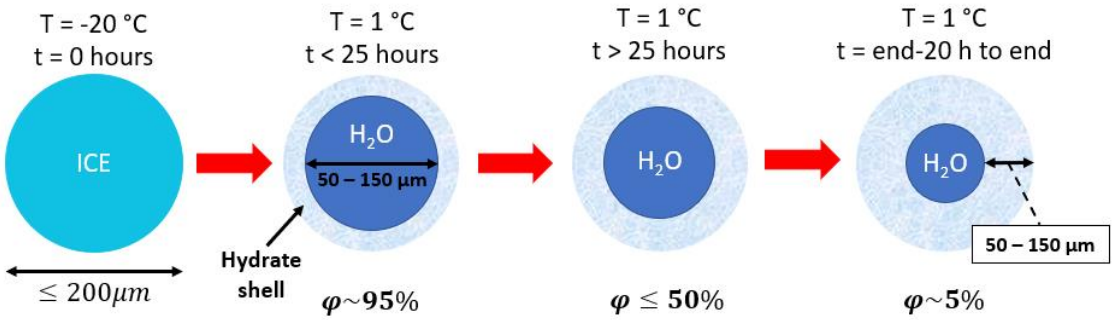

Figure 5.1. Once the hydrate nucleation temperature is reached (1 °C in this model), a thin, highly porous hydrate shell will encapsulate the water droplet. Over the first 25 hours, the thickness of the shell will increase and gradually fill in, resulting in a decreasing porosity. After the first 25 hours, the porosity of the shell stabilizes for a period before it continues to decrease while also continuing to increase in thickness. By the end of the hydrate growth, the porosity has decreased to ~5%. This model is based on the interpretation of work by Haber et al. [11] and Rao et al. [29].

Another aspect of hydrate formation the NMR data informs is the impact of hydrate inhibitors. Hydrate nucleation and growth can be disrupted by hydrate inhibitors which are used by the oil and gas industry to prevent hydrate plugging in pipelines. The most common types of hydrate inhibitors used today are known as low-dosage hydrate inhibitors (LDHIs) [33]. Two different types of LDHIs were added to the aqueous phase in some of the studies performed in this work to investigate changes in molecular dynamics during hydrate formation evident in the NMR data due to the presence of a hydrate inhibitor. The two types of LDHIs are known as kinetic hydrate inhibitors (KHIs)

and anti-agglomerants (AAs) [33]. KHIs act to prevent nucleation and are generally water-soluble polymers with functional groups that can be accommodated into the hydrate cages, thus also resulting in an increased induction time and severely delaying the onset of hydrate growth [33, 34]. However, when hydrate formation begins, hydrate clusters will form in the same fashion as in the absence of a LDHI. The AAs generally consist of molecules with a hydrophilic head group and hydrophobic tails and tend to accumulate at the hydrocarbon-water interface where initial hydrate formation occurs. The hydrate-philic head groups will attach to the surface of the hydrate crystals, while the hydrophobic tails repel the aqueous phase, preventing the formation of new hydrate crystals on that surface [33]. Consequently, the hydrate crystals do not agglomerate and remain small and exist as particles dispersed in the liquid hydrocarbon and aqueous phase.

Methods

Cyclopentane hydrates were prepared by crushing distilled water ice in a blender. The ice particles were then sieved to diameters ≤ 250μm at -20°C (Montana State University Subzero Research Facility) as thawing ice particles contribute to more rapid hydrate nucleation and growth [11, 35]. Precooled cyclopentane was added in excess to the ice particles using a micro pipette and the mixture was stored in 5mm NMR test tubes in a Fisher Scientific cooling bath kept at -20°C. The sample was then transferred to the precooled magnet, also kept at -20°C. The temperature within the magnet was gradually increased at a rate of 1°C/180 s until the desired melt and nucleation temperature, 1°C for

the data shown here, was reached. This temperature is above the melting temperature of the ice, but below the equilibrium temperature of 7.7°C for cyclopentane hydrates [25]. Once the desired formation temperature was reached, free induction decays (FID), T_2, T_1-T_2, and diffusion measurements were interleaved until the hydrates reached an equilibrium state and no further hydrate formation occurred. This process took anywhere from 15-72 hours as monitored by the decrease of the limiting component water spectral peak. In studies where hydrate inhibitors were introduced to the system, the liquid hydrate inhibitor was mixed with the aqueous phase before freezing.

NMR measurements were performed on a Bruker 250 MHz superconducting magnet integrated to an Avance III spectrometer using a high-power rf probe with a 5 mm radio frequency (rf) coil custom built by Bruker. The high-power rf probe integrates with a Diff30 gradient coil capable of z-direction gradients up to 17 T/m at 60 A and allows for rf pulses at 100 W as short as 1 μs. This probe was used to collect T_1 and T_2 relaxation data by performing 1D T_2 experiments and T_1-T_2 correlation experiments, as well as spectrally resolved diffusion data using a pulsed gradient stimulated echo (PGSE) sequence. Spectrally resolved diffusion measurements were performed using a PGSE sequence with pulse length δ = 1 ms, observation time Δ = 300 ms, 64 gradient steps, and a maximum gradient of 0.7 T/m.

Magnetic resonance imaging (MRI) measurements used a Micro5 gradient coil and probe capable of 3 T/m gradients on all 3 coordinate axes at 60 A. This allowed monitoring of total hydrate formation rate and spatial heterogeneity within the system. A multi-slice multi-echo (MSME) sequence with pulse length δ = 1 ms, and echo time TE =

7.35 ms was used to obtain relaxation and signal intensity maps of hydrates using 8 echoes. The sagittal slice has a thickness of 1 mm and a field of view of 5x30 mm with 64x128 points for a resolution of 0.078 mm/pixel in the x-direction and 0.234 mm/pixel in the z-direction.

T_2 and T_1-T_2 correlation data were acquired using the standard CPMG and inversion recovery pulse sequences with 10 μs rf pulses and an echo time of $\tau_E = 96$ μs. The T_1 and T_2 relaxation times of water and cyclopentane are similar, so to separate the two populations based on relaxation times, a paramagnetic gadolinium complex was added to cyclopentane. The gadolinium complex, gadolinium tetramethyl heptanedionate (Gd(III) TMHD), is only soluble in the organic phase cyclopentane, and will not impact the relaxation rate of the water [11]. To determine the concentration of Gd(III) TMHD needed to separate the relaxation rates of the water and the organic phase, the Gd(III) TMHD concentration was gradually increased in increments of ~0.5%. At 0% Gd(III) only one population representing both phases can be seen in the T_1-T_2 correlation map in Figure 5.2(a). At 2-2.5% concentration TMHD, the relaxation rates of the two phases were clearly separated as shown in Figure 5.2(b), with cyclopentane exhibiting the shorter relaxation times. Full hydrate experiments were run using concentrations of 0.6%, 1.0%, 1.5%, 2.0%, and 2.5%. The concentration of Gd(III) did not impact the formation of hydrate.

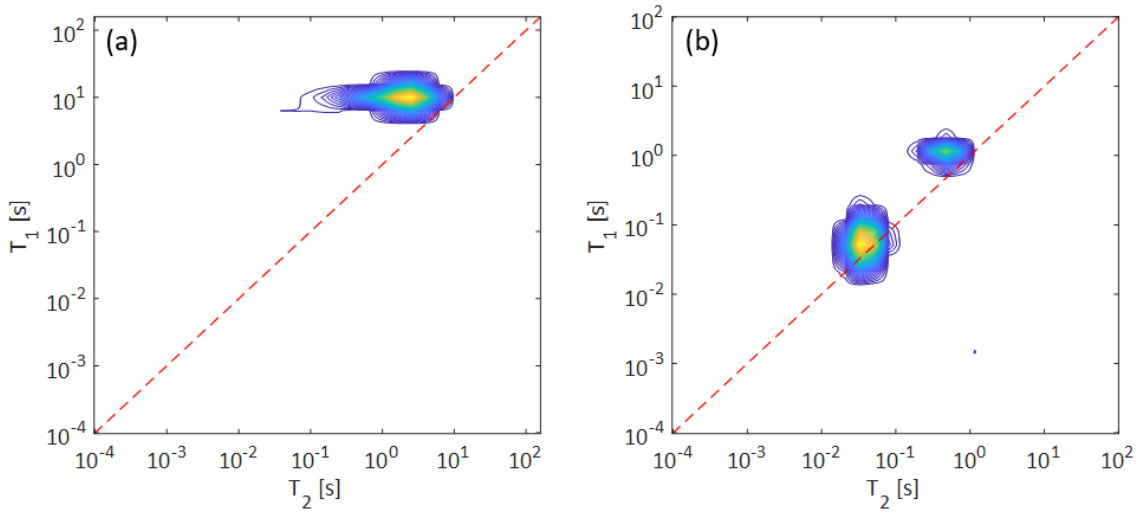

Figure 5.2. T_1-T_2 correlation maps for hydrate containing (a) 0% Gd(III) TMHD and (b) 2.5% Gd(III) TMHD. At 0% Gd(III) TMHD, the water and the cyclopentane population cannot be separated based on relaxation rates. At 2.5% Gd(III) TMHD, the relaxation rate of cyclopentane is fast enough that the two populations are clearly separated.

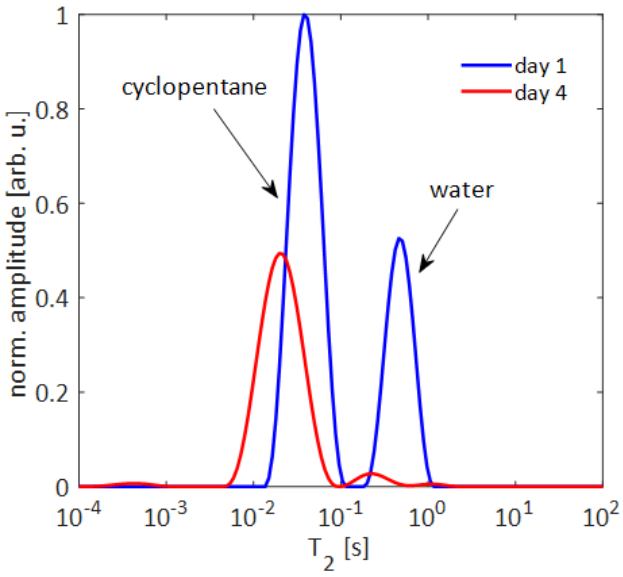

Figure 5.3. T_2 distributions of hydrate with 2.5% Gd(III) TMHD on day 1 (blue) and day 4 (red) after the nucleation temperature is reached, normalized to the maximum of the cyclopentane peak on day 1. As the hydrate formation progresses, a shift to shorter T_2 times a decrease in signal amplitude was observed for both populations. Increase in Gd(III) TMHD concentration causes the shift in T_2 relaxation rate for cyclopentane, while the T_2 shift for water is a result of the water getting more restricted as the hydrate cluster grows. The signal amplitude decreases due to solidification of the water in the hydrate, and single cyclopentane molecules getting trapped in hydrate cages.

T_2 distributions of a hydrate sample with 2.5% Gd(III) TMHD on day 1 and day 4 after the hydrate nucleation temperature of 1°C was reached are shown in Figure 5.3. A shift towards faster relaxation rates is observed for both water and cyclopentane, in agreement with the results obtained at low field by Haber at al. [11] and Gao et al. [24]. The initial T_2 value is ~500 ms for water and ~40 ms for cyclopentane. A shift to shorter T_2 times can be seen for both populations as the hydrate formation progresses, with a final T_2 value of ~200 ms for water and 20 ms for cyclopentane. Additionally, a decrease in signal amplitude with hydrate formation is observed for both water and cyclopentane

when the distributions are normalized to the maximum of the cyclopentane peak on day 1. A shift towards shorter T_2 values for water is expected because the liquid water is gradually confined in smaller and smaller spaces as the hydrate formation progresses. The shift to shorter relaxation times for the cyclopentane is contributed to minor changes in gadolinium concentrations over the formation period since the hydrate formation process occurs in the presence of excess cyclopentane. A progressively higher number of cyclopentane molecules get trapped in hydrate cages, leaving a higher ratio of gadolinium to cyclopentane molecules behind to further increase the relaxation rate of the excess cyclopentane. The decrease in signal amplitude is expected as the T_2 relaxation times of water molecules entrained in hydrate cages, and the cyclopentane molecules trapped within these cages, become too short for the NMR equipment to detect. These results agree with previous low-field NMR measurements of a water-cyclopentane [11] and a deuterium water THF [24] hydrate system.

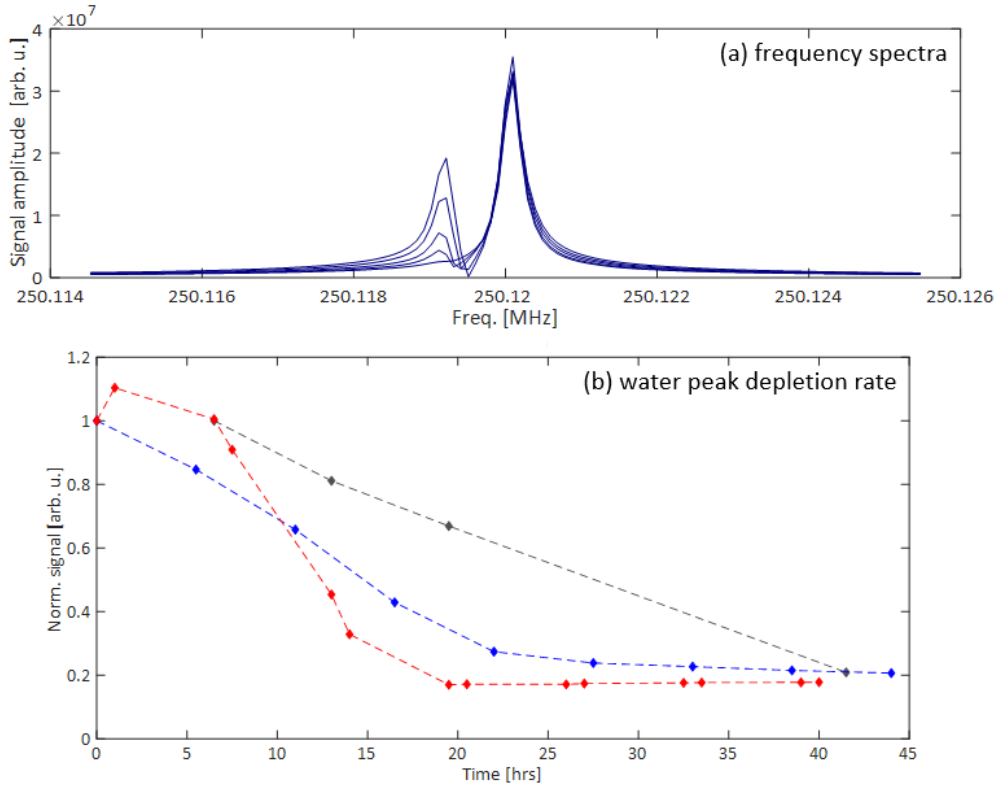

Figure 5.4. (a) frequency spectra showing water (left peak) and cyclopentane (right peak) amplitude throughout the hydrate formation. The water peak disappears due to solidification of the water in the hydrate. (b) water peak depletion rate for three different hydrate studies all at 0.6% Gd(III). The plot indicates varying formation rate even in similar systems. The increase in signal in some experiments at 1 hour indicates all ice was not melted at $t = 0$ hours.

As indicated in the methods, free induction decays (FIDs) were collected throughout the hydrate formation process and Fourier transformed, producing frequency spectra as shown in Figure 5.4. Since 13.5 mol of water are consumed for every one mol cyclopentane [1] and the process is done with excess cyclopentane, the water frequency peak decreases more rapidly than the cyclopentane peak during hydrate formation. Once the water peak is fully depleted, all of the water is entrained in hydrate cages and no further hydrate nucleation and growth will take place. This state is considered to be the equilibrium

state of the hydrate. The variability of the kinetics of the hydrate formation under the same conditions is indicated in Figure 5.4(b). While the rates of formation varied from 15 to more than 40 hours, the resulting molecular dynamics discussed below were consistently similar.

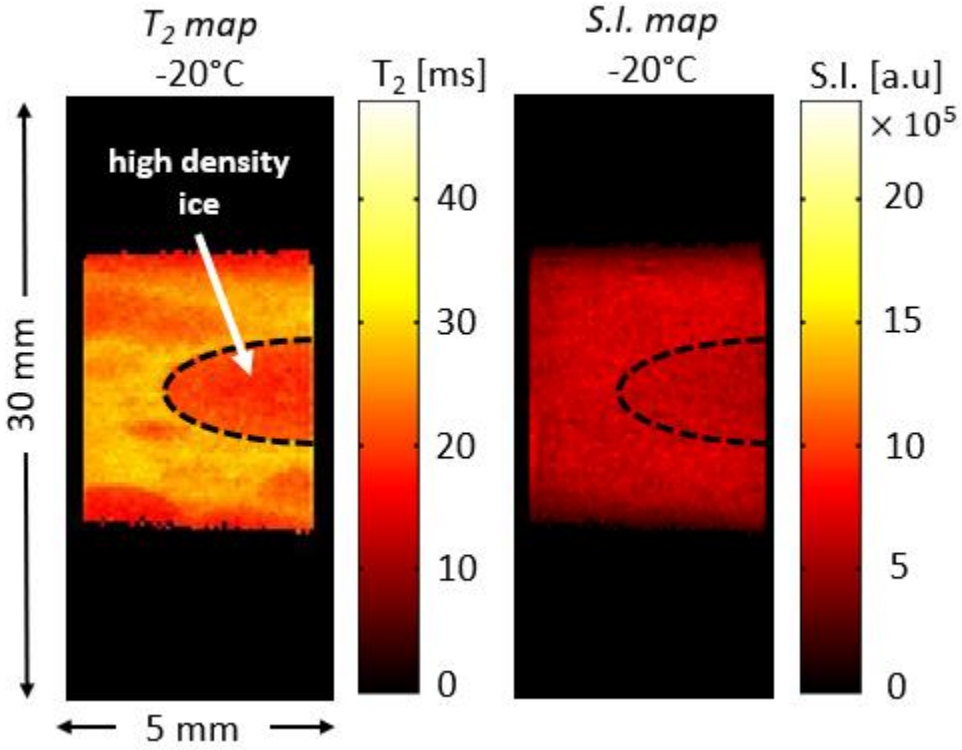

Figure 5.5: T_2 relaxation image (a) and signal intensity image (b) at -20°C before hydrate formation has started. Cyclopentane is the only liquid phase at -20°C. From the relaxation image (a) it can be seen that some regions have faster rates than others. These darker regions consist of densely packed ice where the liquid cyclopentane is more restricted. The signal intensity image indicates that these darker regions have the same concentration of liquid cyclopentane present on the scale of pixels.

Hydrate formation in porous media and in bulk has been studied in detail using MR imaging [10, 17-23]. 2D imaging was used to investigate how the heterogeneity of the hydrate samples affect the formation process. Relaxation images were collected to look for variations in relaxation rates across the hydrate sample, and signal intensity

images were collected to look for variations in cyclopentane concentration within the ice/cyclopentane mixture. Figure 5.5 shows a relaxation image and a signal intensity image at -20°C, where cyclopentane is the only liquid phase in the system. No reaction occurs at this temperature in a cyclopentane/ice system. It can be seen from the relaxation image in Figure 5.5(a) that some regions have slower relaxation rates than others, indicating that the liquid cyclopentane in these areas is more restricted. A signal intensity map of the same hydrate at the same temperature can be seen in Figure 5.5(b). The different regions are more easily visualized in the relaxation image, Figure 5.5(a), because of the low standard deviation of T_2 times within a region, and a 25.6% difference in the average relaxation times between the two regions. The signal intensity (Figure 5.5(b)) within the region with shorter relaxation times has a standard deviation that is two times the difference in signal intensity between the two regions, and an average difference in signal intensity of only 5%. Thus, the low difference in signal intensity along with the high standard deviation in the signal intensity map makes it hard to differentiate between regions. However, the 5% difference in signal intensity confirms that the ice particles are more densely packed in regions with shorter T_2 times.

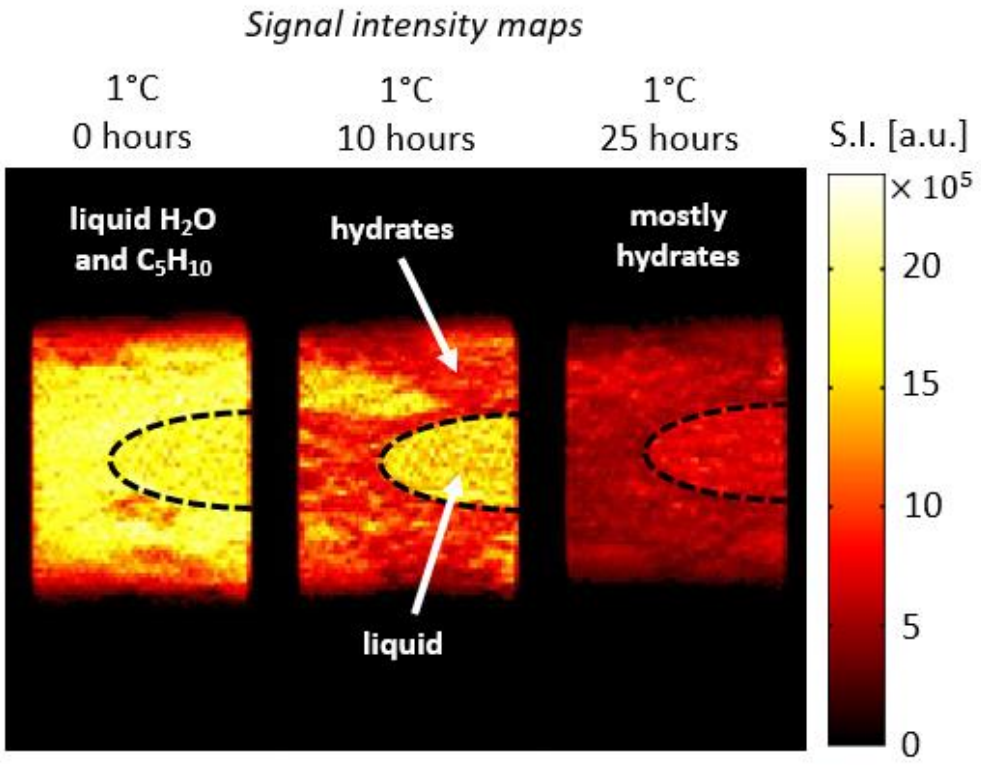

Figure 5.6. MR images showing the signal intensity at 0, 10, and 25 hours in a hydrate sample as the growth progresses. In these images, the system is at 1°C, and the liquid phase consist of both cyclopentane and water. At 0 hours, the bright yellow color of the T_2 map indicates plenty of liquid water and cyclopentane. As the hydrate formation progresses, the signal intensity across the sample decreases as the water is entrained in hydrate cages. Additionally, the MR images show that hydrate formation occurs more slowly in areas with initial high ice density (indicated by the dashed line).

Figure 5.6 shows signal intensity maps of a hydrate cluster at 0, 10, and 25 hours after the nucleation temperature of 1°C was reached. At 1°C, the ice particles start to thaw, and there is both liquid cyclopentane and liquid water present in the system. Yellow regions are areas with high signal and plenty of liquid cyclopentane and water, while dark red regions are areas with hydrate. At 0 hours, the signal intensity is high across the entire sample, with the high level of liquid phase making it impossible to distinguish between low- and high-density ice regions. However, as the hydrate

formation progresses, the signal intensity decreases, and the previously distinguishable regions reappear, indicating that the hydrates form at a slower rate in some regions of the sample. This is due to the higher water droplet concentration as melting occurs from the ice particles having been more densely packed in these regions. The cyclopentane does not penetrate as easily and the hydrate reaction is limited by the cyclopentane transport into the high-density water region. Hydrate nucleation occurs at water cyclopentane interfaces and is therefore likely to occur more rapidly in areas where the ice particles are initially highly saturated with cyclopentane. The cyclopentane/ice surface contact is greater when the ice particles melt while more evenly dispersed throughout the liquid cyclopentane phase. The results confirm that hydrate formation rates have significant variations due to the spatial heterogeneity of the initial distribution of water and organic phase within a sample. Similar observations have been made in a methane-water hydrate system [19].

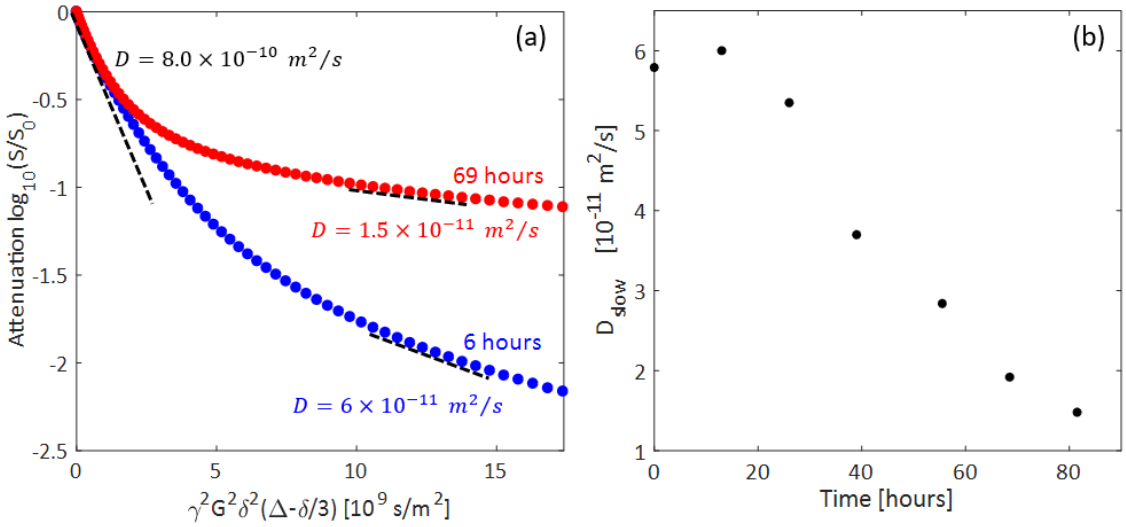

Figure 5.7. a) Stejskal-Tanner plot showing the water phase at 6 (blue) and 69 (red) hours after the onset of hydrate growth. At 6 hours, a majority of the signal originates from larger droplets of water with a diffusion coefficient at the order of 10^{-10} as indicated by the fast low-q decay. At 69 hours, an increase in the ratio of signal originating from water within the porous hydrate shell can be seen. The water trapped in the pore space of the hydrate shell has a diffusion coefficient at the order of 10^{-11}. b) A decrease in the slower diffusion coefficient with hydrate growth progression is observed.

As discussed earlier and shown in Figure 5.1, following initial hydrate nucleation, a thin layer of hydrate will form a shell around the suspended water droplets [9, 11]. With time, the hydrate shell increases in thickness [36]. This reduces the hydrate growth rate due to mass transfer limitations of the excess organic phase cyclopentane to the water interface through the hydrate agglomerate porous media [31, 32, 36, 37]. Spectrally resolved diffusion data indicate two separate diffusion coefficients for water, one fast on the order of 10^{-10} and one slow on the order of 10^{-11} (Figure 5.7(a)). The signal attenuation data shown in Figure 5.7(a) is biexponential with contributions from both the slow and fast diffusion. The fast diffusion coefficient ($8 \times 10^{-10}\ m^2/s$) is close to that of free water at 1 °C [38] and is attributed to water in the droplets larger in size than 50

μm as $\Delta = 300\ ms$ is not long enough to detect restricted diffusion in these large droplets. The slow diffusion coefficient is attributed to the water trapped within the dendritic structure of the porous hydrate shell. The decrease in the slow diffusion coefficient with the progression of hydrate growth indicates a decrease in the pore sizes of the hydrate shell. This can be confirmed by estimating the mean square displacement of hydrogen nuclei in the system given by $\langle \boldsymbol{Z^2} \rangle = 2D\Delta$, where *D* is the measured diffusion coefficient, and Δ is the observation time in the PGStE measurement. Figure 5.7(b) shows the slow diffusion coefficient decreasing as the hydrate growth progresses. Here, $\Delta = 300\ ms$ is kept constant for all measurements, thus a decreasing diffusion coefficient results in a decrease in mean square displacement from $\boldsymbol{Z} = \sqrt{2D\Delta}$ of 6 μm to 2.45 μm, confirming that the hydrate shell is getting less porous.

The molecular dynamics during hydrate formation have been modeled using classical molecular dynamics simulations [1, 3, 39] and phase field models [40, 41]. These models predict complicated diffusion dynamics due to molecular reorientations and interactions during nucleation and subsequent hydrate growth that occurs on timescales of the order of microseconds (~1 μs) and nanometer length scales (~ 1 nm) [39]. The NMR data is acquired with high power rf pulses of duration 10 μs and echo spacing 2τ = 192 μs. Hence the hydrates themselves with a T_2 < 200 μs are not detected, the NMR signal results from liquid state molecules. During the spin echo evolution period a large number of hydrate formation events are occurring at the cyclopentane water fluid interfaces throughout the 5 mm diameter 1 cm long rf coil. These molecular reorientation events are occurring constantly throughout the data sampling period. The

acquired T_1-T_2 correlation data is impacted by these complex diffusion dynamics. The data, conditioned to display exponential decay for ILT inversion, exhibits an initial rise in signal with experimental time τ_1 as has been demonstrated by Song et al. [42]. The signal rise is due to complex diffusion dynamics from coupling between pores of varying size and surface relaxivity [42, 43]. The complex diffusion dynamics in the hydrates includes multiple pore sizes, inter-pore diffusion or exchange, and surface relaxation of the cyclopentane within the porous structure formed by the hydrate agglomeration.

Maneval at al. [43] recently showed, using a coupled pore model [44, 45], that a T_1-T_2 signal rise is highly dependent on pore size ratio, pore connectivity, and coupling of relaxation modes. The results of their simulation show that a signal rise is observed for coupling of T_1 and T_2 relaxation modes in a specific combination of the fast and slow diffusion regime, where the fast diffusion regime is defined as $\frac{a\rho_{1,2}}{D} \gg 1$, and the slow diffusion regime is $\frac{a\rho_{1,2}}{D} \ll 1$ [43, 46]. Here, a is the pore diameter and, D is the diffusion coefficient, and $\rho_{1,2}$ is the surface relaxivity for the T_1 and T_2 relaxation modes. When mixed mode conditions for fast and slow diffusion regimes are met, an increase in the amplitude of the dominating negative eigenmode is observed. These negative amplitude eigenmodes reduces the stability of inverse Laplace transformations [47-49], and are known to reduce the resolution of, and produce $T_1<T_2$ peaks in T_1-T_2 correlation maps as shown in Figure 5.8. Consequently, when high amplitude negative eigenmodes are present, T_1-T_2 correlation maps are unreliable. Instead, results should be obtained from the T_1-T_2 time-domain data directly as indicated by Song et al. [42]. The presence of aphysical peaks in the ILT is sporadic even when the signal rise is robust, thus a signal

rise may be present even when no T_1<T_2 peaks are observed in the T_1-T_2 correlation map, emphasizing the importance of using the more robust time-domain data.

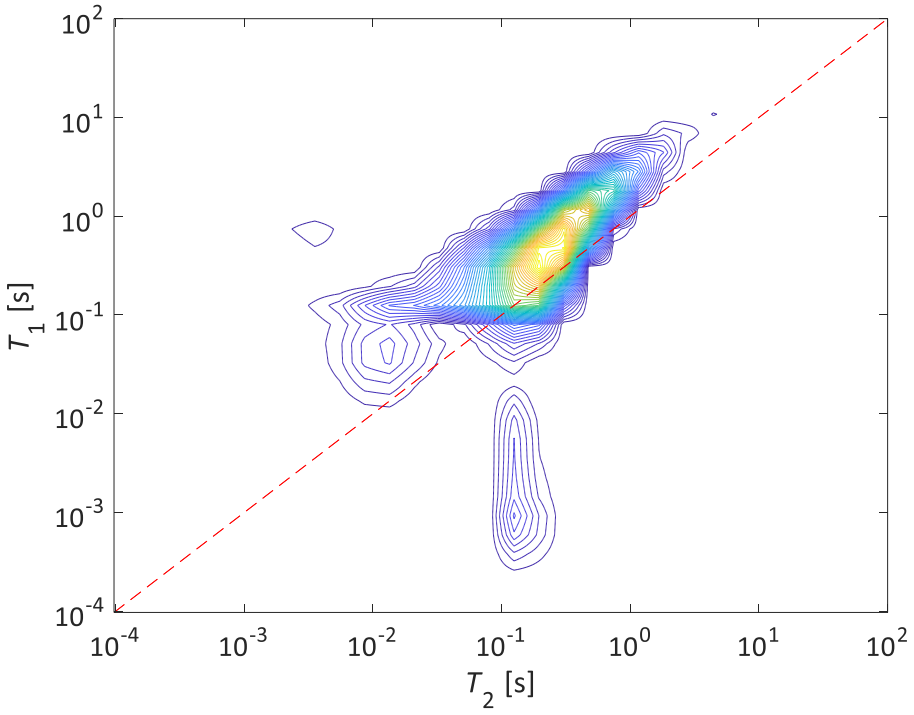

Figure 5.8. T_1-T_2 relaxation correlation map showing a peak in the forbidden (T_1<T_2) zone resulting from a high amplitude negative eigenmode. The T_1<T_2 peaks appear in part due to instability of the inverse Laplace transformation in the presence of negative eigenmodes and resulting signal increase in the τ_1 experimental domain.

Another requirement for the signal rise observed by Maneval et al. is an intermediate level of connectivity, given by an exchange parameter κ_c, between the coupled regions [43]. If $\kappa_c \to 0$ the regions are completely isolated with no magnetization exchange, and no signal rise is observed. If $\kappa_c \to \infty$, the regions are fully connected, and the system reduces to a single pore system which also does not produce a signal rise. The connectivity between bulk cyclopentane and hydrate agglomerate porous regions in a hydrate system gradually changes throughout the formation process playing a significant

role in the T_1-T_2 time domain signal rise observed in the hydrate phase transition dynamics.

During early hydrate formation $\kappa_c \to \infty$ due to the thin and highly porous hydrate shell surrounding the water droplets. Towards the end of the hydrate growth, $\kappa_c \to 0$ as the hydrate shell becomes impermeable. The signal rise observed in the hydrates (Figure 5.9(a)) occur exclusively during the intermediate stage of the hydrate formation when the hydrate agglomerate porosity is stable around $\varphi \leq 50\%$ [29]. By the time the water is fully depleted, and the hydrate has reached an equilibrium state, the T_1-T_2 time domain data returns to its usual processed form exponential decay (Figure 5.9(b)), thus the hydrate data is consistent with the results from the coupled pore model [43].

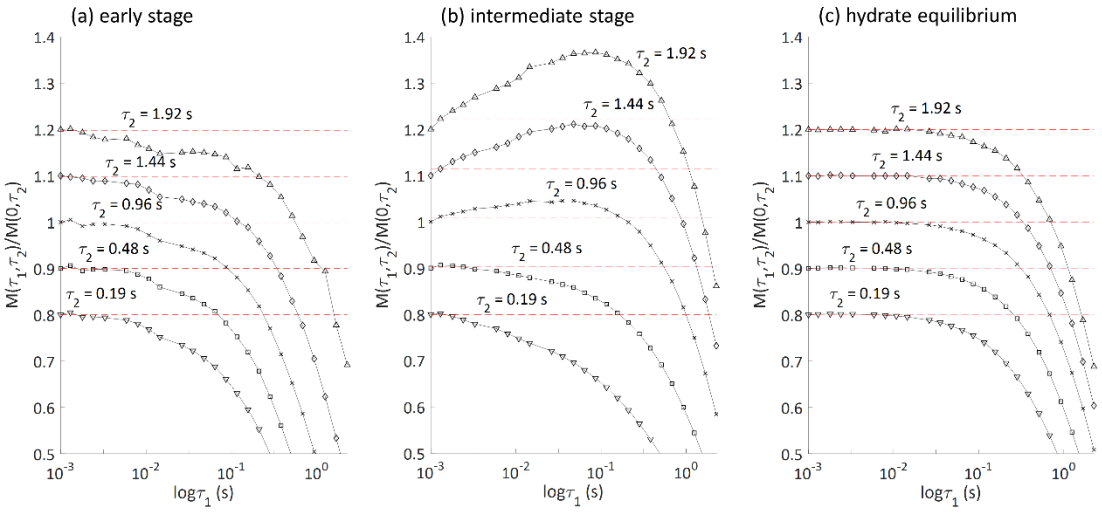

Figure 5.9. T_1-T_2 time domain data processed to show exponential decay for ILT analysis. (a) Early stage of hydrate formation process at 6 hours (b) intermediate stage of hydrate formation process at 14 hours, and (c) hydrate equilibrium state at 21 hours. An initial increase in signal was observed during the intermediate stage of the hydrate growth process. The data sets are manually shifted vertically at each τ_2 for easier visualization of each individual data set. By the time the hydrate reaches an equilibrium state and hydrate growth was complete, the signal returns to the exponential decaying signal typically observed for processed T_1-T_2 correlation data**.**

Following the early stage of hydrate formation, further hydrate growth along with the exchange of magnetization due to molecular diffusion of cyclopentane bewteen regions of bulk organic phase and pore space within the hydrate agglomerate become mass-transfer limited and depends on the diffusivity of the hydrocarbon molecules through the shell as well as the porosity of the shell [37]. The transport of hydrocarbon molecules through the shell is a slow process compared to the frequency at which the NMR signal is collected during T_1-T_2 measurements. Therefore, the effect of the complex diffusion dynamics on the NMR measurements becomes greater with time, as can be seen in the T_1-T_2 time domain data in Figure 5.9(b). The initial signal increase becomes more pronounced at longer τ_2-times, since the diffusion exchange between regions of different relaxation and diffusion dynamics occurs at longer τ_2-times [42, 43].

To further investigate the ability of T_1-T_2 relaxation correlation measurements to provide novel data on hydrate formation dynamics, LDHIs were added to the aqueous phase. The first LDHI used, Luvicap® 55W (provided by BASF, Global Oilfield Solutions), is a KHI which interferes with hydrate nucleation and the formation of hydrate crystals. The second LDHI is an industrial AA (provided by Nalco Champion, Ecolab) which prevents hydrate particles from agglomerating.

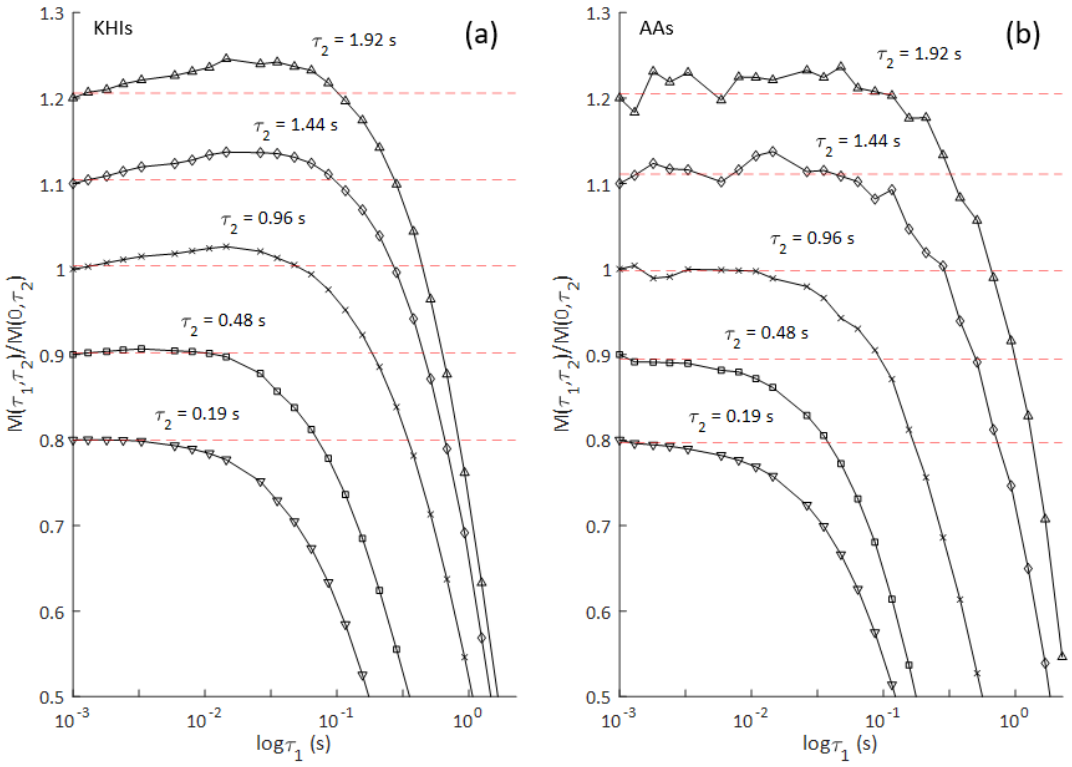

Figure 5.10. T_1-T_2 time domain data collected during the intermediate stage of the hydrate formation process in the presence of (a) KHIs and (b) AAs. A signal rise was observed in presence of KHIs due to the fact that KHIs do not disrupt the agglomoration of hydrate crystals, thus a hydrate shell will still form around the water droplets. No signal rise was observed in the presence of AAs. AAs prevent hydrate crystals from agglomerating and resulting in a slurry of fine hydrate particles which do not form a shell encapsulating the water droplets.

The frequency spectra (not shown, data as in Figure 5.4) collected during the inhibitor studies show that there was indeed a long delay in the onset of hydrate growth when the KHI was added to the system. The delay was typically 24-48 hours relative to the same conditions without KHIs, and no T_1-T_2 signal increase is observed during this initial delay. After 24-48 hours, hydrates began to form and a signal rise was again observed during the intermediate stage of the hydrate formation (Figure 5.10(a)). As indicated, KHI will delay initial hydrate nucleation, but will not prevent the hydrate

crystals from agglomerating once the hydrate growth has started. Hence formation of a porous layer of hydrate agglomerates will occur as a shell around the water droplets suspended in the liquid hydrocarbon phase and an evolving porous media occurs after initial delay, just as in the absence of inhibitors. A signal rise is thus observed in this system as the hydrate formation process is identical to that of hydrates growing in the absence of KHI.

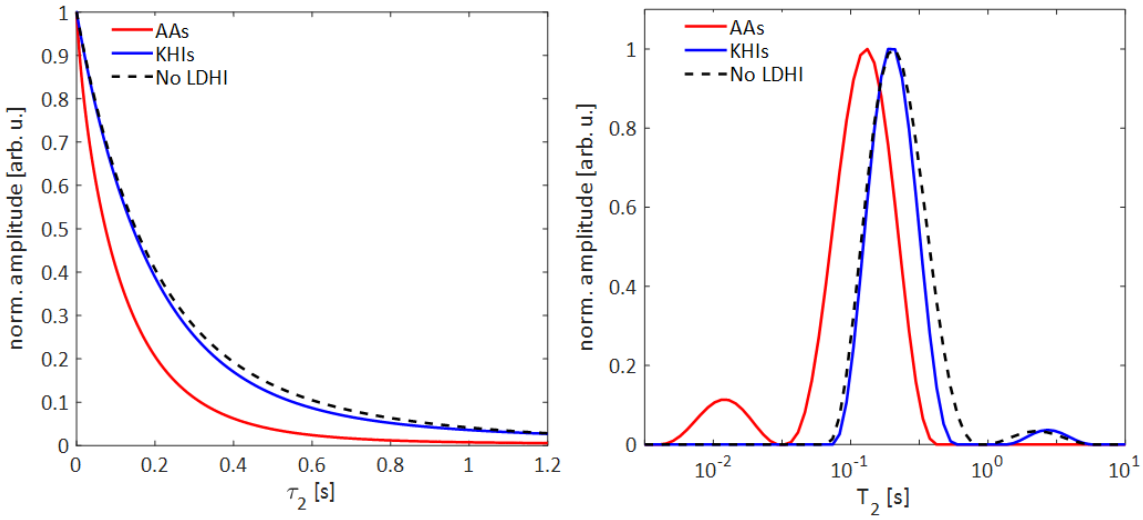

Figure 5.11. (a) signal decay in hydrates forming in the presence of KHIs (blue) and AAs (red), and in the absence of a LDHI (black) as a function of τ_2 and (b) corresponding T_2 distributions. In the presence of AAs, a more rapid decay of the NMR signal is observed resulting a shorter T_2 time (~135 ms) compared to the T_2 time (~200 ms) of hydrates forming with KHIs present. The shorter T_2 of hydrates with AAs indicate smaller hydrate particles more uniformly dispersed in cyclopentane. The T_2 time of hydrates with KHI is identical to that of hydrates growing in the absence of a LDHI confirming that the mechanism of the hydrate formation in the presence of KHI is not different once it starts.

Conclusion

Hydrate formation andgrowth was detected and monitored by frequency spectra obtained using ^{1}H NMR measurements. Frequency spectra also indicated the hydrate equilibrium state at which point no further hydrate growth was indicated by no further change in the

water peak. 1D T_2 distributions show a decrease in peak amplitude for both water and cyclopentane, and a shift to shorter T_2 times for water consistent with low field measurements [11, 24]. Water entrained in hydrate cages and cyclopentane molecules trapped witthin these cages exhibit relaxation times too short to detect due to hardware limitations, thus the decrease in T_2 distribution amplitude indicates the extent of hydrate formation. The decrease in T_2 relaxation time for water indicates a decrease in water droplet size as the hydrate shell surrounding the water droplet increases in thickness. MRI intensity and T_2 relaxation maps indicate spatially dependent hydrate formation rates determined by the density of the packed ice which was heterogeneous. Hydrates grow more rapidly in regions with low ice density due to the increased area of the water-cyclopentane interface. This spatial heterogeneity is related to variations in the rate of hydrate formation observed under the same conditions in the water peak spectra. Spectrally resolved diffusion measurements indicate two distinct diffusion coefficients for the aqueous phase, differing by approximately one order of magnitude. The faster diffusion coefficient is attributed to larger water droplets likely located in regions with high ice density. The slow diffusion coefficient decreases with the progression of hydrate formation, and is attributed to water trapped within the porous hydrate shell. The decrease of the diffusion coefficient indicates a reduction in the pore sizes of the hydrate agglomerate as the hydrate shell increases in thickness.

A novel signal rise is observed in the T_1-T_2 data which indicates that during the intermediate stage of the hydrate growth, when the shell porosity has decreased to $\leq$ 50%, the system consist of two regions, where one region, the trapped water droplets, is

in the fast diffusion regime, and the other region, the cyclopentane, is on the slow diffusion regime. The porous hydrate shell determines the connectivity between the two regions and thus controls the existence as well as the amplitude of the signal rise. The data indicates complex diffusion dynamics [42] due to coupling between regions of varying diffusion and relaxation. This research indicates the ability to characterize phase transition molecular dynamics by high-field NMR relaxometry and diffusometry during hydrate formation due to evolution of the hydrate agglomerate porous structure.

Acknowledgements

M. L. Johns, E. O. Fridjonsson, S. J. Vogt, Z. Aman, and N. Ling of Univ. of Western Australia for assistance with hydrate production and materials. J. D. Seymour and S. L. Codd acknowledge the Murdoch Charitable Trust for equipment funding and Dieter Gross of Bruker for construction of the high power rf probe. S. L. Codd acknowledges NSF CBET-1335534.

References

1. Sloan, E.D. and C.A. Koh, *Clathrate Hydrates of Natural Gases, Third Edition*. Clathrate Hydrates of Natural Gases, Third Edition. Vol. 119. 2008, Boca Raton: Crc Press-Taylor & Francis Group. 1-701.

2. Chatti, I., et al., *Benefits and drawbacks of clathrate hydrates: a review of their areas of interest.* Energy Conversion and Management, 2005. **46**(9-10): p. 1333-1343.

3. Koh, C.A., et al., *Fundamentals and Applications of Gas Hydrates*, in *Annual Review of Chemical and Biomolecular Engineering, Vol 2*, J.M. Prausnitz, Editor. 2011, Annual Reviews: Palo Alto. p. 237-257.

4. Hammerschmidt, E.G., *Formation of gas hydrates in natural gas transmission lines.* Industrial and Engineering Chemistry, 1934. **26**: p. 851-855.

5. Sloan, E.D., *Fundamental principles and applications of natural gas hydrates.* Nature, 2003. **426**(6964): p. 353-359.

6. Ripmeester, J.A., et al., *A New Clathrate Hydrate Structure.* Nature, 1987. **325**(6100): p. 135-136.

7. Warrier, P., et al., *Overview: Nucleation of clathrate hydrates.* Journal of Chemical Physics, 2016. **145**(21).

8. Ripmeester, J.A. and S. Alavi, *Some current challenges in clathrate hydrate science: Nucleation, decomposition and the memory effect.* Current Opinion in Solid State & Materials Science, 2016. **20**(6): p. 344-351.

9. Aichele, C.P., et al., *Nuclear Magnetic Resonance Analysis of Methane Hydrate Formation in Water-in-Oil Emulsions.* Energy & Fuels, 2009. **23**(1): p. 835-841.

10. Bagherzadeh, S.A., et al., *Magnetic Resonance Imaging of Gas Hydrate Formation in a Bed of Silica Sand Particles.* Energy & Fuels, 2011. **25**(7): p. 3083-3092.

11. Haber, A., et al., *Hydrate Shell Growth Measured Using NMR.* Langmuir, 2015. **31**(32): p. 8786-8794.

12. Kleinberg, R.L., et al., *Deep sea NMR: Methane hydrate growth habit in porous media and its relationship to hydraulic permeability, deposit accumulation, and*

submarine slope stability. Journal of Geophysical Research-Solid Earth, 2003. **108**(B10): p. 17.

13. Davidson, D.W., S.K. Garg, and J.A. Ripmeester, *NMR Behavior of Clathrate Hydrate of Tetrahydrofuran .2. Deuterium Measurements.* Journal of Magnetic Resonance, 1978. **31**(3): p. 399-410.

14. Ripmeester, J.A., S.K. Garg, and D.W. Davidson, *NMR Behavior of the Clathrate Hydrate of Tetrahydrofuran .3. Effect of Oxygen.* Journal of Magnetic Resonance, 1980. **38**(3): p. 537-544.

15. Pietrass, T., et al., *Monitoring Xenon Clathrate Hydrate Formation on Ice Surfaces with Optically Enhanced XE-129 NMR.* Journal of the American Chemical Society, 1995. **117**(28): p. 7520-7525.

16. Ripmeester, J.A. and C.I. Ratcliffe, *Low-Temperature Cross-Polarization Magic Angle Spinning C-13 NMR of Solid Methane Hydrates - Structure, Cage Occupancy, and Hydration Number.* Journal of Physical Chemistry, 1988. **92**(2): p. 337-339.

17. Kvamme, B., et al., *Storage of CO2 in natural gas hydrate reservoirs and the effect of hydrate as an extra sealing in cold aquifers.* International Journal of Greenhouse Gas Control, 2007. **1**(2): p. 236-246.

18. Zhao, J.F., et al., *In-situ visual observation for the formation and dissociation of methane hydrates in porous media by magnetic resonance imaging.* Magnetic Resonance Imaging, 2015. **33**(4): p. 485-490.

19. Moudrakovski, I.L., et al., *Methane and carbon dioxide hydrate formation in water droplets: Spatially resolved measurements from magnetic resonance microimaging.* Journal of Physical Chemistry B, 2004. **108**(45): p. 17591-17595.

20. Baldwin, B.A., A. Moradi-Araghi, and J.C. Stevens, *Monitoring hydrate formation and dissociation in sandstone and bulk with magnetic resonance imaging.* Magnetic Resonance Imaging, 2003. **21**(9): p. 1061-1069.

21. Mondrakovski, I.L., et al., *Hydrate layers on ice particles and superheated ice: a H-1 NMR microimaging study.* Journal of Physical Chemistry A, 1999. **103**(26): p. 4969-4972.

22. Susilo, R., et al., *Hydrate kinetics study in the presence of nonaqueous liquid by nuclear magnetic resonance spectroscopy and imaging.* Journal of Physical Chemistry B, 2006. **110**(51): p. 25803-25809.

23. Yang, M.J., et al., *Advances in nuclear magnetic resonance (NMR) techniques for the investigation of clathrate hydrates.* Renewable & Sustainable Energy Reviews, 2017. **74**: p. 1346-1360.

24. Gao, S.Q., W.G. Chapman, and W. House, *Application of low field NMR T-2 measurements to clathrate hydrates.* Journal of Magnetic Resonance, 2009. **197**(2): p. 208-212.

25. Nakajima, M., R. Ohmura, and Y.H. Mori, *Clathrate Hydrate Formation from Cyclopentane-in-Water Emulsions.* Industrial & Engineering Chemistry Research, 2008. **47**(22): p. 8933-8939.

26. Sloan, E.D., et al., *Quantifying hydrate formation and kinetic inhibition.* Industrial & Engineering Chemistry Research, 1998. **37**(8): p. 3124-3132.

27. Kashchiev, D. and A. Firoozabadi, *Induction time in crystallization of gas hydrates.* Journal of Crystal Growth, 2003. **250**(3-4): p. 499-515.

28. Skovborg, P., et al., *Measurement of Induction Times for the Formation of Methane and Ethane Gas Hydrates.* Chemical Engineering Science, 1993. **48**(3): p. 445-453.

29. Rao, I., et al., *Gas Hydrate Deposition on a Cold Surface in Water-Saturated Gas Systems.* Industrial & Engineering Chemistry Research, 2013. **52**(18): p. 6262-6269.

30. Karanjkar, P.U., J.W. Lee, and J.F. Morris, *Surfactant Effects on Hydrate Crystallization at the Water-Oil Interface: Hollow-Conical Crystals.* Crystal Growth & Design, 2012. **12**(8): p. 3817-3824.

31. Genov, G., et al., *Experimental studies on the formation of porous gas hydrates.* American Mineralogist, 2004. **89**(8-9): p. 1228-1239.

32. Chen, L.T., et al., *Methane Hydrate Formation and Dissociation on Suspended Gas Bubbles in Water.* Journal of Chemical and Engineering Data, 2014. **59**(4): p. 1045-1051.

33. Kelland, M.A., *History of the development of low dosage hydrate inhibitors.* Energy & Fuels, 2006. **20**(3): p. 825-847.

34. Gao, S.Q., *Hydrate Risk Management at High Watercuts with Anti-agglomerant Hydrate Inhibitors.* Energy & Fuels, 2009. **23**(3-4): p. 2118-2121.

35. Zylyftari, G., A. Ahuja, and J.E. Morris, *Nucleation of cyclopentane hydrate by ice studied by morphology and rheology.* Chemical Engineering Science, 2014. **116**: p. 497-507.

36. Taylor, C.J., et al., *Macroscopic investigation of hydrate film growth at the hydrocarbon/water interface.* Chemical Engineering Science, 2007. **62**(23): p. 6524-6533.

37. Sun, C.Y., et al., *The growth kinetics of hydrate film on the surface of gas bubble suspended in water or aqueous surfactant solution.* Journal of Crystal Growth, 2007. **306**(2): p. 491-499.

38. Mills, R., *Self-diffusion in normal and heavy water in the range 1-45.deg.* The Journal of Physical Chemistry, 1973. **77**(5): p. 685-688.

39. Walsh, M.R., et al., *Microsecond Simulations of Spontaneous Methane Hydrate Nucleation and Growth.* Science, 2009. **326**(5956): p. 1095-1098.

40. Kvamme, B., et al., *Phase Field Approaches to the Kinetic Modeling of Hydrate Phase Transitions*, in *Natural gas hydrates - Energy resource potential and associated geological hazards*. 2009, The American Association of Petroleum Geologists. p. 758-769.

41. Tegze, G., L. Granasy, and B. Kvamme, *Phase field modeling of CH4 hydrate conversion into CO2 hydrate in the presence of liquid CO2.* Physical Chemistry Chemical Physics, 2007. **9**(24): p. 3104-3111.

42. Song, Y.Q., et al., *Experimental Identification of Diffusive Coupling Using 2D NMR.* Physical Review Letters, 2014. **113**(23): p. 5.

43. Maneval, J.E., et al., *A Two-Region Transport Model for Interpreting T_1-T_2 Measurements in Complex Systems.* To be submitted Journal of Magnetic Resonance, 2018.

44. Belton, P.S. and B.P. Hills, *The Effects of Diffusive Exchange in Heterogeneous Systems on NMR Line-Shapes and Relaxation Processes.* Molecular Physics, 1987. **61**(4): p. 999-1018.

45. Belton, P.S. and B.P. Hills, *The Effects of Exchange and Interfacial Reaction in 2-Phase Systems on NMR Lineshapes and Relaxation Processes.* Molecular Physics, 1988. **65**(2): p. 313-326.

46. Brownstein, K.R. and C.E. Tarr, *Importance of Classical Diffusion in NMR-Studies of Water in Biological Cells.* Physical Review A, 1979. **19**(6): p. 2446-2453.

47. Song, Y.Q., L. Zielinski, and S. Ryu, *Two-dimensional NMR of diffusion systems.* Physical Review Letters, 2008. **100**(24): p. 4.

48. Bytchenkoff, D. and S. Rodts, *Structure of the two-dimensional relaxation spectra seen within the eigenmode perturbation theory and the two-site exchange model.* Journal of Magnetic Resonance, 2011. **208**(1): p. 4-19.

49. Johnson, D.L. and L.M. Schwartz, *Analytic theory of two-dimensional NMR in systems with coupled macro- and micropores.* Physical Review E, 2014. **90**(3): p. 032407.

DETECTING MICROBIALLY INDUCED CALCITE PRECIPITATION IN POROUS SYSTEMS USING LOW-FIELD NUCLEAR MAGNETIC RESONANCE RELAXOMETRY

Contributions of Authors and Co-Authors

Manuscript in Chapter 6

Author: Linn W. Thrane

Contributions: Assisted with experimental design and implementation. Performed all experimental studies. Performed NMR measurements and and analyzed NMR data. Wrote manuscript.

Co-Author: Ryanne L. Daily

Contributions: Assisted in design and implementation of study. Assisted in preparation of bacteria culture and injection media and analyzed effluent samples. Provided feedback and comments on manuscript.

Co-Author: Abby Thane

Contributions: Assisted in design and implementation of study. Provided feedback and comments on manuscript.

Co-Author: Catherine M. Kirkland

Contributions: Provided feedback and comments on manuscript.

Co-Author: Evan R. McCarney

Contributions: Assisted with initial set-up of Rock Core Analyzer and implementation of NMR measurements. Helped with data interpretation. Provided feedback and comments on manuscript.

Co-Author: Robin Dykstra

Contributions: Provided the Rock Core Analyzer. Provided feedback and comments on manuscript.

Co-Author: Sarah. L. Codd

Contributions: Assisted with experimental design and implementation. Helped with data interpretation. Assisted in writing of manuscript. Provided feedback and comments on manuscript.

Co-Author: Adrienne J. Phillips

Contributions: Assisted with experimental design and implementation. Helped with data interpretation. Provided feedback and comments on manuscript.

Manuscript Information Page

Linn W. Thrane, Ryanne L. Daily, Abby Thane, Catherine M. Kirkland, Evan R. McCarney, Robin Dykstra, Sarah L. Codd, Adrienne J. Phillips

Environmental Science & Technology

Status of Manuscript:
_X_Prepared for submission to a peer-reviewed journal
____Officially submitted to a peer-review journal
____Accepted by a peer-reviewed journal
_ __Published in a peer-reviewed journal

American Chemical Society

DETECTING MICROBIALLY INDUCED CALCITE PRECIPITATION IN POROUS SYSTEMS USING LOW-FIELD NUCLEAR MAGNETIC RESONANCE RELAXOMETRY

Abstract

Low-field nuclear magnetic resonance has been shown to be sensitive to the chemical and physical changes in a porous medium caused by microbially induced calcite precipitation (MICP), confirming its potential for detection of MICP for subsurface engineering applications. This investigation used a 2 MHz Rock Core Analyzer, measuring T_2 relaxation, in combination with scanning electron microscopy to characterize the daily chemical and physical changes occurring in various granular media including 1 mm and 0.5 mm silica glass beads, and 1 mm, and 0.45 mm quartz sand. An increase in T_2 time was observed in all of the granular media in accordance with MICP progression due to the formation of a gas interface between the pore walls and bulk liquid. An estimate of the surface relaxivity, ρ, was obtained for the silica glass, quartz sand, the gas, and the mineral precipitate which allowed for a direct correlation between the presence of the gas interface and T_2 relaxation time, and an indirect correlation between mineral precipitation surface coverage and T_2 relaxation time. The results indicate the potential for detailed *in-situ* MICP progress monitoring during the early stages of the process by portable low-filed NMR devices.

Introduction

Controlled microbially induced calcite precipitation (MICP) has been widely researched in recent years as its usage is becoming increasingly prevalent in various engineering applications such as environmental remediation, enhanced construction materials [1, 2] subsurface fracture sealing [3-5], and CO_2 sequestration [4]. The ability to monitor the progress of MICP is essential for successful large-scale field applications. Imaging techniques such as micro CT, scanning electron microscopy (SEM), and X-ray diffraction (XRD) have been used extensively in small scale laboratory studies to detect MICP [6, 7]. However, it is difficult to apply the above imaging techniques in a non-destructive manner, and they are limited to small scales, which makes them unsuitable for *in-situ* monitoring of MICP at the large scale required for industrial field applications. In large scale laboratory studies, or field scale studies, a decrease in permeability or an increase in pressure has been used to indicate the presence of MICP as shown by Phillips et. al. in their work on fracture sealing [3] and CO_2 leakage reduction [4] by MICP. The disadvantage to detecting MICP by permeability and pressure monitoring is the lack of information on MICP processes occurring at the pore scale.

Nuclear magnetic resonance (NMR) is a non-invasive measuring technique that is sensitive to parameter changes such as pore size, pore fluid, and the chemical composition of pore wall surfaces. Fridjonsson et al. [8] used high field NMR to measure changes in hydrodynamic dispersion resulting from MICP in a model porous system of packed monodisperse polystyrene beads. By using a combination of magnetic resonance imaging (MRI) and NMR displacement measurements they were able to monitor the

alteration of the pore structure with time. Sham et al. [9] used NMR and MRI to monitor MICP in a model porous media consisting of borosilicate beads, and in a Bentheimer sandstone. MRI was used to acquire a spatial distribution of calcite perception and their results indicate that precipitation is highly homogeneous.

Rocks and natural sediments are made up of materials with high magnetic susceptibilities and therefore pose a challenge for high field NMR measurements as the measurements are subject to potential susceptibility artifacts. By using an NMR instrument with a low magnetic field, the effect of susceptibility artifacts can be reduced. Low-field NMR instruments are smaller and lighter than high-field instruments, and several portable low-field NMR tools are available today. Kirkland et al. used a portable low-field NMR well-logging probe to monitor MICP in a sand-filled bioreactor by measuring NMR signal amplitude and T_2 relaxation times over an 8 day period. The measured NMR signal amplitude revealed a 76% decrease in water content over the experimental period, additionally an increase in T_2 relaxation time from 650 ms to over 1000 ms was observed [10]. The ability to detect MICP by NMR measurements makes portable NMR tools a promising method for *in-situ* monitoring of MICP in large-scale engineering applications. In this work, a 2 MHz Rock Core Analyzer (RCA) from Magritek in combination with scanning electron microscope (SEM) imaging was used with the aim to further investigate how MICP affects NMR relaxometry. In porous media, T_2 relaxation predominantly depends on pore size and the surface minerology of the pores and has the potential to provide detailed information about the changes that occur within the porous system during MICP.

NMR Theory

The RCA is a bench top NMR instrument best suited for laboratory experiments. It is equipped with a 1D gradient and has a vertical bore that can hold samples with a diameter up to 39 mm. It uses a permanent magnet that produces a static magnetic field, $\mathbf{B_0}$, in the vertical direction. The RCA NMR signal results from hydrogen protons in water referred to as "spins", and the initial amplitude of the NMR signal is proportional to the total water volume in the sampled region. The observed decay rate of the NMR signal over time reflects the local physical and chemical environment of the spins. In porous media, the T_2 relaxation rate is given by [11, 12]

$$\frac{1}{T_2} = \frac{1}{T_{2,B}} + \frac{1}{T_{2,S}} + \frac{1}{T_{2,D}} \qquad (6.1)$$

Where $\frac{1}{T_{2,B}}$ is the bulk relaxation rate of the pore fluid which is sensitive to fluid properties such as viscosity, $\frac{1}{T_{2,S}}$ is the surface relaxation rate which occurs when excited spins interact with paramagnetic ions at the pore wall and is related to the minerology of the pore walls and the pore size, and $\frac{1}{T_{2,D}}$ is the diffusion relaxation rate which is related to the diffusion of spins between regions of local magnetic field inhomogeneities [11, 13]. At low magnetic fields, experimental parameters for T_2 measurements can be selected to minimize the influence of diffusion relaxation to the point where $T_{2,D}$ can be neglected in Equation (6.1) [13, 14]. That means that the T_2 relaxation rate in a porous system is dominated by the surface relaxation rate which occurs when the spins are close to or interact with the pore walls. The surface relaxation rate can be expressed in terms of

a surface relaxivity, ρ, which depends on the minerology of the pore walls, and the surface to volume ratio of the pore [15].

$$\frac{1}{T_{2,S}} = \rho \frac{S}{V} \qquad (6.2)$$

It is expected that the surface relaxation rate will govern potential changes observed in the overall T_2 relaxation rate, although the bulk relaxation term will need to be included also

$$\frac{1}{T_2} = \rho \frac{S}{V} + \frac{1}{T_{2,B}} \qquad (6.3)$$

For this system, pore sizes will decrease and the surface relaxivity will decrease in magnitude as calcite precipitates on the surface of the glass beads or sand [10]. From Equation (6.3), a reduction in surface relaxivity will result in a slower relaxation rate, while a decrease in pore size will result in a faster relaxation rate. In the case of heterogeneous pore sizes or varying surface relaxivity, multiple T_2 relaxation rates will be observed.

Microbially Induced Calcite Precipitation

Biofilms form when groups of microorganisms adhere to surfaces in a matrix of extracellular polymeric substance (EPS) [16]. When the microorganisms in the biofilm are ureolytic, MICP can be induced through various biochemical processes, with the most common method being urea hydrolysis as it is considered the most efficient method for MICP [17]. Ureolytic bacteria produce the enzyme urease which promotes urea hydrolysis, which then leads to the generation of ammonia and carbonic acid. This is followed by an increase in pH of the bulk fluid as the ammonia reacts with water to form

ammonium and hydroxide ions inducing a shift in the carbonate equilibrium toward bicarbonate and carbonate. With sufficient calcium present, the calcium and carbonate precipitate as calcium carbonate or calcite. Urea hydrolysis and calcite precipitation can be summarized by the following chemical reactions:

$$CO(NH_2)_2 + 2H_2O \xrightarrow{Urease} H_2CO_3 + 2NH_3 \qquad (6.4)$$

$$CO_3^{2-} + Ca^{2+} \rightarrow CaCO_{3(s)} \qquad (6.5)$$

The microorganism chosen for this study, *Sporosarcina pasteurii* (*S. pasteurii*), formerly known as *Bacillus pasteurii*, has been studied extensively due to its ability to produce large quantities of intracellular urease [6, 18, 19]. The biofilm containing *S. pasteurii* will form on the surface of the sand grains or glass beads, calcite precipitation within the biofilm will then bind the grains together resulting in an overall reduction in pore volume.

Materials and Methods

Experimental Configuration

A 1-inch diameter and 12-inch-long glass column filled with either glass beads or sand grains was used for all experiments in this work. The inlet was connected with silicone tubing to a syringe pump used to inject media at controlled flow rates, while the column outlet allowed for media waste to flow to a waste container. Quick connects were used at the inlet and outlet of the column so that the column could easily be disconnected from the tubing and placed in the RCA for NMR measurements. A pressure gauge was integrated in the tubing before the inlet to monitor pressure increase as calcite

precipitation began to restrict flow through the column. Mesh filters were placed at both the inlet and outlet to prevent glass beads or sand grains from migrating into the tubing. The flow direction was vertical, from bottom to top of the column. All experiments were run until either the column was fully congested or no further changes in the NMR measurements were observed. A range of granular media were used in this work to further investigate the effect of simultaneous changes in minerology and pore size on the T_2 relaxation rates observed by Kirkland et al. [10]. The granular media used included 1 mm and 0.5 mm soda lime glass beads from BioSpec Products, and 1 mm and 0.45 mm nominal quartz sand grains (2095 and 4095 Granusil silica sand, Unimin Corp., Ottawa, MN)

Injection Strategy

A pulsed-flow injection strategy was used for the culture and media injection to allow the bacteria to attach to the granular media surfaces and ensure an even distribution of calcite precipitation throughout the column. Two pore volumes of culture containing *S. pasteurii* followed by two pore volumes of growth medium were injected at 0.5 ml/min in the evening to allow the bacteria to resuscitate overnight. In the morning, two pore volumes of a calcite precipitation-promoting medium were injected followed by a stationary batch reaction period of 3 hours before a second calcium medium injection and 3-hour batch reaction period. An effluent sample was collected following each medium injection to check the remaining urea concentration which indicates the activity level of the bacteria in the column. This procedure was repeated daily until the end of the study.

NMR Measurements

The 2 MHz Rock Core Analyzer used for this study is particularly well suited for NMR measurements of samples with high magnetic susceptibilities due to its low magnetic field. It operates at a large bandwidth which enables measurements of short T_2 decay times and is equipped with a one-dimensional gradient in the z-direction, allowing 1D imaging and T_2 measurements each day during MICP. The 1D images, or 1D signal intensity profiles, were executed using the standard spin warp imaging technique [20], with 25 μs and 50 μs pulse duration for the $\pi/2$ and π excitation pulses respectively, an echo time of $\tau_e = 500\ \mu s$, and a maximum gradient amplitude of 4 mT/m. The T_2 measurements were executed using the standard Carr-Purcell-Meiboom-Gill (CPMG) pulse sequence [21, 22] with an echo time of $\tau_e = 150\ \mu s$, 10000-30000 echoes, depending on the stage of the calcite precipitation process, 25 μs and 50 μs pulse durations for the $\pi/2$ and π excitation pulses respectively, and a dwell time of 1 μs. The minimum signal to noise ratio (SNR) was set to 100 for the T_2 measurements, so that the number of averages performed depended on the liquid volume in the column. NMR measurements were performed twice daily, in the morning before the first calcium medium injection, and in the afternoon before the culture injection.

Scanning Electron Microscopy

Scanning electron microscopy (SEM) was used to look at the mineral precipitation coating on the sand grains and glass beads after the study was completed. The column was dried out post study and cut into 6 smaller sections, each approximately 2 in long. Sand grains or glass beads were then removed from the same section of each

column, rinsed in DI water to remove any residual salt on the surface and dried. A Zeiss Supra 55VP scanning electron microscope (Zeiss, USA) was used to capture images of the surface of the granular media at magnifications ranging from 250-5000x. Additionally, column sections from each study were re-saturated to obtain post study T_2 relaxation and porosity data. During one of the studies performed on 0.5 mm glass beads, samples of beads were removed from the top of the column daily and went through the same rinse and drying procedure. This allowed for investigation of the correlation between mineral precipitation surface coverage and changes in the T_2 relaxation rate.

Results and Discussion

For each experimental run NMR data was collected for the bottom and the top of the column to ensure there were no major differences in calcite precipitation throughout the system. No significant differences in signal intensity or T_2 distributions were observed between the top and bottom sections in any of the granular media indicating a highly homogeneous mineral precipitation throughout the column. Consequently, all T_2 distributions and signal intensity profiles shown will be from the bottom of the column. 1D images and T_2 measurements confirming spatial homogeneity are shown in Figure A.1 in Appendix A.

The results from three experiments in different granular material are shown in Figure 6.1, 0.5 mm glass beads, 1 mm glass beads and 1 mm sand grain. The amplitude of the NMR signal is proportional to the water volume in the column, thus the change in NMR signal amplitude from the first to the final day of the study provides a measure of

the decrease in total pore volume occupied by water due to calcite precipitation. The decrease in water volume in the column with time can be attributed to two main changes in the local environment that occur due to calcite precipitation: the presence of additional solid (calcite) in the porous medium and gas bubble creation. Calcite precipitates on the surface of the granular media as shown in the SEM image inserts in Figure 6.1. It is clearly visible that the calcite layer is thin and should not cause a significant change in the primary pore size, however, it is likely to cause a small reduction in total pore volume as it will block smaller channels and pore throats. The T_2 distributions in Figure 6.1 all exhibit a low amplitude, short T_2 time population on the first day of the study representing liquid in the smaller pore throats. By the final day of the study, this shorter T_2 population has either experienced a drastic decrease in amplitude, or completely disappeared. The final signal decrease by the end of the studies range from -6.7% to -33.6% with the larger signal decreases representing the longer studies lasting 10-15 days. The longer the study lasts, the more precipitate and gas will form in the column. Additionally, the smaller granular medium, 0.5 mm glass beads, show an overall larger signal decrease than the larger granular media, likely due to the smaller pore throats trapping precipitate and gas more efficiently.

Table 6.1
Sample data

Parameter	0.5 mm glass 7 days	1.0 mm glass 15 days	1.0 mm sand 6 days
Porosity, φ, (%) day 1	41.9	42.0	41.0
Porosity, φ, (%) re-saturated	31.9	31.4	31.7
T_2 (s) day 1	0.38	0.6	0.6
T_2 (s) day final	0.9	1.35	1.20
T_2 (s) re-saturated	0.43	0.67	0.76
ρ $(\mu m/s)$ day 1	120.6	125.7	120.7
ρ $(\mu m/s)$ day final	22.8	9.7	17.7
ρ $(\mu m/s)$ re-saturated	79.7	72.8	58.8

From Equation (6.1), the T_2 relaxation rate will be governed by changes in pore size or changes in surface relaxivity caused by a changing pore wall minerology. Additionally, gas production is likely to have a significant impact on the relaxation time if it alters the accessibility of the water to the surface. A decrease in the pore size of the system should result in a faster relaxation rate unless the effect of a changing surface minerology or the presence of gas on the surface outweighs the effect due to a change in pore size. A slower relaxation rate is observed on the final day of the study for each granular medium. An overview of the T_2 relaxation times on the first and final day and the measured NMR porosity on the first day and the re-saturated column can be found in Table 6.1. An increase in T_2 relaxation time between the first and final day of 74.3% and 125.7% is observed for the 1 mm and 0.5 mm soda lime glass beads respectively. A 59.2% increase in T_2 relaxation time is observed for the 1 mm quartz sand grains. The increase in T_2 time of the quartz sand grains is in close agreement with the increase of approximately 55-65% observed by Kirkland et al. [10]. The T_2 relaxation times obtained from the re-saturated sections are all within 15% of the T_2 time on the first day of the

study. The similar T_2 time on the first day and the re-saturated section, combined with the decrease in porosity indicate that calcite has a lower magnitude surface relaxivity than glass or sand [23]. The large increase in T_2 observed between the first and final day is therefore likely caused by gas bubble creation on the calcite surface, reducing the accessibility of water to the surface and decreasing the effect of surface relaxation which is a strong relaxation mechanism in porous media. The final day ρ is then representative of gas coated calcite.

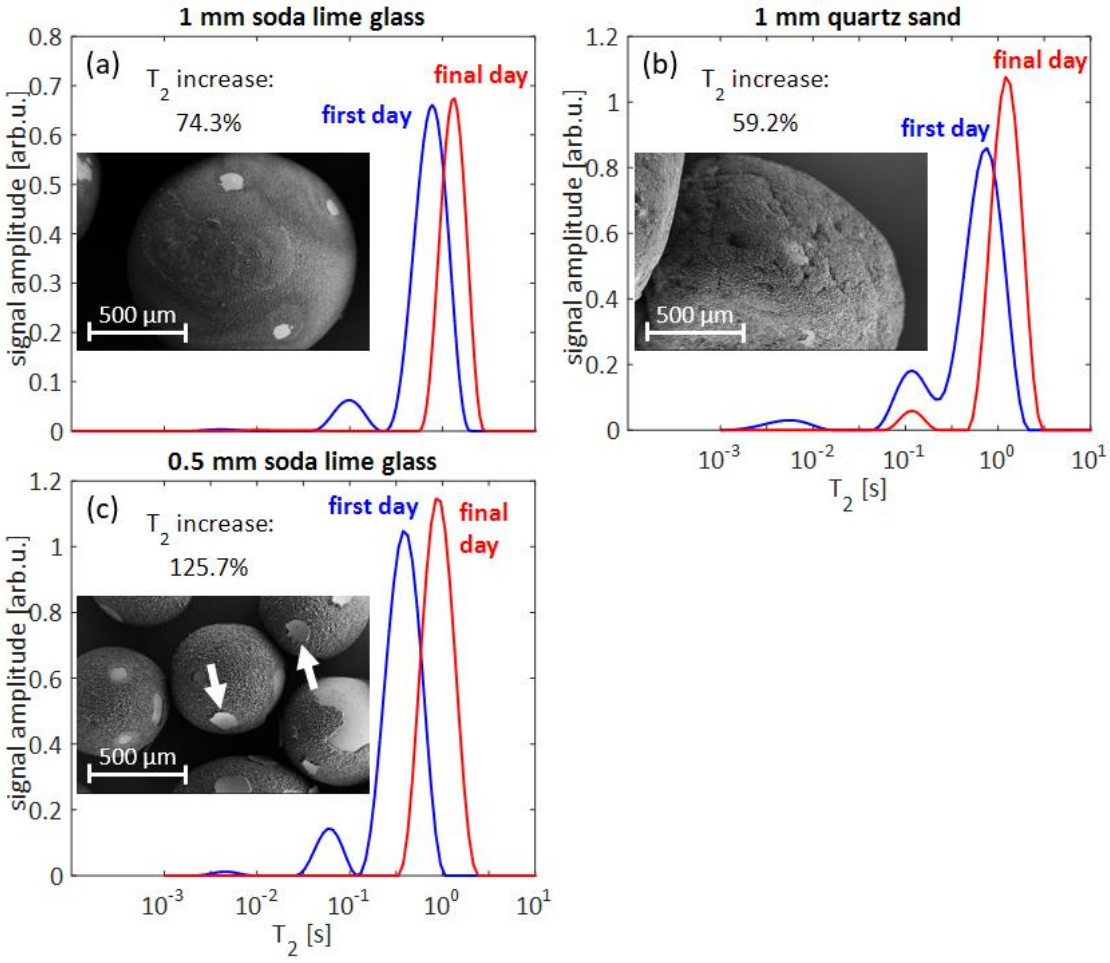

Figure 6.1. T_2 distributions on the first and final day of experiments for (a) 1 mm soda lime glass beads, (b) 1 mm quartz sand grains, and (c) 0.5 mm soda lime glass beads. An increase in T_2 relaxation time and decrease in area is consistently observed in all distributions during the experimental time. Since the pore sizes in the system are getting smaller due to calcite precipitation, the increase in T_2 times must be a result of a decrease in magnitude of the surface relaxivity, ρ, due to the formation of a gas interface. SEM images of granular media removed from column following the completion of the studies are shown next to each T_2 distribution. The granular media are all completely covered in mineral precipitation by the end of the experiments. The exposed areas result from breaking the beads apart upon removal from column. Flakes of mineral precipitation from other beads are highlighted with arrows.

SEM images taken after the study was completed show complete calcite coverage for these representative samples. The areas that are not covered by calcite precipitation are

areas where the beads were connected to other beads, and the layer of calcite was broken off when the beads were removed from the column. This is particularly apparent in the SEM image of the 0.5 mm glass beads where layers from other beads (highlighted with arrows) are still sticking to the surface of the beads in the image.

For a system consisting of monodispersed spherical glass beads, the surface to volume ratio is directly related to the porosity, φ of the system and the diameter d of the beads [24]

$$\frac{S}{V} = \frac{6 * (1 - \varphi)}{d * \varphi} \quad (6.6)$$

All the granular media shown in Figure 6.1 can be reasonably approximated as monodispersed spheres both initially and at the end of the calcite precipitation. As previously mentioned, the initial amplitude of the NMR signal is proportional to the total water volume in the sampled region, thus the porosity φ of the system can be found by means of NMR. By combining Equation (6.6) and Equation (6.3), an estimate of the surface relaxivity ρ_{sand} and ρ_{glass} can be obtained using the porosity values along with the first day measured T_2 times as shown in Equation (6.7). A value of $T_{2,B} = 1.6$ s was determined by measuring the T_2 of both water and the calcite injection fluids.

$$\rho = \frac{d * \varphi}{6 * T_{2,S} * (1 - \varphi)} \quad (6.7)$$

The relaxivity values obtained for the glass and sand are similar to those previously reported by Song et al. [25] prior to a rinsing procedure that stripped paramagnetic impurities from the surfaces.

Equation (6.7) was also used to calculate $\rho_{calcite}$ with the re-saturated measurements of T_2 under the assumption that the system still consisted of monodispersed spherical beads but with a lower $\frac{S}{V}$ due to the thin layer of calcite precipitation. This lower $\frac{S}{V}$ was estimated using final day bead diameters of 0.6 mm (glass) and 1.1 mm (glass and sand). These final day bead diameters were estimated by calculating the total volume of calcite that precipitated in the column over the duration of the study and dividing the volume by the total surface area of the beads. The total volume of calcite precipitated was estimated by subtracting the amount of $CaCO_3$ leaving the column, which was obtained from the effluent samples, from the amount of $CaCO_3$ injected. An accurate measurement of the thickness of the calcite layer is difficult to obtain from the SEM images, but a ~0.05 mm thick layer appears to be a realistic estimate. To get an accurate final porosity value, the column was fully saturated with distilled water after the experiment.

In the 1 mm glass beads and sand grains, the initial T_2 time is similar for the two systems indicating that the two systems have both similar pore sizes and surface relaxivity. The 1 mm granular media have longer initial T_2 times than the 0.5 mm granular medium due to the fact that the surface relaxivity contributes to the relaxation of the NMR signal and less frequent wall interactions in larger pores will result in a slower decay rate leading to longer T_2 times. The larger increase in T_2 time for the 0.5 mm glass beads compared to the 1 mm glass and sand beads is attributed to the smaller pore size and the greater influence of surface relaxivity. The values obtained for $\rho_{calcite}$ are higher than expected which may be attributed to the assumption that the calcite precipitate is a

smooth surface. The SEM images clearly show that the calcite surface is textured, resulting in a significant underestimate of the surface area and thus an overestimate of the surface relaxivity of calcite.

SEM images of 0.5 mm glass beads collected from the column daily during one of the studies allowed for a visual correlation between the mineral precipitation surface coverage and changes in T_2 relaxation rate. The comparison of the daily SEM images with the corresponding T_2 distributions, Figure 6.2, indicates a direct relationship between surface coverage percentage and T_2 relaxation time. The most significant increase in surface coverage occurs between day 1 and 2 and is accompanied by the most significant increase in T_2 time. Beyond the first 24 hours, a steady increase in T_2 time is observed until full precipitation coverage is obtained.

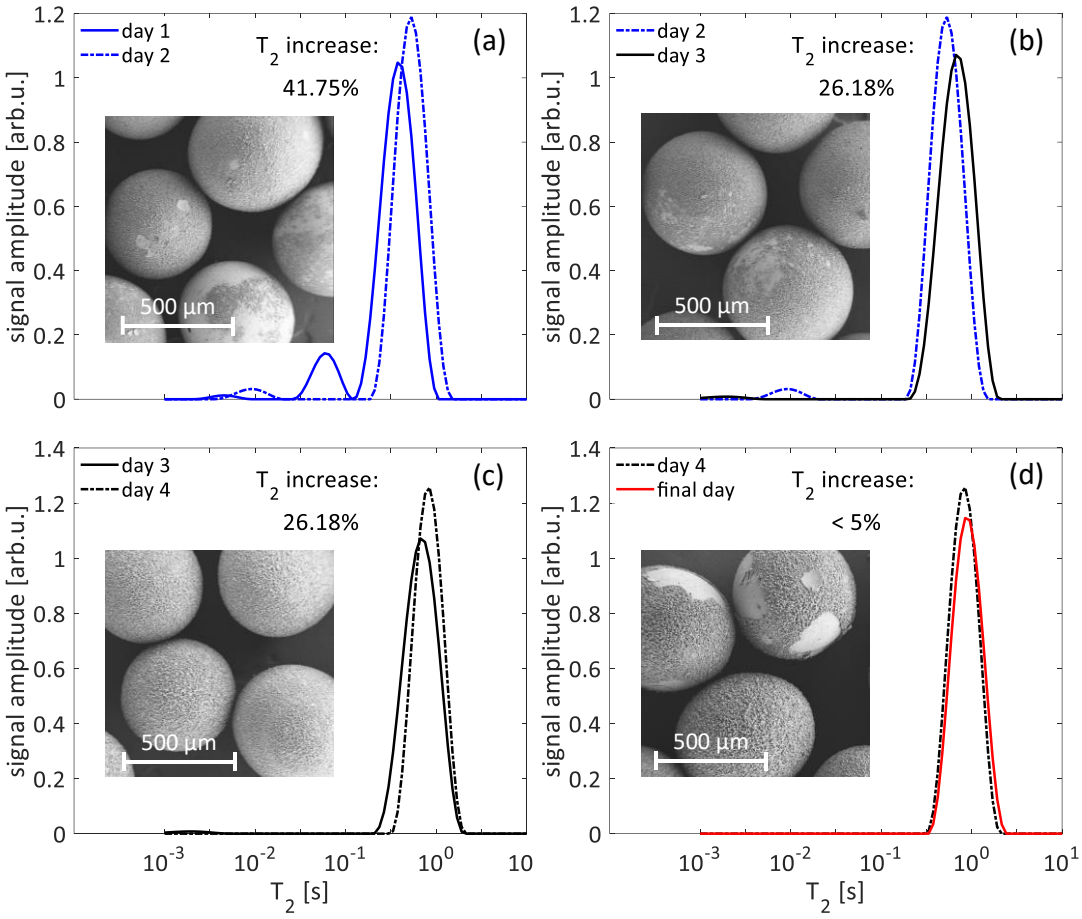

Figure 6.2. Daily SEM images and corresponding T_2 distributions of 0.5 mm glass beads. The SEM images show a gradual increase in the percentage of the surface area covered with mineral precipitation until the beads are fully covered on day 4. A steady increase in T_2 time is observed until the beads are fully covered, at which point the T_2 time stabilizes and a further increase of less than 5% is observed by the final day of the study.

The strong correlation between surface coverage and T_2 time is interesting considering the $< 15\%$ difference in T_2 times observed between the re-saturated column and the un-covered granular media and can be explained by the behavior of the gas on the smooth glass or sand surface versus the textured calcite surface. The textured calcite surface traps the gas on the surface whereas the smooth glass surfaces do not, resulting in

an even distributed gas interface wherever calcite is present. This gas interface diminishes the effect of the surface relaxation mechanism, resulting in a significant increase in T_2 relaxation times. The presence of larger gas bubbles trapped in the pore space will lead to a decrease in T_2 time as demonstrated in Figure A.2 in Appendix A, thus the increase in T_2 cannot be attributed to the presence of gas, but rather how the gas is distributed in the pore space.

To further explore the correlation between surface coverage and T_2 times, the values for porosity and surface relaxivity in Table 6.1 were then used to obtain an estimate of the daily calcite surface coverage of the 0.5 mm glass beads using the following expression

$$\frac{1}{T_{2,S}} = \left(x\rho_{glass} + (1-x)\rho_{gas}\right)\frac{S}{V} \qquad (6.8)$$

Where ρ_{glass} and ρ_{gas} is the relaxivity of the glass and gas interface, respectively, and is given by the relaxivity on the first and final day for the 0.5 mm glass beads in Table 6.1. x is the fraction of the remaining exposed glass surface, and $\frac{S}{V}$ is calculated using Equation (6.6) with the day 1 porosity of the 0.5 mm glass. A constant $\frac{S}{V}$ was assumed since porosity values are only available for the first and final day of the study. The calculated surface coverage is given in Table 6.2 along with the daily T_2 values for the plots in Figure 6.2. The secondary T_2 population is much smaller in amplitude than the main T_2 population and does not have a significant contribution to the NMR signal, thus it was not included in the calculation.

Table 6.2

T_2 times for Figure 6.2 and 0.5 mm glass calcite surface coverage

Day	T_2, main (s)	T_2, secondary (s)	Surface coverage (%)
1	0.38	0.06	0
2	0.53	0.01	45.5
3	0.67	-	69.9
4	0.85	-	89.3
final	0.87	-	90.9 (98.2)*(100.5)**

*surface coverage calculated using $\frac{S}{V}$ obtained from the porosity value on the final day of the study

**surface coverage calculated using $\frac{S}{V}$ obtained from the porosity value on the final day of the study, T_2 from the re-saturated column, and $\rho_{calcite}$

The trend of the calculated surface coverage aligns well with the observed surface coverage in the SEM images in Figure 6.2. The largest increase in surface coverage occurs between day 1 and 2 and continues to increase at a steady rate until the glass beads are fully covered on day 4. By the final day, the surface coverage should have reached 100%, but according to our calculations it has only reached 90.9%. Evidently, the assumption of constant $\frac{S}{V}$ is problematic since the porosity of the system changes throughout the experiment as observed by the first and final day porosity measurements. If instead we find $\frac{S}{V}$ using the porosity measured on the final day and recalculate the surface coverage, a final surface coverage of 98.2% is obtained. Additionally, a final day surface coverage of 100.5% was obtained using the final day $\frac{S}{V}$, the T_2 time from the re-saturated column, and $\rho_{calcite}$ instead of ρ_{gas}. The similarity between the two surface coverage values (98.2% and 100.5%) obtained using the final day $\frac{S}{V}$ indicate that if daily porosity values had been made, an accurate estimate of the percentage surface coverage

could be obtained using this method despite the presence of the gas interface. Future studies will include this step.

Following the three studies discussed above, two additional studies on 0.45 mm quartz sand grains were performed. In both studies on the 0.45 mm quartz sand grains, a pressure increase was detected before the T_2 distributions had equilibrated around one final T_2 time, thus the studies were ended early. It is likely that the different behavior is due to the non-uniform and jagged shape of the 0.45 mm sand grains compared to the close to spherical shape of the 1 mm sand grains. The sand grains were not fully covered in calcite by the final day in either of the studies, Figure 6.3. In an attempt at estimating the final surface coverage of the sand by other means than visual observation, ρ_{sand} and $\rho_{calcite}$ (estimated as the average of the three values obtained for calcite) from Table 6.1, along with the T_2 time from the re-saturated section, were used to solve Equation (6.8) for the final surface coverage percentage. $\frac{S}{V}$ was assumed to stay constant and was obtained using Equation (6.3) and the T_2 time from day 1. The final day calcite precipitation coverage was found to be 49.7%, which appears to be a realistic number when compared to the SEM image in Figure 6.3. In future work, more accurate surface to volume ratios will be obtained by other means to provide a more precise estimate of both the surface coverage and the relaxivity of the various materials.

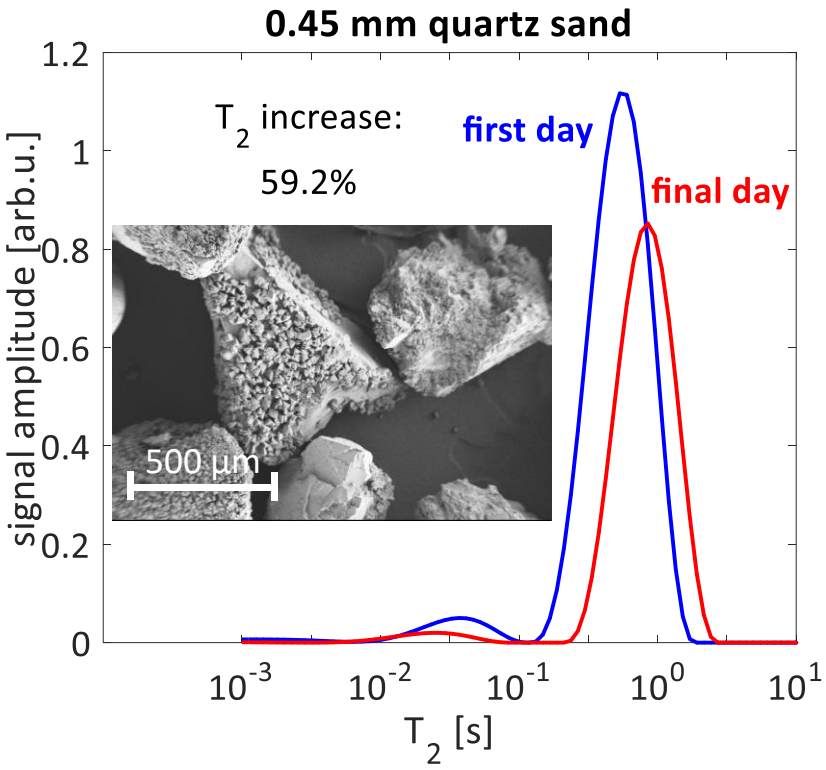

Figure 6.3. T_2 distributions of the 0.45 mm sand on the first and final day and SEM image of sand grains collected from the column after the study was completed. A T_2 increase of 59.2% was observed in the 0.45 mm sand, and the SEM image shows that the grains are only partially covered with calcite precipitate. The partial coverage is likely the reason why a larger increase in T_2 time was not observed.

NMR relaxation measurements have the potential for *in-situ* monitoring of MICP in large-scale engineering applications. This work used 1D T_2 relaxation measurements accompanied by SEM imaging to provide a detailed look at how the changes in geometric structure and mineralogy of the system undergoing MICP affects the acquired NMR signal. The NMR results indicate that the change in T_2 relaxation time due to MICP is predominantly a result of the formation of a gas interface due to the MICP, and not due to the changing surface mineralogy or the decrease in pore volume. Interestingly, the results of this work indicate a strong correlation between surface coverage and T_2 relaxation

times indicating that the gas coating of the surface is correlated to the calcite surface coverage. The presence of a gas interface will be investigated further in future studies. An increase in T_2 times were observed for all experimental systems in this work, though the magnitude of the increase depends on both the size and the material of the granular media, and the T_2 time reaches a steady state value for all systems at a time corresponding to when the calcite covers all surfaces. The results indicate the potential for *in-situ* MICP progress monitoring during the early stages of the process by portable low-field NMR devices. The T_2 measurements can provide *in-situ* monitoring of the degree of progression of resulting surface coverage of the MICP process.

Acknowledgements

This material is based upon work supported by the Department of Energy under Grants No. DE-FE0024296 and DE-FE0026513. Any opinions, findings, conclusions or recommendations expressed herein are those of the authors and do not necessarily reflect the views of the Department of Energy (DOE).

References

1. De Muynck, W., N. De Belie, and W. Verstraete, *Microbial carbonate precipitation in construction materials: A review.* Ecological Engineering, 2010. **36**(2): p. 118-136.

2. Siddique, R. and N.K. Chahal, *Effect of ureolytic bacteria on concrete properties.* Construction and Building Materials, 2011. **25**(10): p. 3791-3801.

3. Phillips, A.J., et al., *Fracture Sealing with Microbially-Induced Calcium Carbonate Precipitation: A Field Study.* Environmental Science & Technology, 2016. **50**(7): p. 4111-4117.

4. Phillips, A.J., et al., *Potential CO2 Leakage Reduction through Biofilm-Induced Calcium Carbonate Precipitation.* Environmental Science & Technology, 2013. **47**(1): p. 142-149.

5. M. Updegraff, D., *Plugging and Penetration of Petroleum Reservoir Rock by Microorganisms*. 2018.

6. DeJong, J.T., M.B. Fritzges, and K. Nusslein, *Microbially induced cementation to control sand response to undrained shear.* Journal of Geotechnical and Geoenvironmental Engineering, 2006. **132**(11): p. 1381-1392.

7. Warren, L.A., et al., *Microbially mediated calcium carbonate precipitation: Implications for interpreting calcite precipitation and for solid-phase capture of inorganic contaminants.* Geomicrobiology Journal, 2001. **18**(1): p. 93-115.

8. Fridjonsson, E.O., et al., *NMR measurement of hydrodynamic dispersion in porous media subject to biofilm mediated precipitation reactions.* Journal of Contaminant Hydrology, 2011. **120-21**: p. 79-88.

9. Sham, E., et al., *Monitoring bacterially induced calcite precipitation in porous media using magnetic resonance imaging and flow measurements.* Journal of Contaminant Hydrology, 2013. **152**: p. 35-43.

10. Kirkland, C.M., et al., *Detecting Microbially Induced Calcite Precipitation in a Model Well-Bore Using Downhole Low-Field NMR.* Environmental Science & Technology, 2017. **51**(3): p. 1537-1543.

11. Kleinberg, R.L. and M.A. Horsfield, *Transverse Relaxation Processes in Porous Sedimentary-Rock.* Journal of Magnetic Resonance, 1990. **88**(1): p. 9-19.

12. Grunewald, E. and R. Knight, *A laboratory study of NMR relaxation times in unconsolidated heterogeneous sediments.* Geophysics, 2011. **76**(4): p. G73-G83.

13. Kleinberg, R.L., W.E. Kenyon, and P.P. Mitra, *Mechanism of NMR Relaxation of Fluids in Rock.* Journal of Magnetic Resonance Series A, 1994. **108**(2): p. 206-214.

14. Kirkland, C.M., et al., *Biofilm Detection in a Model Well-Bore Environment Using Low-Field NMR.* Ground Water Monitoring and Remediation, 2015. **35**(4): p. 36-44.

15. Brownstein, K.R. and C.E. Tarr, *Importance of Classical Diffusion in NMR-Studies of Water in Biological Cells.* Physical Review A, 1979. **19**(6): p. 2446-2453.

16. Stoodley, P., et al., *Biofilms as complex differentiated communities.* Annual Review of Microbiology, 2002. **56**: p. 187-209.

17. Shashank, B.S., Minto, J. M., Singh, D. N., Mountassir, G. E., Knapp. C. W., *Guidance for Investigating Calcite Precipitation by Urea Hydrolysis for Geomaterials* Journal of Testing and Evaluation, 2018. **46**(4): p. 1527-1538.

18. Ferris, F.G., et al., *Bacteriogenic mineral plugging.* Journal of Canadian Petroleum Technology, 1996. **35**(8): p. 56-61.

19. Stocks-Fischer, S., J.K. Galinat, and S.S. Bang, *Microbiological precipitation of CaCO3.* Soil Biology & Biochemistry, 1999. **31**(11): p. 1563-1571.

20. Edelstein, W.A., et al., *Spin Warp NMR Imaging and Applications to Human Whole-Body Imaging.* Physics in Medicine and Biology, 1980. **25**(4): p. 751-756.

21. Carr, H.Y. and E.M. Purcell, *Effects of Diffusion on Free Precession in Nuclear Magnetic Resonance Experiments.* Physical Review, 1954. **94**(3): p. 630-638.

22. Meiboom, S. and D. Gill, *Modified Spin-Echo Method for Measuring Nuclear Relaxation Times.* Review of Scientific Instruments, 1958. **29**(8): p. 688-691.

23. Foley, I., S.A. Farooqui, and R.L. Kleinberg, *Effect of paramagnetic ions on NMR relaxation of fluids at solid surfaces.* Journal of Magnetic Resonance Series A, 1996. **123**(1): p. 95-104.

24. Latour, L.L., et al., *Time-Dependent Diffusion-Coefficient of Fluids in Porous-Media as a Probe of Surface-to-Volume Ratio.* Journal of Magnetic Resonance Series A, 1993. **101**(3): p. 342-346.

25. Luo, Z.X., J. Paulsen, and Y.Q. Song, *Robust determination of surface relaxivity from nuclear magnetic resonance DT2 measurements.* Journal of Magnetic Resonance, 2015. **259**: p. 146-152.

CONCLUSION

The research presented in this dissertation demonstrates the ability to characterize various distinct phase transitions both in porous media and bulk systems by means of nuclear magnetic resonance (NMR). NMR is a unique technique in that it can be applied to obtain detailed information both on micro and macro scales non-invasively and non-destructively, thus it lends itself well to large scale field and industrial applications where the system of interest proves difficult to access non-destructively. The goal of this work was therefore to determine if, and to what extent, various phase transitions of interest to industries can be characterized using NMR relaxation and diffusion measurement and magnetic resonance imaging (MRI). The experiments performed for this dissertation are presented in chapters 4-6, and the three systems of interest were 1) drug solidification in bulk and a porous construct, 2) hydrate formation and growth, and 3) bio mineralization in granular media. The phase transitions occurring in each of these systems were successfully detected and monitored *in-situ* using NMR and MRI.

Each system posed physical challenges that had to be accommodated to obtain the desired results. Due to the small volume and the rapid solidification of fenofibrate, the study was limited to experiments where sufficient averaging could be performed in a short amount of time (chapter 4). Consequently, only frequency spectra and T_2 relaxation distributions were collected in the quest to characterize the liquid-solid transition of the drug. The Gaussian shape of the final frequency spectra of the drug solidifying in bulk indicated a highly ordered crystalline final structure. The frequency spectra of the drug in the tablet was found to be a combination of a Gaussian and Lorentzian distribution. The

Lorentzian component indicates that an amorphous component is formed, in addition to the ordered crystalline structure, due to silica-fenofibrate surface interactions. The T_2 distributions confirm the observations made in the frequency spectra, with a larger amplitude of the longer T_2 time population remaining in the drug in the tablet after solidification is complete. These results confirm the application of non-solid-state NMR to distinguish and characterize crystalline and amorphous solid structural phases. 1D T_2 and 2D T_1-T_2 correlation experiments showed that water will progressively occupy more of the pore space in the tablet when stored in a 100% relative humidity environment over a 14-day period, decreasing the detectable drug signal. Thus, NMR relaxometry has potential as a method for drug quality control.

Hydrate formation and growth is a highly complex process still not completely understood despite extensive research efforts on the subject. The short time and length scale at which hydrate nucleation and cage growth occurs makes hydrate formation processes difficult to monitor and characterize. The onset of hydrate formation and subsequent hydrate growth was successfully detected and monitored by NMR frequency spectra. Frequency spectra also indicated the completion of hydrate growth at which point the water peak was depleted. T_2 relaxation time distributions showed a decrease in the T_2 time for both water and cyclopentane due to a decrease in the water droplet size and an increase in gadolinium concentration in the cyclopentane. MRI intensity maps in combination with T_2 maps revealed a highly heterogeneous hydrate system with spatially dependent hydrate growth rates. Spatially resolved diffusion measurements confirmed the decrease in pore size of the porous hydrate shell with a reduction in the water diffusion

coefficient over the duration of the hydrate growth process. T_1-T_2 correlation measurements exhibited a signal rise at short τ_1-times and long τ_2-times during the intermediate stage of the hydrate growth process. During the intermediate stage, the porosity of the hydrate shell is reduced to $\varphi < 50\%$. The hydrate shell is still permeable allowing exchange to occur, but the mass transport between the aqueous and organic liquid phases is restricted, leaving the system in a combined state of the fast and slow diffusion regime. According to results obtain from the coupled pore model presented by Maneval et al., the observed signal rise is a result of the intermediate level of connectivity between the two phases as well as the presence of both a slow and fast diffusion regime in the hydrate system.

A low-field NMR system operating at 2 MHz was used to characterize biomineralization processes in granular media. Natural sediments, such as the quartz sand used for this study, exhibit a wide range of magnetic susceptibilities which will cause a broadening of spectral peaks and a more rapid signal attenuation. The impact of the magnetic susceptibilities is less significant at lower magnetic fields; thus, a low-field NMR system was essential for accurate characterization of this system. An increase in T_2 relaxation time was observed as a result of the production of a gas interface at the pore wall when calcite precipitate was present, inhibiting the water accessibility to the surface, and thus suppressing the surface relaxation mechanism. Mineral precipitation was found to cause a slight decrease in the total pore volume of the system, and a change in the mineral composition of the pore walls as observed in the SEM images. An estimate of the relaxivity for the glass beads, sand grains, calcite precipitate, and the gas coated calcite

was obtained. The alteration of the surface mineralogy resulted in a slight decrease in magnitude of the surface relaxivity, while the relaxivity of the gas interface was found to be significantly smaller than that of the granular media or calcite precipitate. It was therefore concluded that the presence of the gas interface caused the increase in T_2 times. Despite the similarity in relaxivity of the calcite and granular surface, and the presence of the gas interface, the mineral precipitation surface coverage percentage was successfully correlated with T_2 relaxation time and was found to be in close agreement with visual inspection of surface coverage obtained from SEM images. This is due to the textured calcite surface trapping the gas on the surface whereas the smooth glass or sand surfaces do not, resulting in an evenly distributed gas layer wherever calcite is present.

The research presented in this dissertation demonstrates that phase transitions can be successfully detected and monitored in a broad range of highly distinct systems utilizing several different NMR measurements on both low- and high-field NMR spectrometers. MRI provided the means to explore the spatial heterogeneity of changes occurring throughout the system. 1D T_2 relaxation and spectrally resolved diffusion measurements were used to detect changes in pore size and total porosity by shifts in the observed T_2 relaxation time distributions, and liquid-solid transitions by a decrease in distribution amplitudes. T_1-T_2 correlation measurements were shown to contain information about complex diffusion dynamics and exchange obtained from a signal rise observed in the time domain data.

The various NMR methods by which phase transitions can be detected and monitored indicates that NMR has strong potential to monitor and inform a broad range of industrially relevant processes where phase transitions are of interest.

REFERENCES CITED

Abragam, A., *Principles of Nuclear Magnetism* 1983: Oxford University Press, USA.

Aichele, C.P., et al., *Nuclear Magnetic Resonance Analysis of Methane Hydrate Formation in Water-in-Oil Emulsions.* Energy & Fuels, 2009. **23**(1): p. 835-841.

Amstad, E., F. Spaepen, and D.A. Weitz, *Crystallization of undercooled liquid fenofibrate.* Physical Chemistry Chemical Physics, 2015. **17**(44): p. 30158-30161.

Bagherzadeh, S.A., et al., *Magnetic Resonance Imaging of Gas Hydrate Formation in a Bed of Silica Sand Particles.* Energy & Fuels, 2011. **25**(7): p. 3083-3092.

Baldwin, B.A., A. Moradi-Araghi, and J.C. Stevens, *Monitoring hydrate formation and dissociation in sandstone and bulk with magnetic resonance imaging.* Magnetic Resonance Imaging, 2003. **21**(9): p. 1061-1069.

Belton, P.S. and B.P. Hills, *The Effects of Diffusive Exchange in Heterogeneous Systems on NMR Line-Shapes and Relaxation Processes.* Molecular Physics, 1987. **61**(4): p. 999-1018.

Belton, P.S. and B.P. Hills, *The Effects of Exchange and Interfacial Reaction in 2-Phase Systems on NMR Lineshapes and Relaxation Processes.* Molecular Physics, 1988. **65**(2): p. 313-326.

Bloch, F., *Nuclear Induction.* Physical Review, 1946. **70**(7-8): p. 460-474.

Blümich, B., *NMR Imaging of Materials*. 2000, Oxford: Clarendon Press.

Brownstein, K.R. and C.E. Tarr, *Importance of Classical Diffusion in NMR-Studies of Water in Biological Cells.* Physical Review A, 1979. **19**(6): p. 2446-2453.

Buda, A., et al., *Molecular dynamic heterogeneity of confined lipid films by H-1 magnetization-exchange nuclear magnetic resonance.* Journal of Chemical Physics, 2005. **122**(3): p. 8.

Bytchenkoff, D. and S. Rodts, *Structure of the two-dimensional relaxation spectra seen within the eigenmode perturbation theory and the two-site exchange model.* Journal of Magnetic Resonance, 2011. **208**(1): p. 4-19.

Callaghan, P.T., *Translational Dynamics & Magnetic Resonance: Principles of Pulsed Gradient Spin Echo NMR*. 2011, New York: Oxford University Press.

Carr, H.Y. and E.M. Purcell, *Effects of Diffusion on Free Precession in Nuclear Magnetic Resonance Experiments.* Physical Review, 1954. **94**(3): p. 630-638.

Chatti, I., et al., *Benefits and drawbacks of clathrate hydrates: a review of their areas of interest.* Energy Conversion and Management, 2005. **46**(9-10): p. 1333-1343.

Chen, L.T., et al., *Methane Hydrate Formation and Dissociation on Suspended Gas Bubbles in Water.* Journal of Chemical and Engineering Data, 2014. **59**(4): p. 1045-1051.

Davidson, D.W., S.K. Garg, and J.A. Ripmeester, *NMR Behavior of Clathrate Hydrate of Tetrahydrofuran .2. Deuterium Measurements.* Journal of Magnetic Resonance, 1978. **31**(3): p. 399-410.

De Muynck, W., N. De Belie, and W. Verstraete, *Microbial Carbonate Precipitation in Construction Materials: A review.* Ecological Engineering, 2010. **36**(2): p. 118-136.

DeJong, J.T., M.B. Fritzges, and K. Nusslein, *Microbially induced cementation to control sand response to undrained shear.* Journal of Geotechnical and Geoenvironmental Engineering, 2006. **132**(11): p. 1381-1392.

Dempah, K.E., J.W. Lubach, and E.J. Munson, *Characterization of the Particle Size and Polydispersity of Dicumarol Using Solid-State NMR Spectroscopy.* Molecular Pharmaceutics, 2017. **14**(3): p. 856-865.

Dwyer, L.M., et al., *Confined crystallization of fenofibrate in nanoporous silica.* Crystengcomm, 2015. **17**(41): p. 7922-7929.

Edelstein, W.A., et al., *Spin Warp NMR Imaging and Applications to Human Whole-Body Imaging.* Physics in Medicine and Biology, 1980. **25**(4): p. 751-756.

Ferris, F.G., et al., *Bacteriogenic mineral plugging.* Journal of Canadian Petroleum Technology, 1996. **35**(8): p. 56-61.

Fick, A., *Uber Diffusion*. 1855, Phil. Mag.

Foley, I., S.A. Farooqui, and R.L. Kleinberg, *Effect of paramagnetic ions on NMR relaxation of fluids at solid surfaces.* Journal of Magnetic Resonance Series A, 1996. **123**(1): p. 95-104.

Fridjonsson, E.O., et al., *NMR measurement of hydrodynamic dispersion in porous media subject to biofilm mediated precipitation reactions.* Journal of Contaminant Hydrology, 2011. **120-21**: p. 79-88.

Friesen, D.T., et al., *Hydroxypropyl Methylcellulose Acetate Succinate-Based Spray-Dried Dispersions: An Overview.* Molecular Pharmaceutics, 2008. **5**(6): p. 1003-1019.

Fujara, F., et al., *Translational and Rotational Diffusion in Supercooled Orthoterphenyl Close to the Glass-Transition.* Zeitschrift Fur Physik B-Condensed Matter, 1992. **88**(2): p. 195-204.

Gao, S.Q., *Hydrate Risk Management at High Watercuts with Anti-agglomerant Hydrate Inhibitors.* Energy & Fuels, 2009. **23**(3-4): p. 2118-2121.

Gao, S.Q., W.G. Chapman, and W. House, *Application of low field NMR T-2 measurements to clathrate hydrates.* Journal of Magnetic Resonance, 2009. **197**(2): p. 208-212.

Genov, G., et al., *Experimental studies on the formation of porous gas hydrates.* American Mineralogist, 2004. **89**(8-9): p. 1228-1239.

Grunewald, E. and R. Knight, *A laboratory study of NMR relaxation times in unconsolidated heterogeneous sediments.* Geophysics, 2011. **76**(4): p. G73-G83.

Haber, A., et al., *Hydrate Shell Growth Measured Using NMR.* Langmuir, 2015. **31**(32): p. 8786-8794.

Hahn, E.L., *Spin Echoes.* Physical Review, 1950. **77**(5): p. 746-746.

Hammerschmidt, E.G., *Formation of gas hydrates in natural gas transmission lines.* Industrial and Engineering Chemistry, 1934. **26**: p. 851-855.

Heinz, A., et al., *Understanding the solid-state forms of fenofibrate - A spectroscopic and computational study.* European Journal of Pharmaceutics and Biopharmaceutics, 2009. **71**(1): p. 100-108.

Hoult, D.I. and R.E. Richards, *Critical Factors in Design of Sensitive High-Resolution Nuclear Magnetic-Resonance Spectrometers.* Proceedings of the Royal Society of London Series a-Mathematical Physical and Engineering Sciences, 1975. **344**(1638): p. 311-340.

Johnson, D.L. and L.M. Schwartz, *Analytic theory of two-dimensional NMR in systems with coupled macro- and micropores.* Physical Review E, 2014. **90**(3): p. 032407.

Karanjkar, P.U., J.W. Lee, and J.F. Morris, *Surfactant Effects on Hydrate Crystallization at the Water-Oil Interface: Hollow-Conical Crystals.* Crystal Growth & Design, 2012. **12**(8): p. 3817-3824.

Kashchiev, D. and A. Firoozabadi, *Induction time in crystallization of gas hydrates.* Journal of Crystal Growth, 2003. **250**(3-4): p. 499-515.

Kelland, M.A., *History of the development of low dosage hydrate inhibitors.* Energy & Fuels, 2006. **20**(3): p. 825-847.

Kirkland, C.M., et al., *Biofilm Detection in a Model Well-Bore Environment Using Low-Field NMR.* Ground Water Monitoring and Remediation, 2015. **35**(4): p. 36-44.

Kirkland, C.M., et al., *Detecting Microbially Induced Calcite Precipitation in a Model Well-Bore Using Downhole Low-Field NMR.* Environmental Science & Technology, 2017. **51**(3): p. 1537-1543.

Kleinberg, R.L., et al., *Deep sea NMR: Methane hydrate growth habit in porous media and its relationship to hydraulic permeability, deposit accumulation, and submarine slope stability.* Journal of Geophysical Research-Solid Earth, 2003. **108**(B10): p. 17.

Kleinberg, R.L. and M.A. Horsfield, *Transverse Relaxation Processes in Porous Sedimentary-Rock.* Journal of Magnetic Resonance, 1990. **88**(1): p. 9-19.

Kleinberg, R.L., W.E. Kenyon, and P.P. Mitra, *Mechanism of NMR Relaxation of Fluids in Rock.* Journal of Magnetic Resonance Series A, 1994. **108**(2): p. 206-214.

Koh, C.A., et al., *Fundamentals and Applications of Gas Hydrates*, in *Annual Review of Chemical and Biomolecular Engineering, Vol 2*, J.M. Prausnitz, Editor. 2011, Annual Reviews: Palo Alto. p. 237-257.

Kubo, R., *A Stochastic Theory of Line Shape and Relaxation* in *Fluctuation, Relaxation, and Resonance in Magnetic Systems* D. Ter Haar, Editor. 1962, Oliver and Boyd Ltd: Edinburgh. p. 23-68.

Kvamme, B., et al., *Storage of CO2 in natural gas hydrate reservoirs and the effect of hydrate as an extra sealing in cold aquifers.* International Journal of Greenhouse Gas Control, 2007. **1**(2): p. 236-246.

Kvamme, B., et al., *Phase Field Approaches to the Kinetic Modeling of Hydrate Phase Transitions*, in *Natural gas hydrates - Energy resource potential and associated geological hazards*. 2009, The American Association of Petroleum Geologists. p. 758-769.

Latour, L.L., et al., *Time-Dependent Diffusion-Coefficient of Fluids in Porous-Media as a Probe of Surface-to-Volume Ratio.* Journal of Magnetic Resonance Series A, 1993. **101**(3): p. 342-346.

Luo, Z.X., J. Paulsen, and Y.Q. Song, *Robust determination of surface relaxivity from nuclear magnetic resonance DT2 measurements.* Journal of Magnetic Resonance, 2015. **259**: p. 146-152.

M. Updegraff, D., *Plugging and Penetration of Petroleum Reservoir Rock by Microorganisms*. 2018.

Maneval, J.E., et al., *A Two-Region Transport Model for Interpreting T_1-T_2 Measurements in Complex Systems.* To be submitted Journal of Magnetic Resonance, 2018.

Mansfield, P. and P.K. Grannell, *NMR Diffraction in Solids.* Journal of Physics C-Solid State Physics, 1973. **6**(22): p. L422-L426.

Meiboom, S. and D. Gill, *Modified Spin-Echo Method for Measuring Nuclear Relaxation Times.* Review of Scientific Instruments, 1958. **29**(8): p. 688-691.

Mills, R., *Self-diffusion in normal and heavy water in the range 1-45.deg.* The Journal of Physical Chemistry, 1973. **77**(5): p. 685-688.

Mitchell, J., J.B.W. Webber, and J.H. Strange, *Nuclear magnetic resonance cryoporometry.* Physics Reports-Review Section of Physics Letters, 2008. **461**(1): p. 1-36.

Mondrakovski, I.L., et al., *Hydrate layers on ice particles and superheated ice: a H-1 NMR microimaging study.* Journal of Physical Chemistry A, 1999. **103**(26): p. 4969-4972.

Moudrakovski, I.L., et al., *Methane and carbon dioxide hydrate formation in water droplets: Spatially resolved measurements from magnetic resonance microimaging.* Journal of Physical Chemistry B, 2004. **108**(45): p. 17591-17595.

Murdande, S.B., et al., *Solubility Advantage of Amorphous Pharmaceuticals: I. A Thermodynamic Analysis.* Journal of Pharmaceutical Sciences, 2010. **99**(3): p. 1254-1264.

Nakajima, M., R. Ohmura, and Y.H. Mori, *Clathrate Hydrate Formation from Cyclopentane-in-Water Emulsions.* Industrial & Engineering Chemistry Research, 2008. **47**(22): p. 8933-8939.

Petrov, O.V. and I. Furo, *NMR cryoporometry: Principles, applications and potential.* Progress in Nuclear Magnetic Resonance Spectroscopy, 2009. **54**(2): p. 97-122.

Pham, T.N., et al., *Analysis of Amorphous Solid Dispersions Using 2D Solid-State NMR and H-1 T-1 Relaxation Measurements.* Molecular Pharmaceutics, 2010. **7**(5): p. 1667-1691.

Phillips, A.J., et al., *Fracture Sealing with Microbially-Induced Calcium Carbonate Precipitation: A Field Study.* Environmental Science & Technology, 2016. **50**(7): p. 4111-4117.

Phillips, A.J., et al., *Potential CO2 Leakage Reduction through Biofilm-Induced Calcium Carbonate Precipitation.* Environmental Science & Technology, 2013. **47**(1): p. 142-149.

Pietrass, T., et al., *Monitoring Xenon Clathrate Hydrate Formation on Ice Surfaces with Optically Enhanced XE-129 NMR.* Journal of the American Chemical Society, 1995. **117**(28): p. 7520-7525.

Provencher, S.W., *A Constrained Regularization Method for Inverting Data Represented by Linear Algebraic or Integral-Equations.* Computer Physics Communications, 1982. **27**(3): p. 213-227.

Rao, I., et al., *Gas Hydrate Deposition on a Cold Surface in Water-Saturated Gas Systems.* Industrial & Engineering Chemistry Research, 2013. **52**(18): p. 6262-6269.

Ripmeester, J.A. and S. Alavi, *Some current challenges in clathrate hydrate science: Nucleation, decomposition and the memory effect.* Current Opinion in Solid State & Materials Science, 2016. **20**(6): p. 344-351.

Ripmeester, J.A., S.K. Garg, and D.W. Davidson, *NMR Behavior of the Clathrate Hydrate of Tetrahydrofuran .3. Effect of Oxygen.* Journal of Magnetic Resonance, 1980. **38**(3): p. 537-544.

Ripmeester, J.A. and C.I. Ratcliffe, *Low-Temperature Cross-Polarization Magic Angle Spinning C-13 NMR of Solid Methane Hydrates - Structure, Cage Occupancy, and Hydration Number.* Journal of Physical Chemistry, 1988. **92**(2): p. 337-339.

Ripmeester, J.A., et al., *A New Clathrate Hydrate Structure.* Nature, 1987. **325**(6100): p. 135-136.

Santyr, G.E., R.M. Henkelman, and M.J. Bronskill, *Variation in Measured Transverse Relaxation in Tissue Resulting from Spin Locking with the CPMG Sequence.* Journal of Magnetic Resonance, 1988. **79**(1): p. 28-44.

Sham, E., et al., *Monitoring bacterially induced calcite precipitation in porous media using magnetic resonance imaging and flow measurements.* Journal of Contaminant Hydrology, 2013. **152**: p. 35-43.

Shashank, B.S., Minto, J. M., Singh, D. N., Mountassir, G. E., Knapp. C. W., *Guidance for Investigating Calcite Precipitation by Urea Hydrolysis for Geomaterials* Journal of Testing and Evaluation, 2018. **46**(4): p. 1527-1538.

Siddique, R. and N.K. Chahal, *Effect of ureolytic bacteria on concrete properties.* Construction and Building Materials, 2011. **25**(10): p. 3791-3801.

Skotnicki, M., et al., *Characterization of Two Distinct Amorphous Forms of Valsartan by Solid-State NMR.* Molecular Pharmaceutics, 2016. **13**(1): p. 211-222.

Skovborg, P., et al., *Measurement of Induction Times for the Formation of Methane and Ethane Gas Hydrates.* Chemical Engineering Science, 1993. **48**(3): p. 445-453.

Sloan, E.D., *Fundamental principles and applications of natural gas hydrates.* Nature, 2003. **426**(6964): p. 353-359.

Sloan, E.D. and C.A. Koh, *Clathrate Hydrates of Natural Gases, Third Edition*. Clathrate Hydrates of Natural Gases, Third Edition. Vol. 119. 2008, Boca Raton: Crc Press-Taylor & Francis Group. 1-701.

Sloan, E.D., et al., *Quantifying hydrate formation and kinetic inhibition.* Industrial & Engineering Chemistry Research, 1998. **37**(8): p. 3124-3132.

Song, Y.Q., et al., *Experimental Identification of Diffusive Coupling Using 2D NMR.* Physical Review Letters, 2014. **113**(23): p. 5.

Song, Y.Q., et al., *T-1-T-2 correlation spectra obtained using a fast two-dimensional Laplace inversion.* Journal of Magnetic Resonance, 2002. **154**(2): p. 261-268.

Song, Y.Q., L. Zielinski, and S. Ryu, *Two-dimensional NMR of diffusion systems.* Physical Review Letters, 2008. **100**(24): p. 4.

Stejskal, E.O., *Use of Spin Echoes in a Pulsed Magnetic-Field Gradient to Study Anisotropic Restricted Diffusion and Flow.* Journal of Chemical Physics, 1965. **43**(10P1): p. 3597-+.

Stejskal, E.O. and J.E. Tanner, *Spin Diffusion Measurements: Spin Echoes in the Presence of a Time-Dependent Field Gradient.* Journal of Chemical Physics, 1965. **42**(1): p. 288-+.

Stocks-Fischer, S., J.K. Galinat, and S.S. Bang, *Microbiological precipitation of CaCO3.* Soil Biology & Biochemistry, 1999. **31**(11): p. 1563-1571.

Stoodley, P., et al., *Biofilms as complex differentiated communities.* Annual Review of Microbiology, 2002. **56**: p. 187-209.

Sun, C.Y., et al., *The growth kinetics of hydrate film on the surface of gas bubble suspended in water or aqueous surfactant solution.* Journal of Crystal Growth, 2007. **306**(2): p. 491-499.

Susilo, R., et al., *Hydrate kinetics study in the presence of nonaqueous liquid by nuclear magnetic resonance spectroscopy and imaging.* Journal of Physical Chemistry B, 2006. **110**(51): p. 25803-25809.

Szklarz, G., et al., *Crystallization of supercooled fenofibrate studied at ambient and elevated pressures.* Physical Chemistry Chemical Physics, 2017. **19**(15): p. 9879-9888.

Taylor, C.J., et al., *Macroscopic investigation of hydrate film growth at the hydrocarbon/water interface.* Chemical Engineering Science, 2007. **62**(23): p. 6524-6533.

Tegze, G., L. Granasy, and B. Kvamme, *Phase field modeling of CH4 hydrate conversion into CO2 hydrate in the presence of liquid CO2.* Physical Chemistry Chemical Physics, 2007. **9**(24): p. 3104-3111.

Thrane, L.W., et al., *NMR Relaxometry to Characterize the Drug Structural Phase in a Porous Construct.* Molecular Pharmaceutics, 2018. **15**(7): p. 2614-2620. DOI: 10.1021/acs.molpharmaceut.8b00144

Torrey, H.C., *Bloch Equations with Diffusion Terms.* Physical Review, 1956. **104**(3): p. 563-565.

Vallet-Regi, M., *Ordered mesoporous materials in the context of drug delivery systems and bone tissue engineering.* Chemistry-a European Journal, 2006. **12**(23): p. 5934-5943.

Vallet-Regi, M., et al., *A new property of MCM-41: Drug delivery system.* Chemistry of Materials, 2001. **13**(2): p. 308-311.

Walsh, M.R., et al., *Microsecond Simulations of Spontaneous Methane Hydrate Nucleation and Growth.* Science, 2009. **326**(5956): p. 1095-1098.

Wang, S.B., *Ordered mesoporous materials for drug delivery.* Microporous and Mesoporous Materials, 2009. **117**(1-2): p. 1-9.

Wanlass, L.K. and J. Wakabayashi, *Stimulated Spin-Echo Measurement of Cross-Relaxation in Neutron-Irradiated Calcite.* Physical Review Letters, 1961. **6**(6): p. 271-+.

Warren, L.A., et al., *Microbially mediated calcium carbonate precipitation: Implications for interpreting calcite precipitation and for solid-phase capture of inorganic contaminants.* Geomicrobiology Journal, 2001. **18**(1): p. 93-115.

Warrier, P., et al., *Overview: Nucleation of clathrate hydrates.* Journal of Chemical Physics, 2016. **145**(21).

Washburn, K.E., et al., *Simultaneous Gaussian and exponential inversion for improved analysis of shales by NMR relaxometry.* Journal of Magnetic Resonance, 2015. **250**: p. 7-16.

Xu, Z.P., et al., *Inorganic nanoparticles as carriers for efficient cellular delivery.* Chemical Engineering Science, 2006. **61**(3): p. 1027-1040.

Yang, M.J., et al., *Advances in nuclear magnetic resonance (NMR) techniques for the investigation of clathrate hydrates.* Renewable & Sustainable Energy Reviews, 2017. **74**: p. 1346-1360.

Yuan, X.D., D. Sperger, and E.J. Munson, *Investigating Miscibility and Molecular Mobility of Nifedipine-PVP Amorphous Solid Dispersions Using Solid-State NMR Spectroscopy.* Molecular Pharmaceutics, 2014. **11**(1): p. 329-337.

Zhao, J.F., et al., *In-situ visual observation for the formation and dissociation of methane hydrates in porous media by magnetic resonance imaging.* Magnetic Resonance Imaging, 2015. **33**(4): p. 485-490.

Zylyftari, G., A. Ahuja, and J.E. Morris, *Nucleation of cyclopentane hydrate by ice studied by morphology and rheology.* Chemical Engineering Science, 2014. **116**: p. 497-507.

APPENDIX

EXPERIMENTAL CONFIGURATION AND ADDITIONAL NMR RESULTS FOR MICP MANUSCRIPT

Preparation of Bacteria Culture, Test Column, and Injection Media

To prepare the bacteria culture for injection, 1 mL of frozen stock *S. pasteurii* was added to 100 mL of growth medium containing 37 g/L brain heart infusion (BHI) and 20 g/L urea and placed on a shaker table at 150 rpm for 24 h. At the end of the 24 h period, 1 mL of the culture was added to 100 mL of fresh growth medium and placed on the shaker table to be used for next-day culture injection. The remaining 99 mL was injected into the column for inoculation. This procedure was repeated daily until the end of the study.

A bacterial growth medium and a calcite precipitation-promoting medium were used for this study. Both mediums contained 3 g/L Difco nutrient broth, 20 g/L urea, and 10 g/L ammonium chloride. In addition, the calcite precipitation-promoting media contained 49 g/L calcium chloride. Both were prepared in a sterile manner using distilled (DI) water.

Before each study, the sand- or glass-filled column was disinfected by injecting two pore volumes of a 70% ethanol solution followed by two pore volumes of a 10% bleach solution. A stationary period of 30 minutes was permitted between the ethanol and bleach injections. The disinfection procedure was followed by injecting two pore volumes of sterile DI water to prevent the bacteria culture from getting in contact with the disinfectants.

Testing Homogeneity of Mineral Precipitation

NMR data was collected from the top and bottom of the column on the first and final day of the study to investigate the homogeneity of the mineral precipitation

throughout the length of the system. 1D signal intensity profiles and T_2 distributions of the column collected on the final day of the 0.45 mm sand grains is shown in Figure A.1. Figure A.1(a) shows the signal intensity profile for a 4 cm region at the bottom of the column (blue) compared to a 4 cm region at the top (red). The comparison of the T_2 distribution at the top (red) and bottom (blue) of the column is shown in Figure A.1(b). No significant differences between the top and the bottom of the column was observed in the signal intensity profiles or the T_2 distributions. NMR measurements of the top and bottom were also collected on the first day of the study (not shown) and the results were identical also on day one.

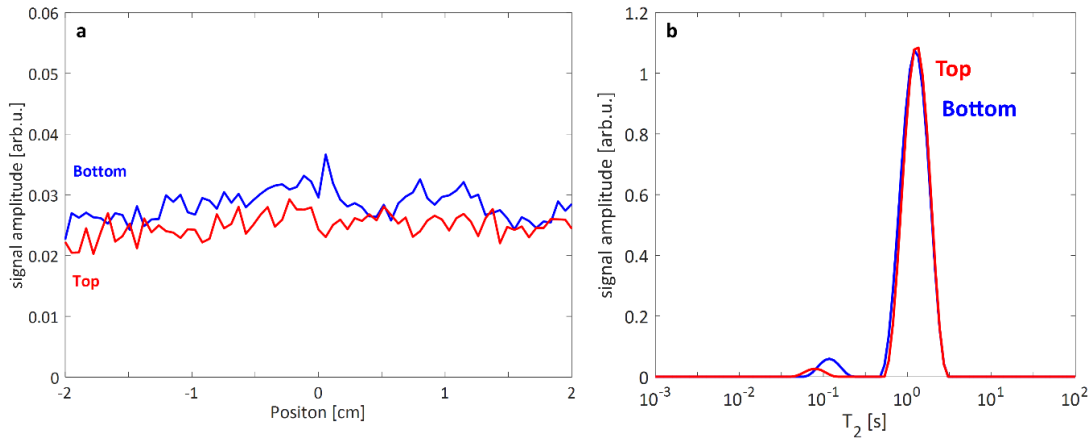

Figure A.1. To confirm homogeneous MICP throughout the length of the column, NMR measurements were performed both at the top and bottom of the column. Both the signal intensity profile (a) and the T_2 distribution (b) confirm uniform calcite precipitation.

Impact of Air Bubbles

T_2 measurements were performed on a biomineralized column with 0.5 mm glass beads fully saturated and after air was flowed through the column to investigate the effect of air bubbles present in the pore space. A shift to a shorter T_2-time was observed in the

presence of air bubbles. The shift to longer T_2-times observed during the MICP process is attributed to a gas interface appearing between the bulk water and the pore walls, reducing the accessibility of water to the surface. The air flowed through the column will not reproduce this gas layer, but rather result in air bubbles trapped in the pore space. The bubbles will occupy partial volumes of the pore space, reducing the effect of the slower bulk relaxation rate while simultaneously increasing the effect of the surface relaxation mechanism, resulting in the slightly faster relaxation rate observed in Figure A.2.

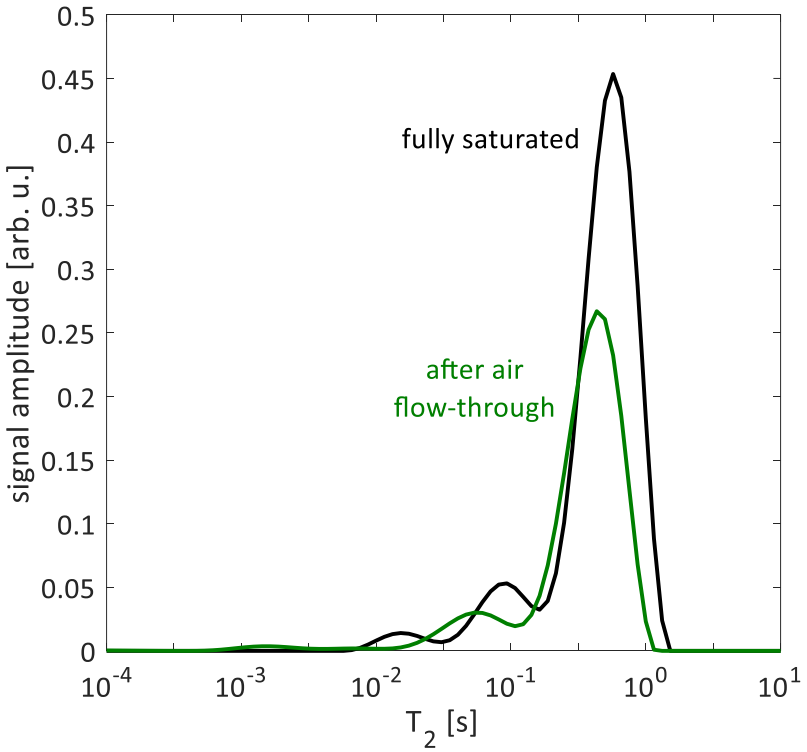

Figure A.2. T_2 distributions of (a) a fully saturated 0.5 mm glass beads column after MICP, and (b) after air was flowed through the column. A shift to slightly shorter T_2-times were observed due to the presence of air bubbles in the pore space.